# Università degli Studi di Ferrara

DOTTORATO DI RICERCA IN
"FISICA"

CICLO XXVI

COORDINATORE Prof. Vincenzo Guidi

# An insight into the role of magnetic anisotropies in the behavior of thin films and arrays of nanoparticles

Settore Scientifico Disciplinare FIS/03

**Dottorando**
Dott. Fin Samuele

**Tutore**
Prof. Bisero Diego

Anni 2011/2014

# Contents

# Introduction

In the last years the scientific interest on nanotechnologies has covered all the research fields, starting from electronics and magnetism due to the necessity to reduce the sizes of hardware in computers and increase the density of memory storage.

The importance of studying the magnetic properties of nanostructures derives from the fact that they change dramatically when the dimensions are reduced under the micrometer and new physical phenomena take place. With respect to the bulk magnetic materials, effects like Giant Magnoresistance, Oscillatory Exchange Coupling or Perpendicular Magnetic Anisotropy (just to quote some examples) are evidenced and they have a great impact on the development of new technological equipment and products.

The reasons of the different magnetic behavior of the materials when they are in the nanostructured form must be searched primarily in the change of the relative strength of dipolar and exchange interactions and in the elemental (and then) quantum-mechanical nature of the matter, which emerges when the dimensions of the objects are near to those of the atom itself.

One of the important properties which is strongly affected by the size reduction and in which is contained most of the physical description of a magnetic system is the anisotropy energy term: a direction-dependent parameter which strongly contributes to the determination of the equilibrium state and magnetic behavior.

In this thesis we describe various nanostructured systems concentrating prevalently on thin films and arrays of interacting nanoparticles and for each system the origin and the physical implications of magnetic anisotropy is discussed.

In the first chapter we report the theoretical knowledge of nanomagnetism: the energy terms involved in the determination of equilibrium state and reversal process, various typologies of magnetic anisotropies, their origins and their implications. We perform a description of the magnetic domains and how they are influenced by the shape and dimensions of the nanoparticles.

In the second chapter a brief discussion of the experimental instrumentation is done. We report the experimental methods and instrument prevalently used: Magnetic Force Microscopy for the determination and imaging of the magnetization distribution, the Magneto-Optical Kerr Effect Magnetometry and Vibrating Sample Magnetometer for the production of the hysteresis loops and finally the Brillouin Light Scattering technique for the detection of the spin-wave frequencies in the magnetic media.

The following part of the thesis deals with the nanostructured systems analyzed and anisotropies characterizing them. It is divided in two sections: thin magnetostrictive films and arrays of nanoparticles.

In the first topic, two types of magnetic anisotropies are presented: Perpendicular Magnetic Anisotropy which has a crystalline origin and competes with the shape anisotropy of the thin film producing a singular type of magnetic domains called “stripes” and the Rotatable Anisotropy (the easy magnetic direction is not fixed but could be rotated by means of an external magnetic field). We tried to give a better explanation and modeling of the Rotatable Anisotropy, making a parallelism between the static and dynamic experimental evidences.

The second topic regards the description of the interaction of magnetic dots in arrays with different symmetry and with finite dimensions. In particular we discovered a peculiar space-dependent behavior that we called “global configurational anisotropy”, that has a strong importance when the dimension of the array becomes comparable with the dimension of the nanoparticles.

# Theoretical Concepts

## Introduction

The “Nanomagnetism” is the area of research in physics that refers to the magnetic properties and behaviors of systems in which at least one of the spatial dimensions is reduced in the nanoscopic scale. Nanomagnetism involves objects like films (one dimension is in the nanoscale), nanowires (two dimensions are in the nanoscale) and nanodots (all the spatial dimensions are in the nanoscale).

It is possible to combine magnetic and non-magnetic films in multilayers, superimposing one film to the other, as it is possible to bring the nanowires so close that they interact (1) and even to produce nanowires multilayered (2). Moreover it is possible to form one-dimensional (chains) and two-dimensional arrays of nanodots, single or multi-layered, and for each arrangement the dots could have different dimension, composition or geometry (circular, squared, exagonal etc.) (3).

All the infinite combinations of dimensionality, size, shape, composition, interaction, symmetry give as many different magnetic properties like equilibrium energies, domain shapes, switching fields, coercive fields or the dynamical responses of the spin-wave frequencies. Every features change, as we will see, could be associated to an anisotropy term, that is an energy term whose minimization could be reached only in some particular directions of the system.

To better structure and frame the following considerations on magnetic behaviors and magnetic anisotropies involved in the studied systems we do a brief theoretical excursus on the general knowledge of magnetism and then we relate it with the reduction of dimension in magnetic materials in the specific sections.

## The magnetostatic energy

The magnetostatic energy arises from the interaction of the magnetization itself with the magnetic field $H_d$ i.e. the field coming only from any divergence in the magnetization M. This is the reason why this term is also said “self energy”. The magnetostatic energy density can be expressed in the following term:

$$E_{ms} = -\frac{\mu_0}{2}\mathbf{H_d} \cdot \mathbf{M}$$

In a magnetic body in equilibrium, the demagnetizing field $\mathbf{H_d}$ is antiparallel to the magnetization that generates it.

## The exchange energy

The exchange energy is a quantum mechanical quantity that can be described by a phenomenological approach. Considering the following expression:

$$E_{ex} = -JS^2 \sum_{i \neq j} \cos \phi_{ij}^2$$

where S is the total spin momentum per atom and $\phi_{ij}$ is the angle between the directions of the spin momentum vectors of atom i and j, the term J is the exchange constant, which is a measure of the intensity of the interaction. The exchange constant, or exchange integral, comes from the quantum mechanical interaction between electrons in their shared orbitals. In ferromagnetic materials the exchange integral is positive and thus the energy is minimized when the spins are parallel. From this point of view, the exchange energy is in competition with the magnetostatic energy and the equilibrium point is determined by the shape, size and thickness of the object. (4)

### The Zeeman energy

The Zeeman contribution to the overall energy is due to the application of an external magnetic field:

$$E_Z = -\mu_0 \mathbf{M} \cdot \mathbf{H}$$

The Zeeman energy is minimized when the magnetization is aligned with the external field (as we can see from the fact that the scalar product reaches its maximum when the magnetization vector is parallel to the external field).

### The anisotropy energy

When a physical property of a material is a function of direction, that property is said to exhibit anisotropy. The preference for the magnetization to lie in a particular direction in a sample is called Magnetic Anisotropy.

There are different sources of the anisotropy: shape, magnetocrystalline, surface and interface anisotropy, strain anisotropy and growth induced anisotropy, configurational anisotropy etc.

Each type of energy term contribution modifies the total amount of energy density and therefore the magnetic behavior of the material and in particular we will see as magnetic anisotropy could influence the magnetic properties of a system.

## Magnetic Anisotropy

### Shape Anisotropy

The shape anisotropy is due to the presence, in every magnetic sample, of a demagnetizing field $\mathbf{H_d}$ which opposes to magnetization and tends to reduce it prevalently in the direction in which it has a greater value.

Suppose a bar sample is magnetized by a field applied from left to right and subsequently removed. Then a north pole is formed at the right end, and a south pole at the left, as shown in Fig. 1 (5). We see that the H lines, radiating out from the north pole and ending at the south pole, constitute a field both outside and inside the magnet which acts from north to south and which therefore tends to demagnetize the magnet.

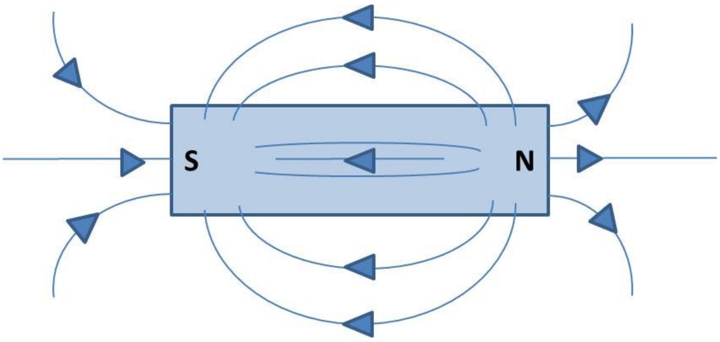

Figure 1: Emergent surface stray field and bulk demagnetizing field due to the “free poles” at the edges of a magnetized bar.

This self-demagnetizing action of a magnetized body is important, not only because of its bearing on magnetic measurements, but also because it strongly influences the behavior of magnetic materials in many practical devices.

The demagnetizing field $\mathbf{H}_\mathbf{d}$ acts in the opposite direction to the magnetization M which creates it.

If we model the shape of the bar, smoothing its corner, it is possible to obtain a ideally uniform parallel demagnetizing field. It may be shown, although not easily, that the correct taper to achieve this result is that of an ellipsoid (Fig. 2) (5). If an unmagnetized ellipsoid is placed in a uniform magnetic field, it becomes magnetized uniformly throughout; the uniformity of M and B are due to the uniformity of $H_d$ throughout the volume. This uniformity can be achieved only in an ellipsoid.

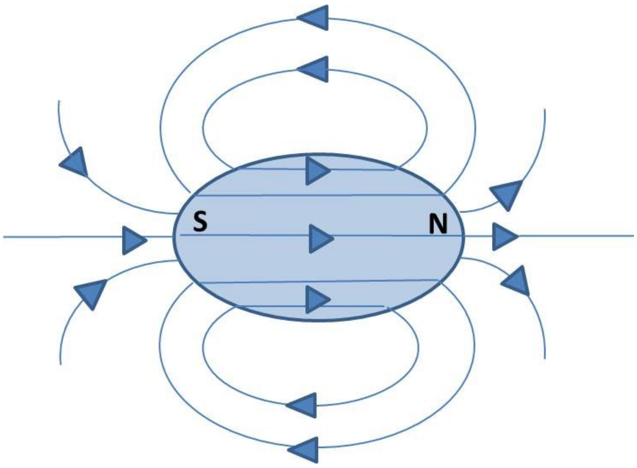

Figure 2: Uniform magnetization and uniform demagnetizing field in an ellipsoid.

The demagnetizing field $H_d$ of a body is proportional to the magnetization which creates it and as said is antiparallel:

$H_d = -N_d M$

where $N_d$ is the demagnetizing factor or demagnetizing coefficient.

The value of $N_d$ depends mainly on the shape of the body, and has a single calculable value only for an ellipsoid.

It is clear that it depends on the relative lengths of the three spatial dimensions: along a short axis the external surfaces are very close and this favors the demagnetization, and therefore the demagnetizing factor increases; viceversa, in a long axis the surfaces (and thus the “free magnetic charges”) are not close and it is more difficult to demagnetize the sample in that direction. The sum of the demagnetizing factors along the three orthogonal axes of an ellipsoid is a constant.

$N_a + N_b + N_c = 1$

For a sphere, the three demagnetizing factors must be equal, so $N_{sphere} = 1/3$.

The general ellipsoid has three unequal axes 2a, 2b, 2c, and a section perpendicular to any axis is an ellipse (Fig. 3) (5). Of greater practical interest is the ellipsoid of revolution, or spheroid. A prolate spheroid is formed by rotating an ellipse about its major axis 2c; then $a = b < c$, and the resulting solid is cigar-shaped. Rotation about the minor axis 2a results in the disk-shaped oblate spheroid, with $a < b = c$. Maxwell calls this the planetary spheroid, which may be easier to remember (5).

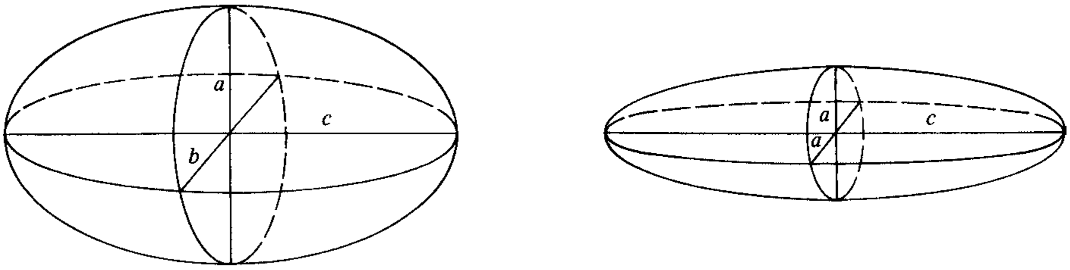

General ellipsoid Prolate spheroid

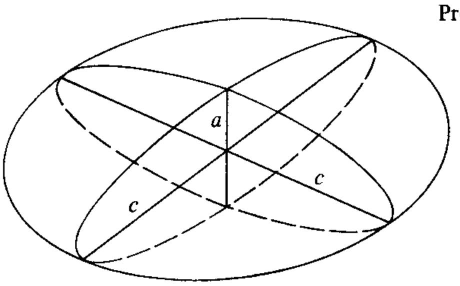

Oblate spheroid

Figure 3: Ellipsoids with different ratio between the axis. General, Prolate (Cigar) and Oblate (Planetary) spheroids.

Equations, tabular data, and graphs for the demagnetizing factors of general ellipsoids are given by E. C. Stoner [Phil. Mag., 36 (1945) p. 803] (6) and J. A. Osborn [Phys. Rev., 67 (1945) p. 351] (7).

Specimens often encountered in our practice are thin films, elliptical dots or disks magnetized in their plane.

What is important to evidence is that the contribution to the Magnetostatic Energy is strictly conditioned from the shape of the sample.

In the next section we will see in particular three types of systems: thin films, nanostructured ellipses and circular nanostructured dots. We can to some extent represent thin films as oblate spheroid (as in figure 3) with $a \rightarrow 0$ and $b = c$ both very large. We see as for thin film $N_a \approx 1$, $N_c \rightarrow 0$.

For circular disk the situation is not trivial and each case must be considered individually. Finally for the elliptical dots, we can consider the case of a general spheroid but it is simple to show how the easy direction is everytime the longer one.

Consider a polycrystalline specimen having no preferred orientation of its grains, and therefore no net crystal anisotropy. If it is spherical in shape, the same applied field will magnetize it to the same extent in any direction. But if it is nonspherical, it will be easier to magnetize it along a long axis than along a short axis. The reason for this is (as clearly described just now) the demagnetizing field along a short axis is stronger than along a long axis. The applied field along a short axis then has to be stronger to produce the same true field inside the specimen. Thus shape alone can be a source of magnetic anisotropy.

In order to treat shape anisotropy quantitatively, we write an expression for the magnetostatic energy $E_{ms}$ of a permanently magnetized body in zero applied field. If a body is magnetized by an applied field to some level A (Fig.4) (5) and the applied field is then removed, the magnetization will decrease to C under the action of the demagnetizing field $H_d$.

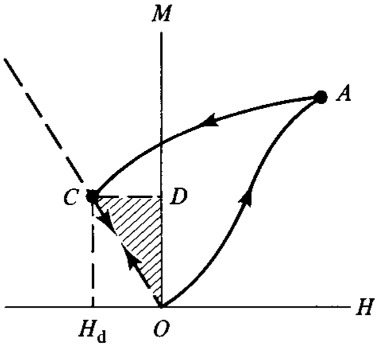

Figure 4: the applied field is then removed, the magnetization will decrease under the action of the demagnetizing field $H_d$. The shadowed area is the magnetostatic energy of the magnet.

Here OC is the demagnetizing-field line, with a slope of $-1/N_d$, where $N_d$ is the demagnetizing coefficient. The specimen then contains stored energy $E_{ms}$ equal to the area of the shaded triangle

OCD. This energy is that associated with the demagnetizing field of the specimen, and is variously called the magnetostatic energy, the self-energy, or the energy of a magnet in its own field.

$$E_{ms} = \frac{\mu_0}{2} \int H_d^2 dv$$

where $dv$ is an element of volume and the integration extends over all space. The distribution of $H_d$ in space is generally not known accurately and, even when it is, the evaluation of this integral would be difficult. It is easier to compute the area of the triangle OCD in Fig.4. This energy can be written in vector form as

$$E_{ms} = -\frac{\mu_0}{2} \mathbf{H_d} \cdot \mathbf{M}$$

where M is the level of magnetization at point C.

Since magnetization and demagnetizing field vectors are antiparallel $\mathbf{H_d} = -N_d \mathbf{M}$ therefore (in the SI)

$$E_{ms} = \frac{\mu_0}{2} N_d M^2$$

## Magnetocrystalline Anisotropy

In BCC Fe, the magnetization process is said to be easy in the [100] directions and hard in the [111] directions because the field needed to magnetize iron to saturation is smaller in the [100] direction than in any others. This is called Magnetocrystalline Anisotropy because its origin is of crystalline structure nature and could be explained considering the Spin-Orbit coupling in the atoms of the ferromagnetic material. In FCC Nichel, the case is just the opposite: [111] directions are easy, [100] hard, and the fields required for saturation in the hard directions are smaller for Ni than for Fe. Cobalt is hexagonal, and its easy direction of magnetization is the c axis; to saturate the sample in the basal plane is very difficult, more than an order of magnitude harder than in the [111] directions in Fe.

After saturation, reduction of the field to zero leaves most of the magnetization remaining in the direction in which the field had been applied if it is an easy direction. In the absence of an external field, the magnetization remaining at H=0, called "remanence", is non zero for Fe and Ni magnetized in hard directions, whereas it is zero for Co magnetized in a hard direction.

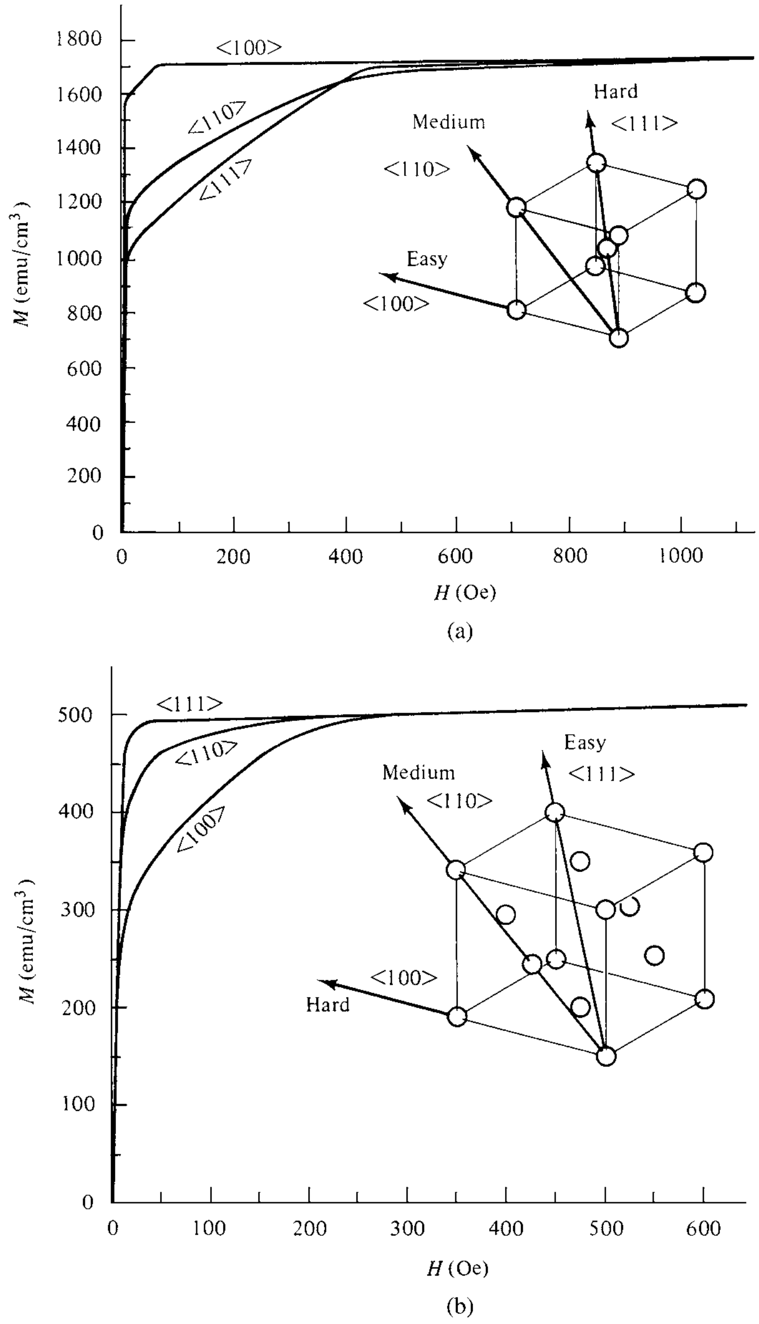

Figure 5: magnetization curves for Iron and Nichel (5)

Figure 5 shows that fairly high fields, of the order of several hundred Oersteds, are needed to saturate iron in a [110] direction.

More generally, the direction of easy magnetization of a crystal is the direction of spontaneous domain magnetization in the demagnetized state. When an increasing external field is applied to one arbitrary direction, the magnetization grows in the easy direction following the scheme of figure 6 (5).

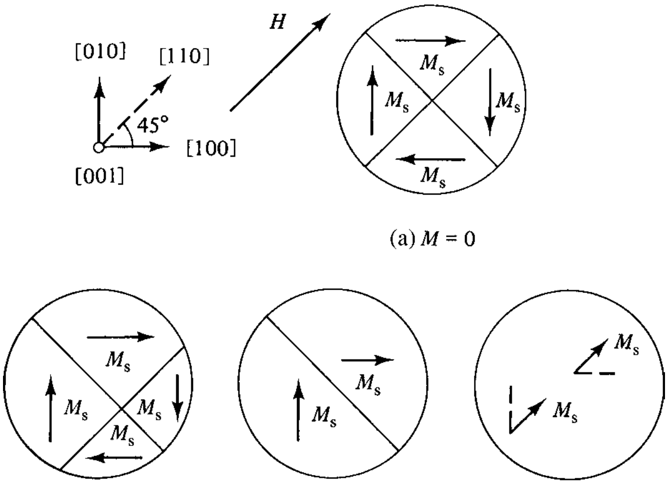

(a) $M = 0$

(b) $M > 0$ (c) $M = M_s \cos 45°$ (d) $M = M_s$

Figure 6: an increasing external field is applied away from the easy direction. The domain walls move and favor the domains with a component of magnetization along the field, reducing the dimensions of the other (b). When the domains are saturated in the easy directions, the spins rotate along the field direction (d).

Domain wall motion, in a low field, occurs until there are only two domains left (Fig. 6c), each with the same potential energy. The only way in which the magnetization can increase further is by rotation of the $M_S$ vector of each domain until it is parallel with the applied field. This process is called *domain rotation*. The domain itself, which is a group of atoms, does not rotate. It is the net magnetic moment of each atom which rotates. Domain rotation thus happens at very high field due to the magnetocrystalline anisotropy, this "force" which works to leave the magnetization in a specific direction.

When the rotation process is complete (Fig. 6d), the domain wall in Fig. 6c disappears, and the crystal is saturated.

Due to the fact that the domain rotation spends a certain amount of energy to be performed, there should be a great amount of energy stored in the material when the magnetization is not in the easy direction and this is called “crystal anisotropy energy”.

The Russian physicist Akulov showed in 1929 that this energy can be expressed in terms of a series expansion of the direction cosines of $M_s$ relative to the crystal axes. In a cubic crystal, let $M_s$ subtends angles a, b, c with the crystal axes, and let $\alpha_1, \alpha_2, \alpha_3$ be the cosines

of these angles, which are called direction cosines. Then

$$E = K_0 + K_1\left(\alpha_1^2\alpha_2^2 + \alpha_2^2\alpha_3^2 + \alpha_3^2\alpha_1^2\right) + K_2\left(\alpha_1^2\alpha_2^2\alpha_3^2\right) + ..$$

where $K_0$, $K_1$, $K_2$, . . are constants for a particular material at a particular temperature and are expressed in erg/cm$^3$ (cgs) or J/m$^3$ (SI). Higher powers are negligible, and sometimes $K_2$ is so small that the term involving it could be ignored. The first term, $K_0$, is independent of angle and is usually skipped, because normally we are interested only in the change in the energy E when the $M_s$ vector rotates from one direction to another. For example in a bcc crystal if $K_1$ is positive, then $E_{100} < E_{110} < E_{111}$, and [100] is the easy direction, because E is a minimum when $M_s$ is in that direction.

In the hexagonal Cobalt there is a unique easy axis and the other direction are equivalently hard. We speak of Uniaxial Anisotropy and the Akulov formula could be simplified as

$$E = K_0 + K_1\sin^2\theta + K_2\sin^4\theta + ..$$

Where θ is the angle between the magnetization and the c axis of the hexagonal structure.

When $K_1$ and $K_2$ are both positive, the energy E is minimum for $\theta = 0$, and the c-axis is an axis of easy magnetization. A crystal with a single easy axis, along which the magnetization can point either up or down, is referred to as a uniaxial crystal, as noted above. Its domain structure in the demagnetized state is particularly simple (figure 7). Elemental cobalt, barium ferrite, and many rare earth transitional metal intermetallic compounds behave in this way.

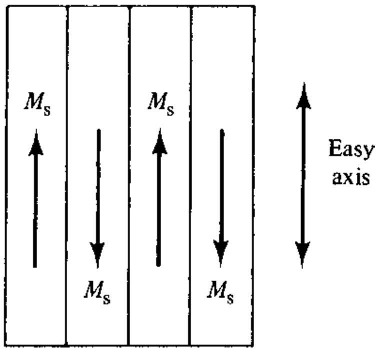

Figure 7: magnetization breaks in domains in uniaxial anisotropy crystals.

Crystal anisotropy is due mainly to spin-orbit interaction. The orbit of the electron is strongly linked to the lattice configuration. There is also a coupling between the spin and the orbital motion of each electron. When an external field tries to reorient the spin of an electron, the orbit of that electron also tends to be reoriented. But the orbit is strongly coupled to the lattice and therefore resists the attempt to rotate the spin axis. The energy required to rotate the spin system of a domain away from the easy direction, which we call the anisotropy energy, is just the energy required to overcome the spin–orbit coupling. Inasmuch as the “lattice” consists of a number of atomic nuclei arranged in space, each with its surrounding cloud of orbital electrons, we can also speak of a spin–lattice coupling and conclude that it too is weak. These several relationships are summarized in Fig. 8 (5)

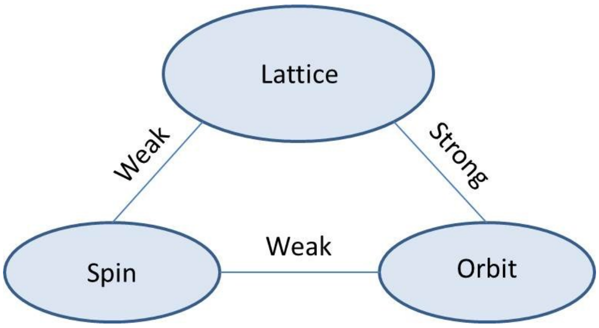

Figure 8: Spin-orbit coupling scheme.

The magnitude of the crystal anisotropy generally decreases with temperature more rapidly than the magnetization, and vanishes at the Curie point. Since the anisotropy contributes strongly to the coercive field, the coercive field generally goes to zero together with the anisotropy.

## Anisotropy Field

The crystal anisotropy forces which hold the spontaneous magnetization $M_s$ of any domain in an easy direction can also be expressed in an indirect but often useful way that doesn't make use of anisotropy constants. For small rotations of the magnetization away from an easy direction, the crystal anisotropy acts like a magnetic field trying to hold the magnetization parallel to the axis. This field is called the anisotropy field and is given the symbol $H_K$. The anisotropy field is parallel to the easy direction and its magnitude, for small angular deviations $\theta$, exerts the same torque on $M_s$ as the crystal anisotropy itself. The torque due to the anisotropy field is $H_K M_s \sin\theta$, or $H_K M_s \theta$ for small values of θ. For example, in a cubic crystal with [100] easy directions, the torque exerted on $M_s$ by the crystal when $M_s$ rotates away from [100] is, $+K_1/2\sin 4\theta$, or $2K_1\theta$ for small $\theta$.

Equating these torques, we have

$$H_K M_s \theta = 2K_1\theta$$

$H_K = \frac{2K_1}{M_s}$ or $H_K = \frac{2K_1}{\mu_0 M_s}$ in SI.

This is the expression for the Anisotropy Field in the case of magnetocrystalline anisotropy. As we will see in the next chapters it could be associated not only to magnetocrystalline anisotropy but extended to the other type of magnetic anisotropies.

## Induced Anisotropy

### Stress effects

When a substance is exposed to a magnetic field, its dimensions change. This effect is called magnetostriction. It was discovered in 1842 by Joule, who showed that iron in bulk form increased its length when it was magnetized lengthwise by a weak field (5).

The fractional change in length $\frac{\Delta l}{l}$ is simply a strain, and, to distinguish it from the strain $\varepsilon$ caused by an applied stress, we give the magnetically induced strain a special symbol:

$$\lambda = \frac{\Delta l}{l}$$

The value of $\lambda$ measured at magnetic saturation is called the saturation magnetostriction $\lambda_s$, and, when the word “magnetostriction” is used without qualification, $\lambda_s$ is usually meant. The origin of the magnetostriction could be understood looking at the image below (fig 9) (5).

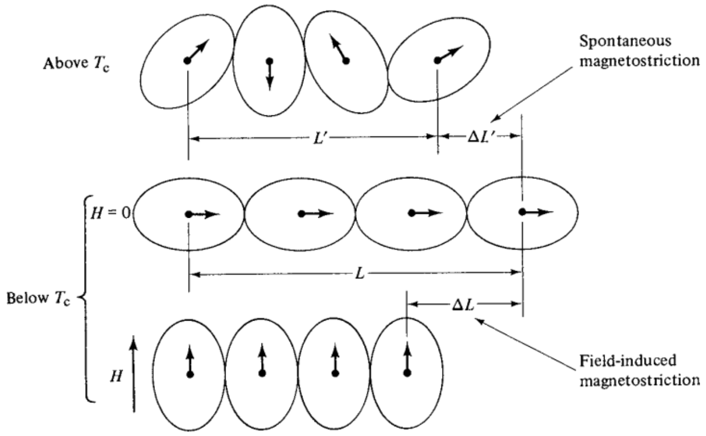

Figure 9: magnetostriction is caused by the rotation of the orbit around the nuclei.

The black dots represent atomic nuclei, the arrows show the net magnetic moment per atom, and the ellispoidal lines enclose the electrons in a fixed orbit around the nuclei in the magnetostrictive crystal. The upper row of atoms depicts the paramagnetic state above $T_c$. If, for the moment, we assume that the spin–orbit coupling is very strong, then the effect of the spontaneous magnetization occurring below $T_c$ would be to rotate the spins and the electron clouds into some particular orientation determined by the crystal anisotropy. The nuclei would be forced further apart, and the spontaneous magnetostriction would be $\frac{\Delta l_0}{l_0}$. If we then apply a strong field vertically, the spins and the electron clouds would rotate through 90 degrees, and the domains strain by an amount $\frac{\Delta l}{l}$.

Thus an applied mechanical stress can alter the domain structure and create a new source of magnetic anisotropy. These effects can have a substantial influence on the low-field magnetic properties, such as permeability and remanence.

The saturation magnetostriction $\lambda_{si}$ of a cubic crystal in a direction could be expressed as a function of the direction cosines $\beta_1$, $\beta_2$, $\beta_3$ relative to the crystal axes, when the magnetization changes from the demagnetized state to saturation in a direction defined by the direction cosines $\alpha_1$, $\alpha_2$, $\alpha_3$, and is given by

$$\lambda_{si} = \frac{3}{2}\lambda_{100}\left(\alpha_1^2\beta_1^2 + \alpha_2^2\beta_2^2 + \alpha_3^2\beta_3^2 - \frac{1}{3}\right) + 3\lambda_{111}\left(\alpha_1\alpha_2\beta_1\beta_2 + \alpha_2\alpha_3\beta_2\beta_3 + \alpha_3\alpha_1\beta_3\beta_1\right)$$

where $\lambda_{100}$ and $\lambda_{111}$ are the saturation magnetostrictions when the crystal is magnetized, and the strain is measured, in the directions [100] and [111], respectively.

The symbol σ will be used here and in the following paragraphs for applied mechanical stress.

H, M (or B), and σ could be all parallel, but, in general, M and σ may not be parallel. We know from the previous equation that the amount of magnetostrictive strain exhibited by a crystal in a particular direction depends on the direction of the magnetization. If we impose an additional strain by applying a stress, for the Villari effect we expect that the direction of the magnetization will change. We therefore need a general relation between the direction of M within a domain and the direction and magnitude of σ. But we know that, in the absence of stress, the direction of M is controlled by crystal anisotropy, as characterized by the first anisotropy constant $K_1$. Therefore, when a stress is acting, the direction of M is controlled by both σ and $K_1$. These two quantities are therefore involved in the expression for that part of the energy which depends on the direction of M, which is, for a cubic crystal

$$E = K_1\left(\alpha_1^2\alpha_2^2 + \alpha_2^2\alpha_3^2 + \alpha_3^2\alpha_1^2\right) - \frac{3}{2}\lambda_{100}\sigma\left(\alpha_1^2\gamma_1^2 + \alpha_2^2\gamma_2^2 + \alpha_3^2\gamma_3^2\right) - 3\lambda_{111}\sigma\left(\alpha_1\alpha_2\gamma_1\gamma_2 + \alpha_2\alpha_3\gamma_2\gamma_3 + \alpha_3\alpha_1\gamma_3\gamma_1\right)$$

Where $\alpha_1$, $\alpha_2$, $\alpha_3$ are the direction cosines of M, as before, and $\gamma_1$, $\gamma_2$, $\gamma_3$ are the direction cosines of the stress σ. The equilibrium direction of $M_s$ is that which makes E a minimum, and this direction is seen to be a complicated function of $K_1$, $\lambda_{100}$, $\lambda_{111}$, and σ, for any given stress direction $\gamma_1$, $\gamma_2$, $\gamma_3$.

Stress alone can create an easy axis of magnetization. Therefore, when stress is present, stress anisotropy must be considered. It is a uniaxial anisotropy, and the relation which governs it, is of exactly the same form as for uniaxial crystal anisotropy or shape anisotropy. We therefore write for the stress anisotropy energy, which is a magnetoelastic energy

$$E_{me} = K_{\sigma} \sin^2 \theta$$

## Configurational Anisotropy

It was demonstrated (3) that in a squared array of spins at least two different spatial configuration of the magnetization are equilibrium states of the magnetostatic energy.

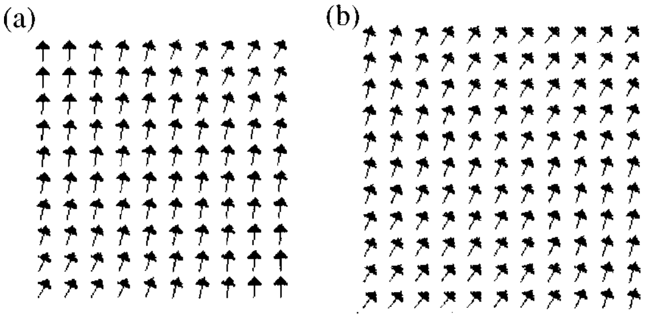

Figure 10: Flower (a) and Leaf (b) magnetization configuration are equilibrium states, created by the application of a field along the side or along the diagonal of the squared dot. This effect is called "configurational anisotropy".

It is possible (3) to model the flower and leaf (figure 10 a and b) states analytically as small perturbations from the uniformly magnetized state and find that the energy surface between the states can be described by a fourfold symmetric configurational anisotropy field which changes sign at a critical width to thickness aspect ratio. Figure 10 shows examples of equilibrium magnetization vector fields calculated for square nanostructures. Figure 10a shows the vector field (also called a configuration) which occurs when one magnetizes the structure parallel to one of its edges. This configuration is usually poetically named the 'flower' because of the way it flares out at the top and bottom, like the center of a daffodil. Figure 10b shows the configuration associated with a square magnetized along its diagonal. We name this configuration the 'leaf' because of the way that it bows out in the center and then nips together at the ends, like a plant leaf. The numerical calculation of an equilibrium magnetization field can be repeated for each value of a varying applied field in order to simulate a hysteresis loop, or as a function of nanomagnet orientation in order to predict anisotropy values.

The concept could be extended to “array of dots” and the configurational anisotropy will assume a more wide significance, as we will describe in the second part of this thesis.

## Other Anisotropies

Various other anisotropies may be induced in certain materials, chiefly solid solutions, by appropriate treatments. These induced anisotropies are of interest both to the physicist, for the light they throw on basic magnetic phenomena, and to the technologist, who may exploit them in the design of magnetic materials for specific applications (5).

The following treatments can induce magnetic anisotropy:

1. Magnetic annealing. This means heat treatment in a magnetic field, sometimes called a thermomagnetic treatment. This treatment can induce anisotropy in certain alloys. (Here the term “alloys” includes not only metallic materials but also mixed ferrites.) The results depend on the kind of alloy:

a. Two-phase alloys. Here the cause of anisotropy is the shape anisotropy of one of the phases and is therefore not basically new. However, it is industrially important because it affects the behavior of some of the alnico permanent-magnet alloys.

b. Single-phase solid-solution alloys

2. Stress annealing. This means heat treatment of a material that is simultaneously subjected to an applied stress.

3. Plastic deformation. This can cause anisotropy both in solid solutions and in pure metals, but by quite different mechanisms.

4. Magnetic irradiation. This means irradiation with high-energy particles of a sample in a magnetic field.

## Exchange Anisotropy

Another interesting small-particle effect was discovered in 1956 by W. H. Meiklejohn and C. P. Bean (8), who called it exchange anisotropy. They took fine, single-domain particles of cobalt and partially oxidized them, so that each cobalt particle was covered with a layer of CoO. A compact of these particles was then cooled in a strong field to 77K, and its hysteresis loop was measured at that temperature. This loop, shown by the full curve of Fig. 11, is not symmetrical about the origin but shifted to the left. If the material is not cooled in a field, the loop is symmetrical and entirely normal (dashed curve). The field-cooled material has another unusual characteristic: its rotational hysteresis loss $W_r$, measured at 77K, remains high even at fields as large as 16 kOe, whereas $W_r$ decreases to zero at high fields in most materials.

These two features of exchange anisotropy, a shifted loop and high-field rotational hysteresis, have been found in other materials, including alloys. For example, disordered nickel-manganese alloys at and near the composition $Ni_3Mn$ are paramagnetic at room temperature but show exchange anisotropy when field-cooled to low temperatures.

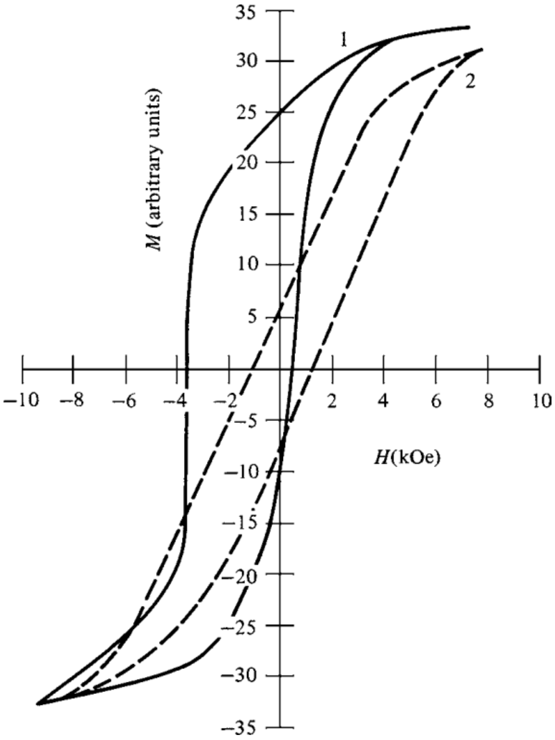

Figure 11: Asymmetric/symmetric hysteresis loop for a sample cooled/not in a field due to the effect of exchange anisotropy.

## Domains and magnetic configurations

In presence of a magnetization $\mathbf{M}$, the magnetic field $\mathbf{H}$ can be split in two components, the applied field $\mathbf{H}_{\mathbf{ext}}$ and the magnetostatic field $\mathbf{H}_d$, coming only from the magnetization $\mathbf{M}$. For $\mathbf{H}_d$ the following equation is valid: $\nabla \times \mathbf{H}_d = 0$, given that j = 0. The most general solution is $\mathbf{H}_d = -\nabla U(r)$. From the third Maxwell equation ($\nabla \cdot \mathbf{B} = 0$), being $\mathbf{B} = \mu_0 \left( \mathbf{M} + \mathbf{H} \right)$ and substituting $-\nabla U(r)$, it is obtained that $U(r)$ is solution of: $\nabla^2 U = \nabla \cdot \mathbf{M}$. Considering the boundary conditions, the solution of the equation can be calculated:

$$U(r) = \frac{1}{4\pi} \left( -\int_V \frac{\nabla' \cdot \mathbf{M}(r')}{|r - r'|} d\tau' + \int_S \frac{n \cdot \mathbf{M}(r')}{|r - r'|} d\mathbf{S}' \right)$$

From the equation above two terms can be identified: a bulk term ( $-\nabla \cdot \mathbf{M}$ ), that is zero when $\mathbf{M}$ is uniform everywhere and a surface term ( $\mathbf{n}\cdot\mathbf{M}$ ), that is zero when $\mathbf{M}$ is parallel to borders.

When a high external field is applied so that the sample reaches a saturated state, uniform magnetization is favoured. At small magnetic field, the magnetization is generally arranged in order to reduce the magnetostatic energy.

The way to do so is formation of domains structure, where the magnetization is arranged in a closed flux circuit without leakage outside the material. In each magnetic domain the magnetization is homogenous and oriented parallel to one of the easy directions. At the interface between one domain and the next, the magnetic spins have to change their orientation. Into the material there are then regions, called domain boundaries, which are costly in terms of energy (4) (9). An excess of anisotropy and exchange energy is stored in domain boundaries, considering that within the wall each spin is misaligned slightly from its neighbours, against the exchange energy that will tends to align the adjacent spins. On the other hand, these same atomic spins within the wall do not lie parallel to an easy direction, so there will be an anisotropy energy associated with the wall presence. Summarizing, the number and the shape of domains are determined by the balance of three energy terms: the magnetostatic energy and the anisotropy and exchange energies associated with the walls. When the lateral size of the ferromagnetic structure becomes to be so small that is comparable with the domain wall dimension, the magnetization configuration becomes a single domain. If then the size becomes too small, the magnetic moment of the single domain ferromagnet can fluctuate, due to the thermal energy, and the object becomes superparamagnetic (10).

In the simple ideal case, it is assumed that the rotation of the magnetization inside the wall is always normal to the magnetization on both the domains separated by the wall. This is the case of the Bloch wall domain. The energetic cost due to the presence of a domain wall can be evaluated as:

$$\sigma_W = \alpha\sqrt{AK_1}$$

where A is the exchange stiffness constant and α is a coefficient depending on the material, the type of boundary and the direction normal to the boundary.

Another type is the Néel wall domain: the magnetization rotates from the direction of the first domain to the direction of the second, with a rotation that is within the plane of the domain wall. It consists of a core with fast varying rotation and two tails where the rotation logarithmically decays. Néel walls are the common magnetic domain wall type in very thin film where the exchange length is very large compared to the thickness.

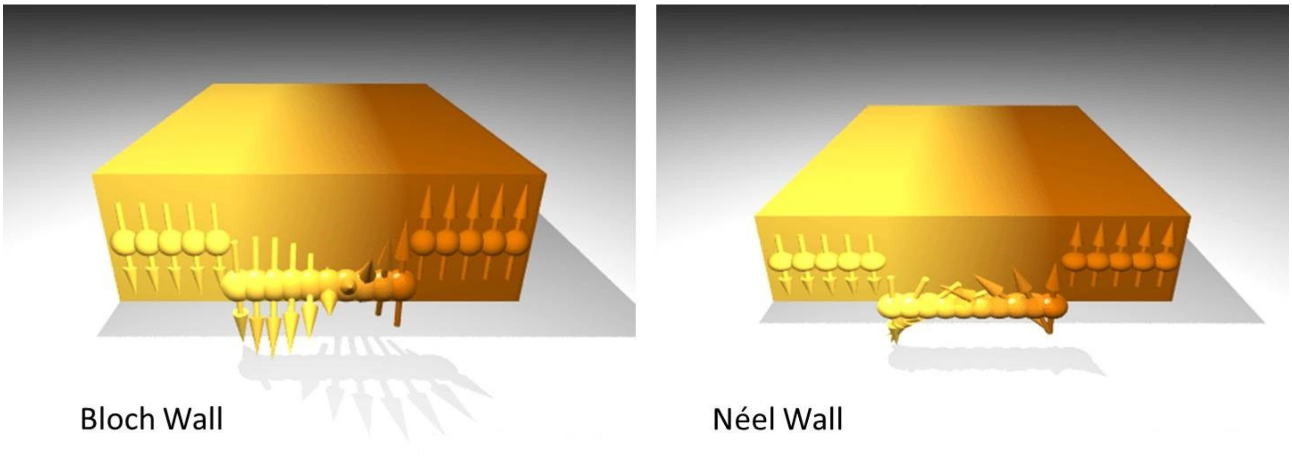

Figure 12: Bloch wall and Néel wall types.

## Specific length-scales

Considering the example of a spherical object with radius R and constituted by a specific material (so that A and $K_1$ are known) and calculating the energy for the single domain state and for a two domains state, the critical radius below which the former state is energetically stable can be written as (11):

$$\mathrm{R}_{\mathrm{sd}} = \frac{36\sqrt{AK_1}}{\mu_0 M_s^2}$$

The competition between exchange and dipolar energy can be expressed in terms

of the exchange length $l_{ex}$ (12):

$$l_{ex} = \sqrt{\frac{2A}{\mu_0 M_s^2}}$$

which represents the spatial scale below which exchange dominates on the magnetostatic effects.

Another important parameter is the hardness:

$$\kappa = \frac{2K_1}{\mu_0 M_s^2}$$

that measures the relative importance of anisotropy compared to magnetostatic effects.

The domain wall width parameter

$$\Delta = \sqrt{\frac{A}{K_1}} = \frac{l_{ex}}{\sqrt{\kappa}}$$

is related to the domain wall width $\delta_0$ is given by (12)

$$\delta_0 = \pi\sqrt{\frac{A}{K_1}} = \pi\Delta$$

The relative values of the characteristic lengths change as a function of the degree of magnetic hardness of the materials. For soft magnetic materials, one has:

$$\mathrm{R}_{\mathrm{sd}} \approx l_{ex} << \Delta$$

and for hard magnetic materials,

$$R_{sd} >> l_{ex} \geq \Delta$$

In the figure 13 (4) below we report some examples of magnetic domain structures in a rectangular ferromagnet. The magnetostatic energy is considerably reduced for the last two examples where a closure domain configuration is clearly visible.

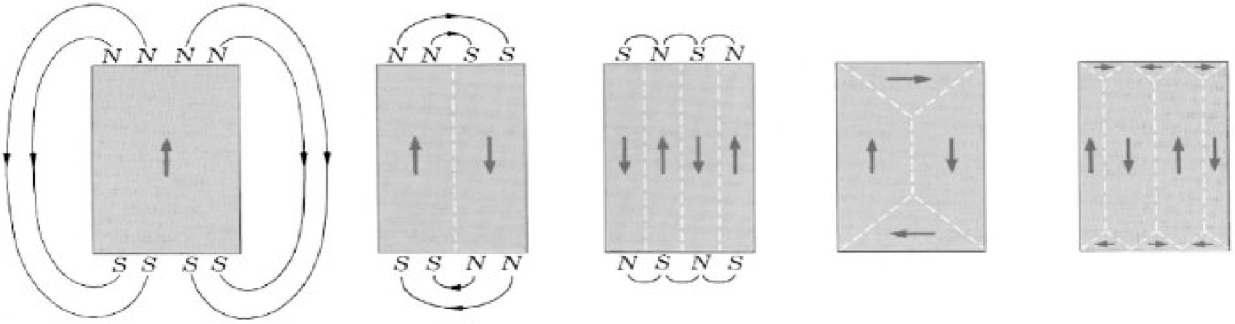

Figure 13: single domain, multi-domains and examples of closure domains.

The circular shape has a strong potential for nanomagnets, due to its lack of shape anisotropy and configurational anisotropy. If the circular dot is constituted by an isotropic material, as it is for Py, it results that its magnetization can be changed in direction by a very weak applied magnetic field. It is just in the circular objects that it appears a particular closure domain: the magnetic vortex (13), in which the magnetization direction changes in the plane of the object, lowering the system energy by reducing the stray field. In the core the magnetization is perpendicular to the surface plane, so the only residual magnetostatic energy is confined in the center which could be seen as a topological singularity, that gives to the object two key properties: chirality (clockwise or counterclockwise rotation of magnetization) and polarity (positive or negative direction of the core magnetization). A scheme of the magnetization orientation in a vortex is represented in image 14.

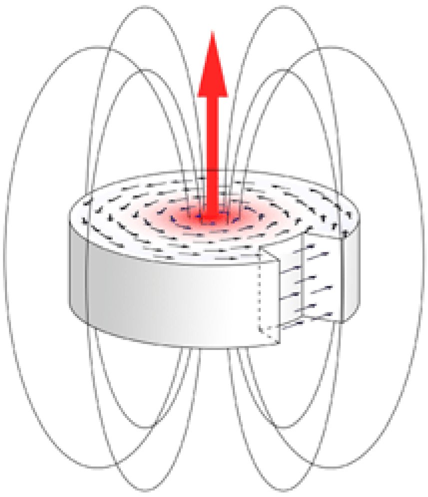

Figure 14: magnetization distribution in a vortex. The topological singularity determines the polarity; the chirality indicates the rotation of the magnetization.

## Reversal of Magnetization

When the particle lateral dimensions begin to be small, the single domain is energetically more favorable and the reversal nucleation field is greater in than the extended film. This means that the coercivity increases when the particle dimension is reduced. We report in figure 15 a scheme in which the coercivity as function of the particle dimension is summarized. We see that as we go from right to left (when we reduce the diameter of the particle) the coercivity increases.

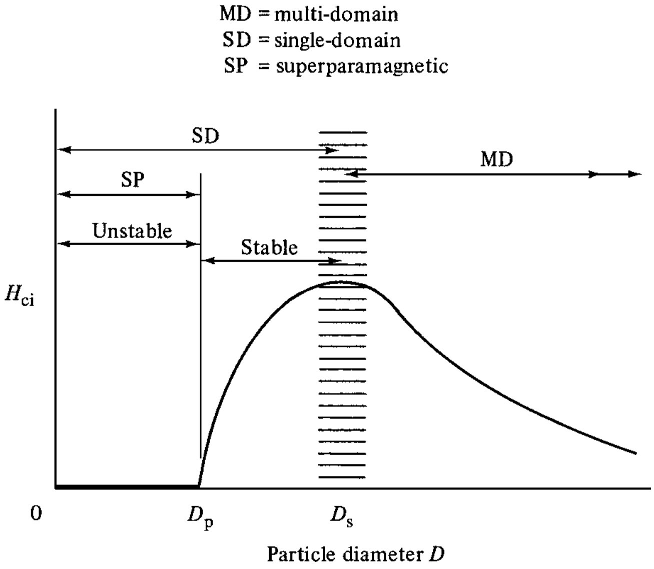

Figure 15: as the dimensions of the particle are reduced, the single domain is favored and as consequence the coercive field grows. If the dimensions are still reduced, the thermal excitations misalign the spins in a chaotic distribution (superparamagnetic behavior) and the coercive reduces to zero.

When the diameter of the particle is further reduced the coercivity starts to reduce and when the thermal energy is greater than the magnetic energy the particle becomes superparamagnetic due to the thermal excitations which misalign the spin orientation. The magnetization reversal process is energetically favored if it passes through a domain wall motion, but when the particle is single domain the nucleation field is still smaller than that for coherent reversal. Two different mechanism of incoherent spin rotation, the magnetization buckling and magnetization curling, are now energetically favoured as sketched in Figure 16 (14).

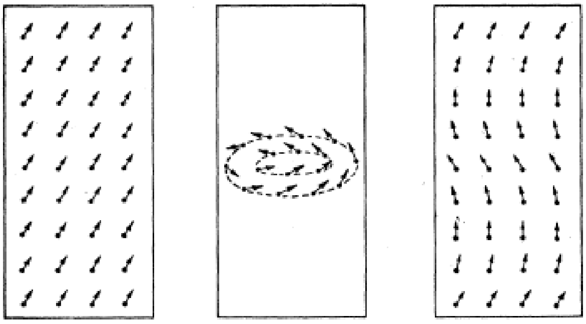

Figure 16: coherent rotation, curling and buckling reversal mechanism.

## Particle interaction

In a magnetic nanodots array the only interaction between the particles is the dipolar interaction (or dipolar coupling) that acts in the long range, because its magnitude scales as $r^{-3}$

It derives from the magnetic dipole-dipole interaction which would favor the alignment of the magnetization of a particle to the stray-closure flux produced by the neighbor particle. In figure 17 it is simply sketched the dipolar influence of the uniformly magnetized particle A on the particle B and C.

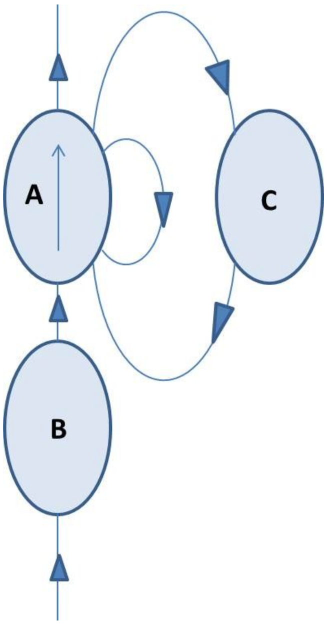

Figure 17: coupling interactions between magnetic particle.

The particle C tends to be magnetized antiparallel to A, while the particle B prefers a magnetization in the same versus of the particle A.

For circular magnetic dots in an array the coupling interaction favors vortexes with identical chirality and polarity (15).

It is not trivial to understand how the coupling interaction affect the reversal process in a magnetic dot array for different dimensions and relative dispositions, but it was one of the objective of the work done.

## Spin Waves

Spin waves are propagating disturbances in the ordering of magnetic materials. These collective excitations occur in magnetic lattices with continuous symmetry. From the equivalent quasiparticle point of view, spin waves are known as *magnons*, which are boson modes of the spin lattice that correspond roughly to the phonon excitations of the nuclear lattice. As temperature is increased, the thermal excitation of spin waves reduces a ferromagnet's spontaneous magnetization. The energies of spin waves are typically only μeV. Spin waves can propagate in magnetic media with magnetic ordering such ferromagnets and antiferromagnets. The frequencies of the precession of the magnetization depend on the material and its magnetic parameters; in general precession frequencies are in the microwave from 1–100 GHz, exchange resonances in particular materials can even see frequencies up to several THz. This higher precession frequency opens new possibilities for analogue and digital signal processing.

Spin waves themselves have group velocities on the order of a few km per second. The damping of spin waves in a magnetic material also causes the decay of amplitude of the spin wave with distance, meaning that the spin waves can travel usually only several 10's of μm. The damping of the dynamical magnetization is accounted by the Gilbert damping constant in the Landau-Lifshitz-Gilbert equation (LLG equation).

The LL equation was introduced in 1935 by Landau and Lifshitz to model the precessional motion of magnetization M in a solid with an effective magnetic field $H_{eff}$ and with damping. Later, Gilbert modified the damping term, and in the limit of small damping yields the older LL equation. The LLG equation is,

$$\frac{\partial M}{\partial t} = -\gamma \mathbf{M} \times \mathbf{H_{eff}} + \frac{\alpha}{M_s} \mathbf{M} \times (\mathbf{M} \times \mathbf{H_{eff}})$$

The constant α is the Gilbert phenomenological damping parameter and depends on the solid; γ is the electron gyromagnetic ratio.

A *magnonic crystal* is a magnetic meta-material with alternating magnetic properties. Like conventional metamaterials, their properties arise from geometrical structuring, rather than their band-structure or composition directly. Small spatial inhomogeneities create an effective macroscopic behavior, leading to properties generally not found in nature. By alternating parameters such as the relative permeability or saturation magnetization, there exists the possibility to tailor 'magnonic' bandgaps in the material. By tuning the size of this bandgap, only spin wave modes able to cross the bandgap would be able to propagate through the media, leading to selective propagation of certain spin wave frequencies (16).

## The Micromagnetic modeling

The full quantum mechanical approach is used when the dimensions of the nanostructures are of the order of atoms and molecules, while in the mesoscopic range phenomenological constants (i.e. the exchange constant, anisotropy fields) are introduced.

In the mesoscopic scale a classical approximation of the description of the magnetic materials called “micromagnetic approach” is introduced and the discrete nature of the matter is neglected.

In the micromagnetic theory the total free energy is a result of several terms, whose balance determines the magnetic properties of the system. In physics (and therefore in this theory) a system in equilibrium is in a local minimum of the total free energy. If thermal fluctuations are not considered, i.e. the system is at 0 K, this can be written as:

$E_{tot} = E_d + E_{ex} + E_Z + E_{anis}$

where $E_d$ is the magnetostatic energy, $E_{ex}$ is the exchange energy, $E_Z$ is the Zeeman energy and $E_{anis}$ is the anisotropy energy. The determination of the exact values of all these terms, and in particular the condition under which they are in a local minimum, allows us to predict the magnetic behavior of the considered system.

# Experimental Methods

## Introduction

The present thesis work concerns an experimental analysis and characterization of some novel nanostructured systems: FeGa (produced by the group of Prof. Marangolo at the University Pierre et Marie Curie in Paris) and TbFeGa (produced by Rocio Ranchal at University Complutense in Madrid) in thin films, bicomponent array of ferromagnetic ellipses (done by the group of prof Adeyeye at University of Singapore) and finite-size array of Py nanodots (by the group of Vavassori at Cic Nanogune in San Sebastian, Spain).

The main methods for detection of the magnetic properties were Magnetic Force Microscopy, for the determination and visualization of the magnetization configuration, the Magneto-Optical Kerr Effect Magnetovectometry for the determination of the variation of magnetization under the field application in the three spatial directions, the Vibrating Sample Magnetometer and finally the Brillouin Light Scattering for the analysis of the spin-wave frequencies. MFM and MOKE are measurements performed with instruments at the University of Ferrara, VSM at the UPMC while BLS is performed at the Department of Physics and Geology of the University of Perugia.

## Magnetic Force Microscopy

The Magnetic Force Microscope is a type of Scanning Probe Microscope. The principle of operation is based on the scheme reported in the image 1 (17).

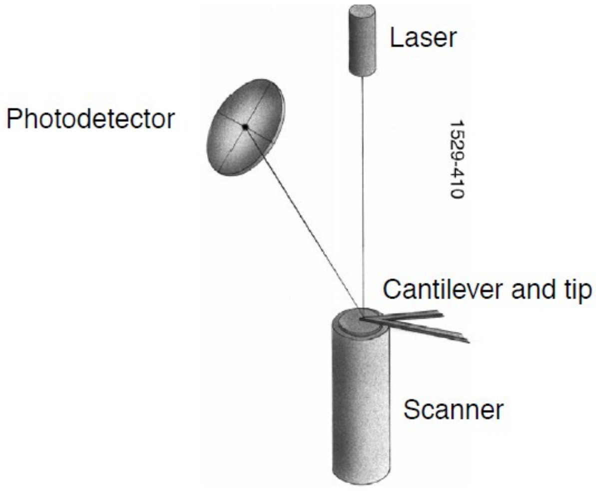

Figure 1: scheme of the principle of operation of SPM.

A laser beam is focused over a reflecting “cantilever” which is suspended on one side. On the free end a small volume of magnetic material, the tip, is mounted. When a magnetic surface is brought close to this tip they will interact by the magnetic stray field. Magnetic force  microscopy is a non-contact technique and during scanning the sample is kept at a distance of several nanometers from the tip. The interaction between tip and sample can be measured by a detector which collects the laser beam reflected by the back side of the cantilever. When the sample is moved with respect to the tip a one dimensional array of interaction data is put into the computer and stored there. The direction of this motion is called the fast scale direction (X). A number of parallel scan lines will form a two-dimensional array of data in the computer. The direction of the offset between these lines is called the slow scan direction (Y). A computer assigns grey color with different contrast to different strengths of interaction forming a microscopic image of the interaction in the sample surface.

In an MFM two basic detection modes can be applied which are sensitive to two different types of interaction. The static (or DC) mode detects the magnetic force acting on the tip whereas the dynamic (or AC mode) measures the force derivative (18).

## Static Mode

According to Hooke's law the displacement Δz of the cantilever is proportional to the force F that it exerts on the tip:

$F = - c \Delta z$

The proportionality constant c is called the cantilever constant. In this mode the cantilever is used to translate the force acting on the tip to a displacement which can be measured by the detector. The detector signal and thus the magnetic image will be a direct measure of the force acting in the cantilever.

## Dynamic Mode

In the dynamic mode the cantilever is oscillated at or close to its resonance frequency. The cantilever can be treated as a harmonic oscillator having the resonance frequency *f*, which is given by

$$f = \frac{1}{2\pi}\sqrt{\frac{c_{eff}}{m}}$$

with m the effective mass of tip and cantilever. The effective cantilever constant $c_{eff}$ consists of two contributions:

$$c_{eff} = c - \frac{\partial F}{\partial z}$$

where c is the cantilever constant. In the close proximity of the sample also the forces acting on the magnetic tip change when the distance between tip and sample is changed. This can be described by a force derivative $\frac{\partial F}{\partial z}$ . This force derivative on the tip acts on the cantilever just like an additional cantilever constant. Note that in case of a large cantilever oscillation amplitude the force derivative will not be constant over one period, resulting in a non-harmonic oscillation. For low amplitudes, however, a constant $\frac{\partial F}{\partial z}$ can be assumed so that the problem can still be treated as an harmonic oscillator:

$$f = \frac{1}{2\pi}\sqrt{\frac{c - \frac{\partial F}{\partial z}}{m}}$$

From this it can be shown that a force derivative $\frac{\partial F}{\partial z}$ changes the cantilever resonant frequency to

$$f = f_0\sqrt{1 - \frac{\frac{\partial F}{\partial z}}{c}}$$

with $f_0$ the free resonance frequency of the cantilever in the case of no tip sample interaction provided that $\frac{\partial F}{\partial z} \ll$ the shift in resonant frequency is given by:

$$\Delta f \approx \frac{1}{2c}\frac{\partial F}{\partial z}$$

We know that

$F \propto M_{tip}\frac{\partial}{\partial z}B$ and thus the frequency shift is proportional to the second derivative of the magnetic stray field along z:

$$\Delta f \propto \frac{\partial^2 B}{\partial z^2}$$

There are three ways to detect this change of the cantilever resonance frequency:

- Amplitude detection: here the cantilever is oscillated at a fixed frequency $f_{ex} > f_0$ , where in the case of $\frac{\partial F}{\partial z} = 0$ the oscillation amplitude is already slightly below the maximum amplitude at $f_0$. When the resonance frequency changes this will result in a change in cantilever oscillation amplitude which can easily be detected. The disadvantage of this technique is that it is very slow for the cantilevers with low damping and that a change in cantilever damping will be misinterpreted as change in resonance frequency.
- Frequency detection: in this method the cantilever is oscillated directly at its resonance frequency, using a feedback amplifier with amplitude control. The change in resonance frequency can be directly detected by FM demodulation techniques. Also in this case the images had to be interpreted very carefully since an increase in cantilever damping can also reduce the resonance frequency. A comparison of the static and dynamic mode favors the dynamic mode for high resolution (18).
- Finally there is another method for the measurement of the force acting on the cantilever and is the "*phase shift detection mode*": it measures the phase difference between the frequency voltage that drives the cantilever oscillation and the true cantilever response. The shift on the cantilever response depends on its damping constant. This is the method we used in all our measurements in this thesis word.

## Magnetic Forces on the tip

A magnetized body, brought into the stray field of our sample, will have the magnetic potential energy:

$$E = -\mu_0 \int \mathbf{M}_{tip} \cdot \mathbf{H}_{sample} dV_{tip}$$

The force acting on an MFM tip can thus be calculated by:

$$F = -\nabla E = -\mu_0 \int \nabla \left( \mathbf{M}_{tip} \cdot \mathbf{H}_{sample} \right) dV_{tip}$$

The integration of this equation has to be carried out over the tip volume. In order to simplify calculations often simple point dipole, elongated dipole or monopole models are used for the tips. Calculations have been carried out about the MFM response of more complicated tips on different kinds of magnetic structures (18).

## Non magnetic forces on the tip

Different other forces also act on the tip. With increasing distance these forces have a different decay rate which is indicated in the figure 2 (18).

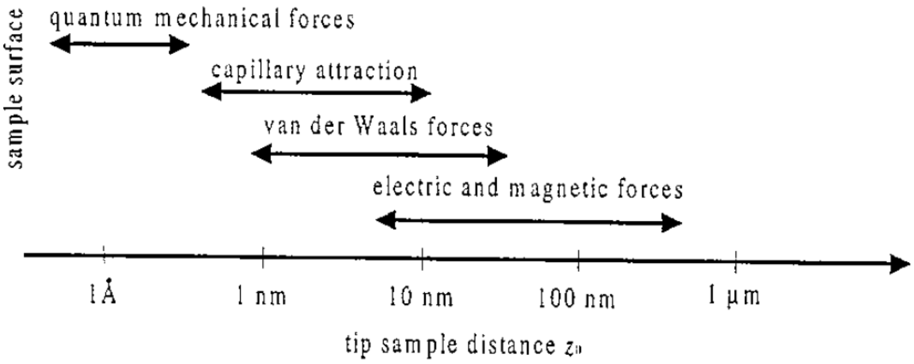

Figure 2: action of attractive and repulsive forces and their working distances.

### *Electrostatic forces*

Above 10 nm distance between tip and sample surface next to the magnetic forces also electrostatic forces are the most important influence on the tip. The electrostatic force is given by:

$$F_{el} = \frac{\partial C}{\partial z} V_{ts}^2$$

Where C is the electrical capacity between tip and sample and $V_{ts}$ is the applied voltage. For a conductive tip this force is always attractive, even if both tip and sample have the same voltage. In the case of an insulating sample, electric surface charges can act on the tip by Coulomb forces. On insulator, due to the scanning motion even charging can occur. Usually these two effects are not important for magnetic media, since the materials are conductive enough. In constant signal mode operation often a voltage is applied between tip and sample to keep the overall force (force derivative) positive so that a regulation loop can keep it constant. This technique is called biasing (18).

### *Van der Waals Force*

Below 10 nm tip-sample distance the influence of the Van der Waal force increases. This type of force originates from the induced electromagnetic dipole-dipole interaction between atoms. In general between two atoms a decay of $r^{-7}$ can be assumed for this force. The magnetic dipolar interaction instead decays as $r^{-3}$. For this reason when the tip is very close to the sample surface, the Van Der Walls forces are very strong, but when the tip is lifted the Van Der Walls forces rapidly decrease while the dipolar interaction remains strong. This is the principle on which the MFM works: in the first pass the tip is kept close to the surface and it feels the Van der Walls forces and in this way it traces the topography. Knowing the topography it is possible to pass a second time with a fixed lift height at which the Van der Walls forces are neglectable but magnetic forces are still strong and in this way only the magnetic forces are accounted for.

### *Capillary Forces*

If measurements are performed in ambient conditions capillary forces need to be accounted for if the radius of the contact is less than the Kelvin radius. Below this dimension vapors (usually water) condense into the contact area. The Kelvin radius is given by

$$r_K = \frac{\gamma V}{RT\log(p/p_s)}$$

where $\gamma$ is the surface tension, R is the universal gas constant, T is the temperature, V is the molar volume and $p_s$ is the saturation vapor pressure. Due to the large tip-sample separations capillary forces are assumed to be negligible in this study.

## The Multimode SPM – Nanoscope IIIa

The instrument in our laboratory is a Digital Instruments Nanoscope IIIa. The image of the head of the microscope is reported below in figure 3 (17).

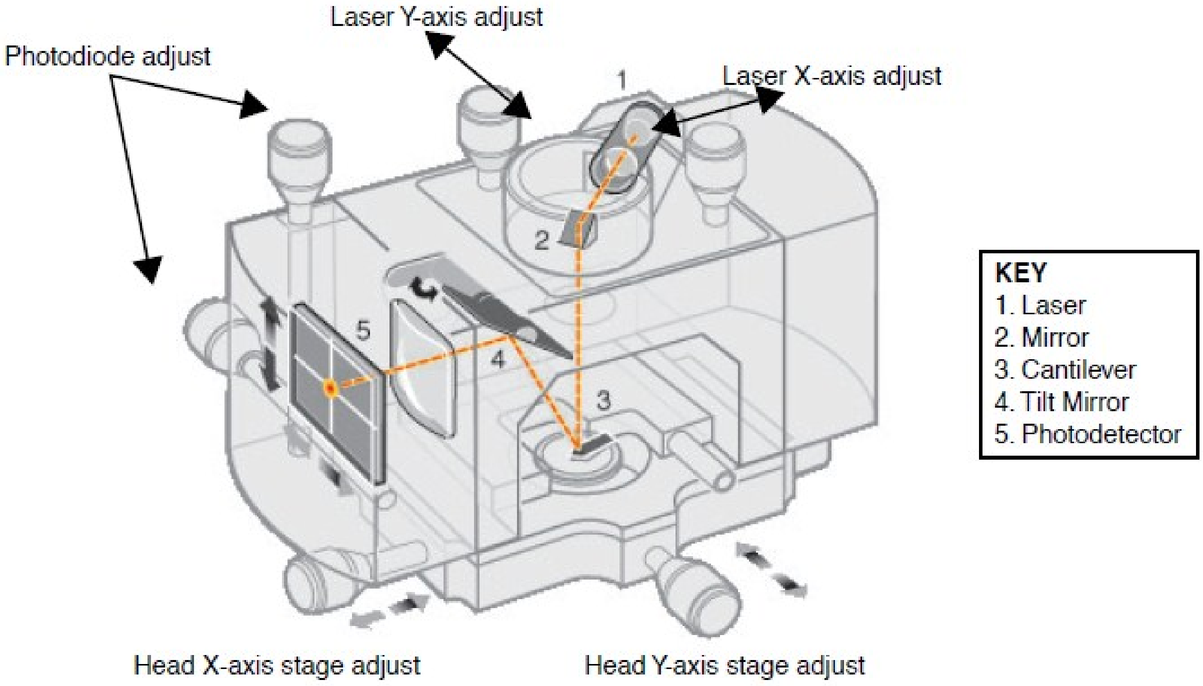

Figure 3: representation of the “head” of the MFM

Images consist of raster-scanned, electronic renderings of sample surfaces. There are three default sizes: 128 x 128 pixels, 256 x 256 pixels, and 512 x 512 pixels. In addition, nine width-to-height aspect ratios may be specified by the user: 1:1, 2:1, 4:1, 8:1, 16:1, 32:1, 64:1, 128:1 and 256:1.

Thus, it is possible to obtain “strip scans” which require less time to capture. One can scan up to 200µm laterally (in X and Y) and 10µm vertically (Z axis).

The MultiMode is so called because it offers multiple SPM modes, including AFM, ECAFM, ECSTM, STM and TappingMode. With this instrument it is possibile to perform AFM measurements of the topography following different method:

**Contact AFM**—Measures topography by sliding the probe tip across the sample surface. Operates in both air and fluids

**TappingMode AFM**— Measures topography by tapping the surface with an oscillating tip. This eliminates shear forces which can damage soft samples and reduce image resolution. This is now the technique of choice for most AFM work.

**Phase Imaging**—Provides image contrast caused by differences in surface adhesion and viscoelasticity.

**Non-contact AFM**—Measures topography by sensing Van der Waals attractive forces between the surface and the probe tip held above the surface. It provides lower resolution than either contact AFM or TappingMode.

**Interleave MODE** is a feature of NanoScope software which allows the simultaneous acquisition of two data types. After each main scan line trace and retrace (in which topography is typically measured), a second (Interleave) trace and retrace is made with data acquired to produce an image concurrently with the main scan. Typical applications of interleave scanning include MFM (magnetic force microscopy). During the interleave scan, the feedback is turned off and the tip is lifted to a user selected height above the surface to perform far field measurements such as MFM. The lift mode measures MFM or other long range interaction in the second pass, while in the first pass the topography is measured in tapping mode at a smaller distance at which Van der Waals forces prevail figure 4 (17).

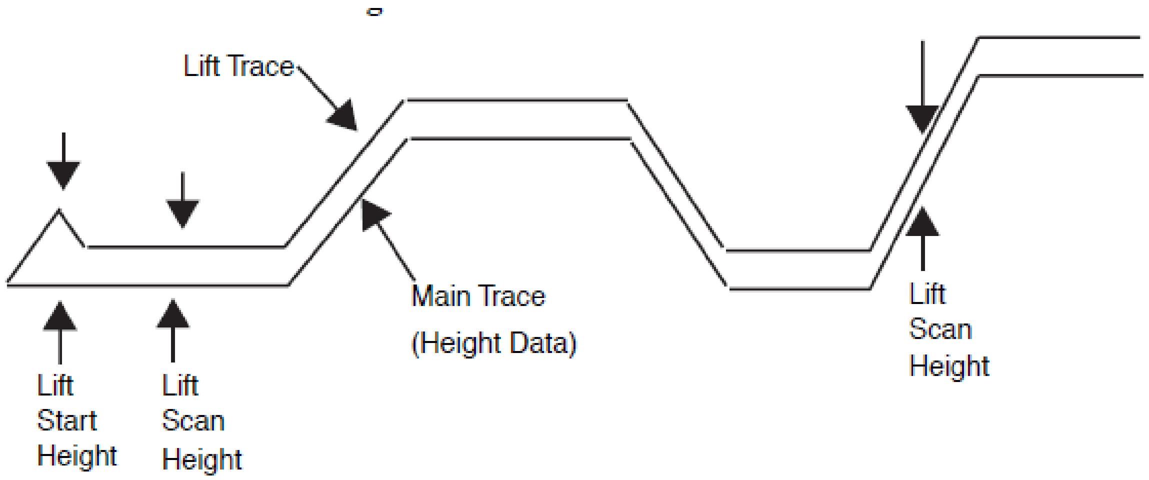

Figure 4: scheme of the lift operation mode; in the first pass the microscope traces the topography; the second pass is performed at a fixed distance (lift distance) at which long range forces (like magnetic coupling interaction) prevail.

The four elements of the quad photodiode (position sensitive detector) are combined to provide different information depending on the operating mode. In all modes the four elements combine to form the SUM signal. The amplified differential signal between the top two elements and the two bottom elements provides a measure of the deflection of the cantilever. This differential signal is used directly in the contact AFM. It is fed into an RMS converter (or phase module if attached) for TappingMode operation.

Figure 5 (17) shows the arrangement of the photodiode elements in the MultiMode head. Different segments of the photodetector are used for generating AFM and LFM (lateral force microscope) signals.

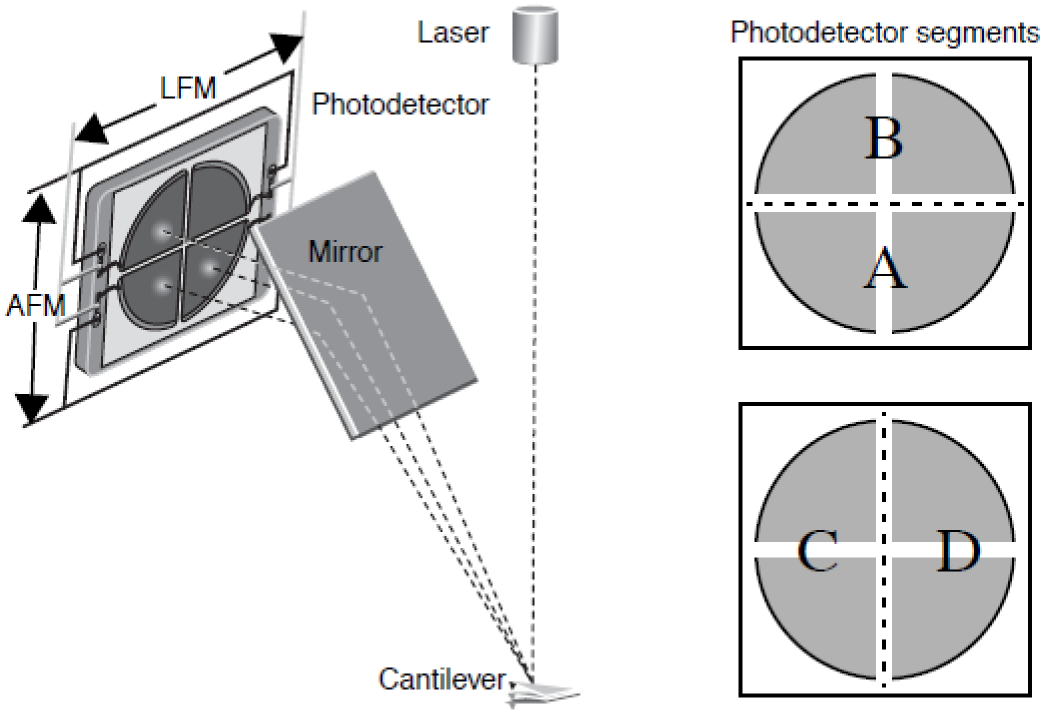

Figure 5: the four elements photodiode for the analysis of the reflected beam, the interpretation of the detected signal is performed by the software.

A version of the TappingMode tip is the MFM probe. This is basically a crystal silicon TappingMode probe having a magnetic coating on the tip. As the magnetized tip oscillates through magnetic fields on the sample surface, it modulates the cantilever’s phase and frequency. These are monitored, providing a measure of magnetic field strength and providing images of magnetic domains.

AC voltages applied to the scanner crystal X-Y axes produce a raster-type scan motion as represented in Figure 6.

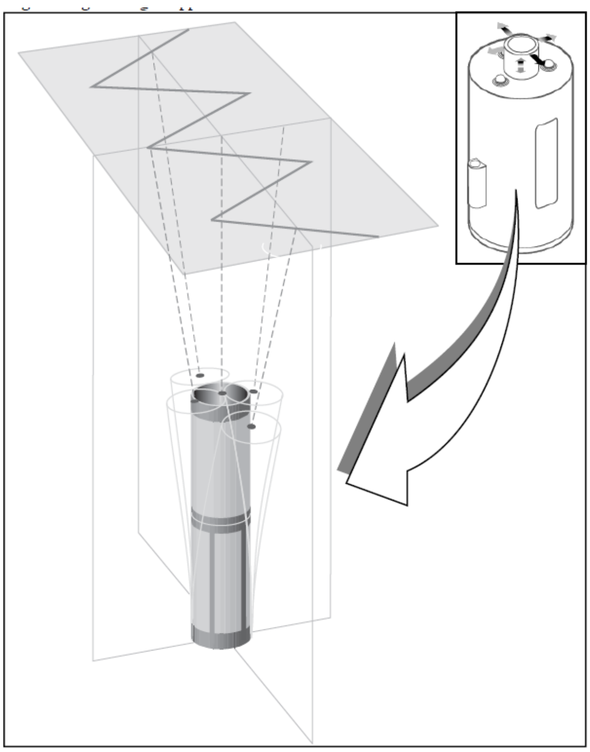

Figure 6: the x-y scanner is moved by piezo-element actuators.

## Magneto-Optical Kerr Effect

The magneto-optical Kerr effect (MOKE) is a technique employed to investigate the magnetization mechanisms of some sample discussed in this work. Therefore it is helpful to describe the physical basics and the measurements setup of this technique.

### Introductory arguments

In the magneto-optical Kerr effect (MOKE) (19) the interaction between a polarized light and magnetization of a ferromagnetic sample causes the change of polarization and/or intensity of the light beam reflected by the sample surface. The transmission analogous to the Kerr effect is the Faraday effect, where the polarization of the light beam transmitted through the ferromagnetic material is changed from the polarization of the incident light beam (20). The Kerr effect can be observed in three different dispositions of the magnetization with respect to both the plane of incidence of the light and the sample reflecting surface (21) (figure 7).

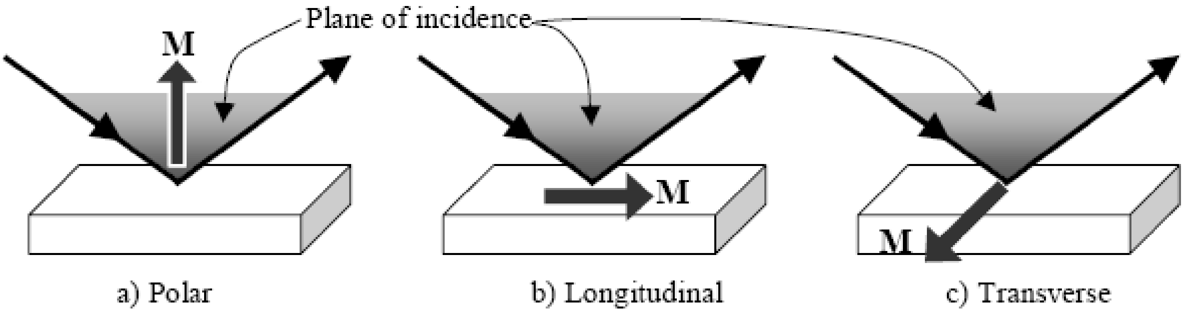

Figure 7: Polar, Longitudinal and Transverse configuration depending on the orientation of the incidence plane with respect to the magnetization vector.

In the polar configuration the magnetization is perpendicular to the sample surface and it is performed at normal incidence. Longitudinal and transverse MOKE operate at a certain angle of incidence, with a magnetization parallel to the sample surface, either parallel (longitudinal) or perpendicular (transverse) to the optical plane of incidence. The simplest model to explain the MOKE phenomenon is to consider a Lorentz-Drude theory for a metallic film. The incident light causes an electrons oscillation parallel to the plane of polarization. In the presence of a non-ferromagnetic sample, the polarization plane of the reflected light is the same as the incident light. When the sample has a magnetization that acts on the oscillating electrons through a Lorentz force, like an internal magnetic field, the result is a second oscillating component perpendicular to the direction of the magnetization and to the primary motion. Using a linearly polarized incident light, the polar and longitudinal MOKE yield the orthogonally polarized component upon reflection whereas the transverse geometry only affects the intensity, i.e. the amplitude of the incident polarization (22). However, the complexity of MOKE theory requires a quantum description, that stems from the need for explaining the large magneto-optical effect in the ferromagnetic materials (23). The explanation could be found in the spin-orbit coupling, introduced by Hulme (24) and improved by Kittel (25) and Argyres (26). The spin-orbit interaction couples the magnetic moment of the electron with its motion, connecting the magnetic and optical properties of a ferromagnet. This effect is present also in the non-magnetic materials, but it is only in the ferromagnets that it manifests itself thanks to the unbalanced number of spin up and spin down electrons.

## Mathematic formalism

The formalism to explain the MOKE effect is the same used for the other magneto-optical effects. If we consider a linearly polarized light as a superposition of right and left circularly polarized light, we see how, without an external magnetic field, a left-circularly polarized light will drive the electrons into left circular motion and a right-circularly polarized light will drive the electrons into right circular motion. The radius of the electron orbit for left and right circular motion will be the same and, since the electric dipole moment is proportional to the radius of the circular orbit, there will be no difference between the dielectric constants for both circularly polarized electromagnetic waves.

An interesting effect occurs when dealing with a ferromagnetic sample because a net Lorentz force acts on the electrons due to the magnetization of the sample. The Lorentz force introduces an additional small oscillating component to the motion of the electrons in the perpendicular direction both to the magnetization and to the displacement of the electrons. By superimposing the contributions, with their relative phases, the reflected light will result in an elliptical polarization state (27).

Considering the polar Kerr effect at normal incidence, the complex refraction index of the sample is $n_+$ for the right circularly polarized light and $n_-$ for the left circularly polarized light, where $n_\pm$

can be conceived (4) as $n(1 \pm \frac{1}{2}Q)$. $Q$ is the Voigt magneto-optical constant, that is proportional to the value of the magnetization in the linear approximation. The reflected amplitude, such as the Fresnel coefficient, will be:

$$\mathrm{r} = |r| e^{i\phi} = \frac{E_1}{E_0} = -\frac{n-1}{n+1}$$

Therefore, it is that:

$$\frac{r_+}{r_-} = \left|\frac{r_+}{r_-}\right| e^{i(\phi_+ - \phi_-)}$$

using the indices + and – to denote, for each quantity, the right and left circularly polarized light, respectively. If the incident light is linearly polarized, the reflected light will be elliptically polarized because the circular components, in which it is decomposed, will no longer have equal amplitude and the major axis will be rotated from the direction of incident polarization because of the phase difference introduced between these circular components (4) (28). This rotation angle, the Kerr rotation, is given by:

$$\vartheta_K = -\frac{1}{2}(\phi_+ - \phi_-)$$

considering that the minus sign is due to the reflected light travelling in the negative direction, in accordance with a coordinate system where the z direction is positive if going into the sample surface.

The Kerr ellipticity will be instead:

$$\varepsilon_K \frac{|r_+| - |r_-|}{|r_+| + |r_-|}$$

To first order in $(\mathrm{n}_+ - \mathrm{n}_-)$ such as to first order in Q, the two terms become:

$$\vartheta_K = \Phi\left(\frac{\mathrm{n}_+ - \mathrm{n}_-}{\mathrm{n}_+\mathrm{n}_- - 1}\right) = \Phi\left(\frac{\mathrm{nQ}}{\mathrm{n}^2 - 1}\right)$$

$$\varepsilon_K = \mathrm{E}\left(\frac{\mathrm{n}_+ - \mathrm{n}_-}{\mathrm{n}_+\mathrm{n}_- - 1}\right) = \mathrm{E}\left(\frac{\mathrm{nQ}}{\mathrm{n}^2 - 1}\right)$$

The relation among the components of the magnetization, the Voigt constant Q and the Kerr rotation and ellipticity, can be resumed introducing the dielectric tensor of the medium $\varepsilon$, that can be decomposed into a symmetric, thus diagonalizable and an antisymmetric part, that gives rise to the Kerr effect.

Considering a thick magnetic film where the multiple reflections could be ignored (29), when a light beam is incident on this ferromagnetic medium 1, from a non-magnetic medium 0, the dielectric tensor $\varepsilon$ can be written as:

$$\varepsilon = \varepsilon_{xx}\begin{pmatrix} 1 & -iQm_z & iQm_y \\ iQm_z & 1 & -iQm_x \\ -iQm_y & iQm_x & 1 \end{pmatrix}$$

$m_i$ are the direction cosines of the magnetization vector $M_s$ and Q is the already cited Voigt magneto-optical constant. At this point is useful to clarify that there are two different sign formalisms to describe the dielectric tensor and also the sense of magneto-optically induced rotations and ellipticities (4) (30). The coordinate system and the sign convention chosen in this treatment (4) are the same used by Ref. (31) and Ref. (32).

The reflection from the sample can be evaluated through the Fresnel reflection matrix:

$$R = \begin{pmatrix} r_{pp} & r_{ps} \\ r_{sp} & r_{ss} \end{pmatrix}$$

where the terms $r_{ij}$ are the Fresnel reflection coefficients, with the indices j and i related to the polarization of the incident and reflected electric field, respectively; *s* is the polarization state perpendicular to the plane of incidence, whereas *p* is the polarization state parallel to the plane of incidence. The complex Kerr angle can be now written as:

$$\theta_K^p = \vartheta_K^p + i\varepsilon_K^p = \frac{r_{sp}}{r_{pp}} \quad , \quad \theta_K^s = \vartheta_K^s + i\varepsilon_K^s = \frac{r_{ps}}{r_{ss}}$$

with $\vartheta_K$ and $\varepsilon_K$ the Kerr rotation and ellipticity.

The $r_{ij}$ will be dependent on magnetization components, refractive index and refraction angle inside the ferromagnetic medium, in different way depending on the geometry of the magnetization in relation to the plane of incidence and the sample plane.

The investigations performed in the longitudinal geometry (magnetization parallel to the plane of incidence), have $m_y = 1$ and $m_x = m_z = 0$, the coefficients $r_{ij}$ are expressed by (33):

$$r_{pp}^l = \frac{n\beta - \beta'}{n\beta + \beta'}$$

$$r_{ss}^l = \frac{\beta - n\beta'}{\beta + n\beta'}$$

$$r_{ps}^l = -r_{sp}^l = \frac{\gamma\beta\kappa_2}{n^2\beta'(n\beta + \beta')(\beta + n\beta')}$$

where $\kappa_2 = in^2Q$ , $\beta = \cos\theta$ ($\theta$ is the angle of incidence measured from the sample normal) and

$$\beta' = \sqrt{1 - (\sin^2\theta / n^2)}$$

## Measurement setup

The magneto-optic response is measured with a SMOKE system (34) sketched in Fig 8 (35). The incident light originates from a He-Ne laser, passes through a rotatable Glan-Thompson polarizer, strikes on the sample surface and it is reflected. The reflected light beam passes through a photo-elastic modulator (PEM), vibrating at a frequency $\omega$ = 50kHz and through a second rotatable Glan

Thompson polarizer, to be finally detected by a pre-amplified photodiode. The components of the detected signal modulated at $\omega$ and 2 $\omega$ are measured with two lock-in amplifiers, whereas the dc component of the signal is measured with a high precision voltmeter. The sample is positioned between the poles of a two-axes ferrite electromagnet in order that the magnetic field H can be applied in the sample surface plane, parallel or perpendicular to the plane of incidence.

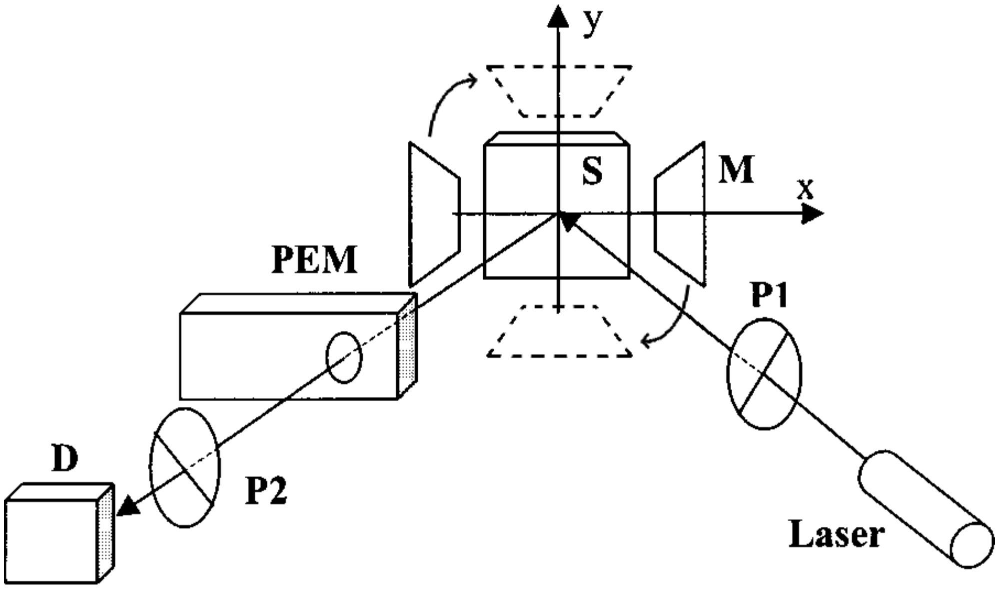

Figure 8: scheme of the Magneto Optical Kerr Effect Magnetometer.

The optical arrangement can be analyzed by using the Jones-matrix formalism (36), where the polarization state of the incident and the reflected electromagnetic waves is expressed by a column vector:

$$\mathbf{E} = \begin{pmatrix} E_p \\ E_s \end{pmatrix}$$

where the symbols p and s indicates the electric field components, normalized to one, parallel (p) and perpendicular (s) to the plane of incidence.

Every optical element can be represented by a 2x2 matrix, expressing the polarization change of the light passing through this element. A sequence of optical elements is expressed as the product of the Jones matrix of each element.

In the measurements presented, the incident light is polarized perpendicular (s) or parallel (p) to the plane of incidence. The matrices describing a polarizer that sets these two polarization state are, respectively:

$$\mathbf{P_s} = \begin{pmatrix} 0 & 0 \\ 0 & 1 \end{pmatrix}, \quad \mathbf{P_p} = \begin{pmatrix} 1 & 0 \\ 0 & 0 \end{pmatrix}$$

The analyser, in contrast, is positioned at a certain angle $\theta_a$ respect to the incidence plane and its matrix results to be:

$$\mathbf{P} = \begin{pmatrix} \cos^2\theta_a & \sin\theta_a\cos\theta_a \\ \sin\theta_a\cos\theta_a & \sin^2\theta_a \end{pmatrix}$$

The sample is described by the Fresnel reflection matrix **R**, showed in a previous equation.

The photo-elastic modulator PEM is used for modulating or varying at a fixed frequency, the polarization of the light beam. The PEM operation principle is based on the photoelastic effect, in which a mechanically stressed sample exhibits birefringence proportional to the resulting strain. Creating an optical axis in the PEM, a linear polarization of light, parallel to the optical axis, has a slightly different speed from that of a linear polarization perpendicular to this axis. Defining $\Delta$ n the difference between the two respectively indices of refraction, it is given that $\Delta n = A\cos\omega_M t$. $A$ is proportional to the amplitude of the voltage applied to the piezoelectric transducer causing the vibration, at the frequency $\omega_M$ in the photoelastic material. The phase angle introduced between two waves travelling through the PEM, with polarization parallel and perpendicular to the optic axis, is $\phi = \frac{2\pi \Delta n l}{\lambda}$, where $l$ is the thickness of the optical element and $\lambda$ is the wavelength of the incident light. The matrix of the photo-elastic modulator can be written as:

$$\mathbf{P} = \begin{pmatrix} 1 & 0 \\ 0 & e^{i\phi} \end{pmatrix}$$

if the optical axis of the PEM is perpendicular to the plane of incidence, thus parallel to the *s* polarization direction. As just explained, the signal measured in the Kerr experiment can be expressed as the product:

$$i_f = \frac{I_f}{I_{dc}} = \frac{\left| \mathbf{A} \cdot \mathbf{P} \cdot \mathbf{R} \cdot \mathbf{E} \right|^2}{I_{dc}}$$

where *f* is the frequency of the measured signal ( $\omega_M$ or 2 $\omega_M$), $I_{dc}$ is the dc intensity and **A**, **P**, **R**, **E** are the Jones matrices described above. Supposing that the incident light is polarized *s*, from previous equation, neglecting terms of second order in the magnetization, it is for the normalized lock-in output at $\omega$ and 2 $\omega$:

$$i_{\omega}^{s} = C_1 f\left(\theta_a\right) \Phi\left\{ r_{ss} r_{ps}^{*} \right\} , \quad i_{2\omega}^{s} = C_2 f\left(\theta_a\right) \mathrm{E}\left\{ r_{ss} r_{ps}^{*} \right\} \quad \text{eq 1}$$

where $f\left(\theta_a\right) = \sin\theta_a / \cos\theta_a$, $C_1 = -4J_1 / \sqrt{2}\left|r_{ss}\right|^2$ and $C_2 = 4J_2 / \sqrt{2}\left|r_{ss}\right|^2$.

$J_1 = 0.519$ and $J_2 = 0.432$ are, respectively, the first and the second order Bessel function evaluated at $\phi = 137.8^{\circ}$ (37). In fact, the term $\phi$ in the Jones matrix of the PEM is proportional to $\cos\omega_M t$. If $e^{i\phi}$ is expanded in a series of Bessel polynomials:

$$e^{i\phi} = e^{i\frac{2\pi A l}{\lambda}\cos\omega t} = J_0\left(\phi_M\right) + 2iJ_1\left(\phi_M\right)\sin\omega t + 2J_2\left(\phi_M\right)\cos 2\omega t + \ldots \quad \text{eq 2}$$

If $\phi_M = \frac{2\pi Al}{\lambda}$ is set at 137.8 degrees, $J_0$ results to be equal to zero and the first and second order Bessel functions have the values cited above. The other higher order terms of equation 2 are negligible not because are small, but because the lock-in detections are limited to measuring signals at $\omega_M$ and $2\omega_M$ frequencies.

Considering Eq. 1 and the relations between Kerr rotation $\vartheta_K$ and Kerr ellipticity $\varepsilon_K$, it is simple to show that the former term $i^s_\omega$ is proportional to Kerr ellipticity, whereas the latter term $i^s_{2\omega}$ is proportional to Kerr rotation.

It is interesting to remark the relation that connects the measured signal with the magnetization components, through the Fresnel reflection coefficients

$$\Phi\left\{r_{ss}r^*_{ps}\right\} = \Phi\left\{g^s_1(nQ\theta)\right\}m_x - \Phi\left\{g^s_2(nQ\theta)\right\}m_z$$

where $g^s_i$ are functions of the complex refraction index n, of the Voigt magnetooptical constant $Q$ and of the incidence angle $\theta$.

A similar relation is obtained if the incident light is polarized parallel to the incidence plane (p-polarization), so that, with opportune arrangement and approximations, the measurement of the single magnetization components is possible. To study the interaction effects between nanomagnetic structures is sufficient to obtain the rotation and ellipticity quantities that contain the magnetization, though they are not simply proportional to it (4).

## Vibrating Sample Magnetometer (VSM)

The VSM is the most simple magnetometer and is based on measuring the change of the magnetic flux when a sample is vibrating inside a changing magnetic field.

The sample, commonly a small disk, is attached to the end of a nonmagnetic rod, the other end of which is fixed to a loudspeaker cone (Fig. 10) (5) or to some other kind of mechanical vibrator. The oscillating magnetic field of the moving sample induces an alternating voltage in the detection coils, whose magnitude is proportional to the magnetic moment of the sample. The voltage induced is amplified with a lock-in amplifier which is sensitive only to signals at the vibration frequency. The lock-in amplifier must be provided with a reference signal at the frequency of vibration. The detection-coil arrangement shown in Fig. 10 is only one of those described by Foner (38).

The coil arrangement of Fig. 10 is very commonly used. The apparatus is calibrated with a specimen of known magnetic moment, which must be of the same size and shape as the sample to be measured, and should also be of similar permeability.

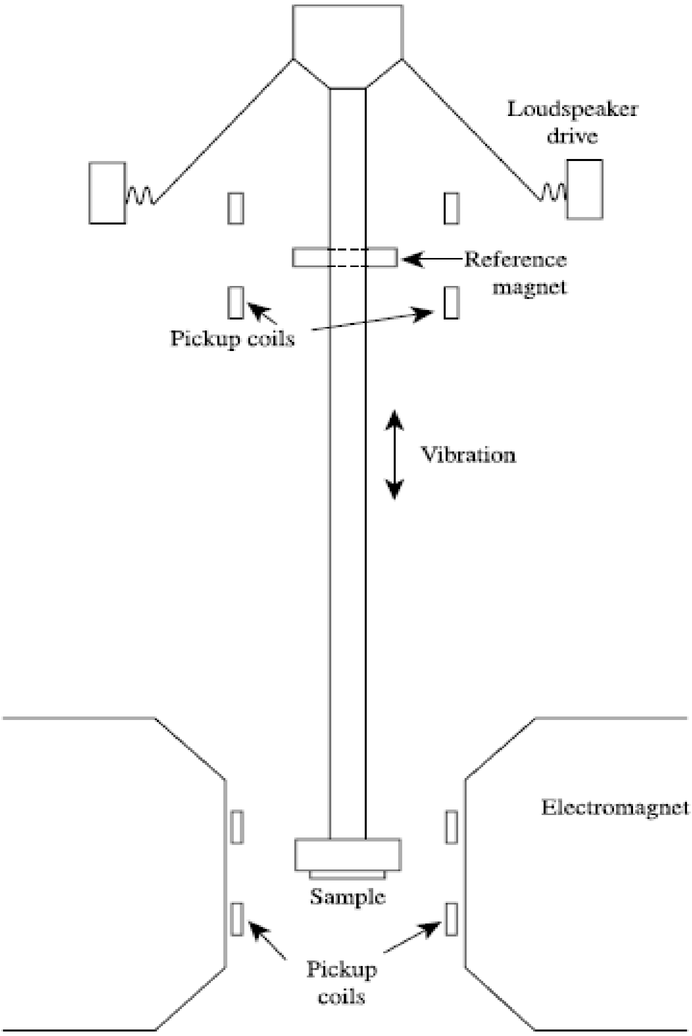

Figure 10: Vibrating Sample Magnetometer scheme.

## The Brillouin light scattering

The Brillouin light scattering is referred to the inelastic light scattering from thermally excited spin waves and offers the possibility to determine the dynamical magnetic excitations in thin film as well as in ordered nanostructures as nanodot arrays.

It is well known that collective excitations in a solid can inelasticly scatter incident light, through the induced modulation of the optical constants of the medium. In analogy with the elasto-optic effect caused by acoustic phonons, in the case of spin waves this is achieved via the magneto-optic interaction. This can be understood as the fluctuation of the transverse polarizability of a medium due to the Lorentz force caused by the fluctuating magnetization (39).

In a BLS experiment, a beam of highly monochromatic light is focused on the surface of the sample and the light scattered within a solid angle is analysed in frequency using a multi-pass Fabry-Perot interferometer. This last one is required in order to extract and separate the weak inelastic component of light from the elastically scattered contribution (40). If the process is viewed as a two-particles diffusion, a photon and a magnon (the energy quantum of spinwaves), the conservation of the wave vector brings that the wavelength of the revealed spin waves is of the same order of magnitude as the light magnitude, i.e. much larger than the interatomic distances. Therefore the medium can be considered as a continuum.

The BLS measurements offer also the way to determine different magnetic parameters as the saturation magnetization, monitoring the spin wave frequencies as a function of the direction and magnitude of the in-plane wave vector of the incident light and of the direction and strength of the applied magnetic field. Figure 9 (39) shows the setup of the BLS experiment in the backscattering configuration, which is usually exploited in studies of thin films or layered structures.

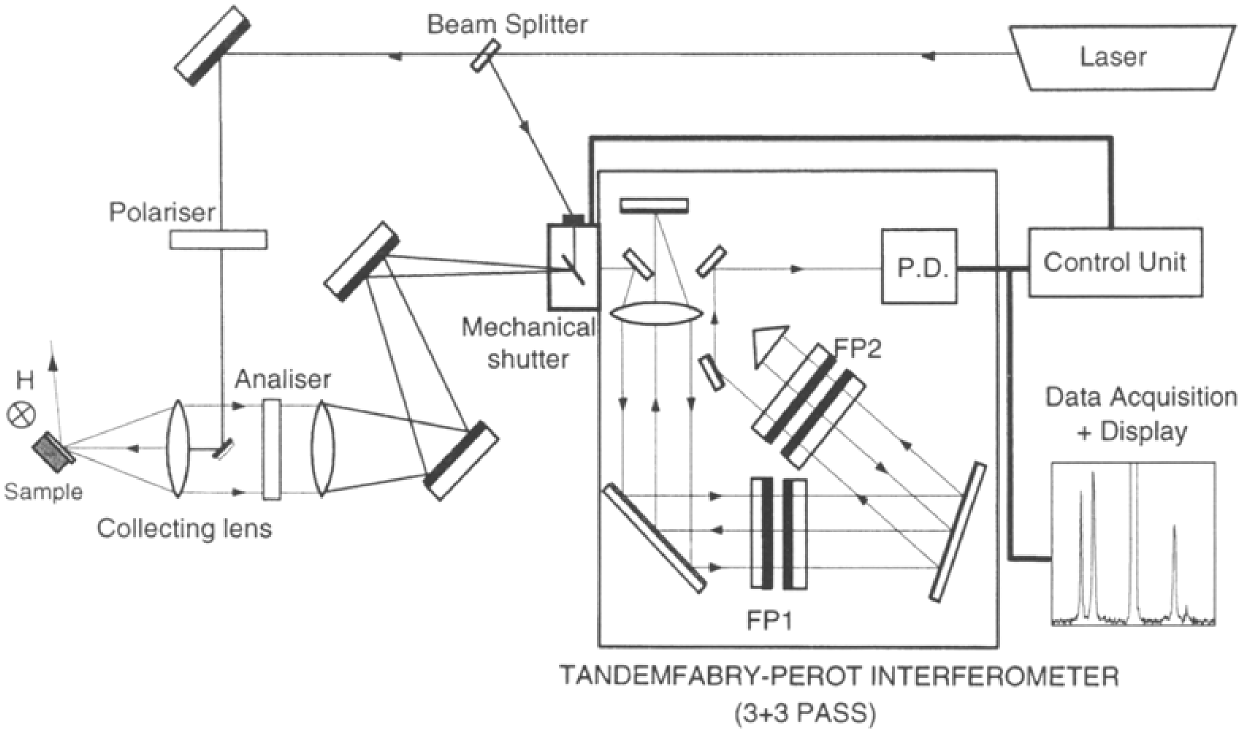

Figure 9: scheme of the Brillouin Light Scattering apparatus.

In this geometry, the spin-wave vector component parallel to the sample surface $q_{\parallel}$ is related to the optical wave vector $k_i$ by the following simple equation:

$$q_{\parallel} \quad 2k_i \sin\theta_i$$

where $\theta_i$ is the angle of incidence of light. The energy conservation guarantees that if $\hbar$ is the energy of the incident photon and $\hbar$ is the energy of the magnon then the energy of the backscattered photon will be $\hbar$ according to the magnon absorption (right shift or anti-Stokes) or creation (Stokes) in the process, respectively.

# Thin Films with Perpendicular Magnetic Anisotropy: stripe domains and “Rotatable anisotropy”

# Iron-Gallium

## Introduction

Galfenol is an Iron and Gallium magnetostrictive alloy (FeGa) with well known properties and is employed in the fabrication of various sensors and actuators that make use of the particular property of magnetostriction (for example sonars: the acoustic deformation is transformed in an electromagnetic signal).

The study of FeGa properties in thin film form is important due to the fact that it can be integrated in spintronic nanodevices: in particular the studied system is produced (as we will see in detail in the next paragraphs) on a ZnSe/GaAS substrate; the Zn-terminated ZnSe epilayer is a prototype of the low reactive iron/semiconductor interface (41), it is expected to constitute large tunnel magnetoresistance devices and is the best choice (42) for the injection of spin polarized current in the GaAs semiconductor for the realization of hybrid electronic/spintronic devices. Moreover the magnetostrictive behavior of the FeGa thin film gives the possibility to change the surface magnetic features acting, for example, on the Ga concentration or on the film thickness.

An interesting property that we have found (43) in the FeGa thin films is the creation of stripe domains, that are originated by the presence of a Perpendicular Magnetic Anisotropy (in turn rising from the short-range ordering of Ga pairs along the [001]-growth direction) (44). In these samples we have observed the “Rotatable Anisotropy” which makes possible to rotate the stripes direction and the direction of preferential magnetization (easy direction).

In this study we aim to deepen our knowledge of the magnetic properties of the FeGa thin films as deposited, in particular of the Rotatable Anisotropy giving an interpretation that couples together its dynamical and static definitions (up to now, only a definition based on dynamical properties is available (45) (46)).

We also would evidence rotation and reversal of the stripe domains by the in-field MFM measurements, giving the details of the mechanism and showing what subtend to their evolution. Finally we will show that it is possible to change the magnetic ordering by the application of a strong OOP magnetic field and this bring to the creation of an alternative stable configuration of the surface magnetization that is called “mixed bubble pattern” (21).

## FeGa film production and characteristics

The $Fe_{1-x}Ga_x$ films were produced at the University Pierre et Marie Curie in Paris by co-evaporation from independent Fe and Ga Knudsen cell sources on a substrate of ZnSe/AsGa(001) of a Molecular Beam Epitaxy chamber as explained elsewhere (by M. Eddrief et al.) The composition of the alloys was determined by X-Ray Photoelectron Spectroscopy while the thickness of the samples was investigated by means of X-Ray Reflectivity. The first sample studied in the present thesis has Ga concentration and thickness respectively of $x=0.20$ and $t=65$ nm.

The choice to produce a sample with these composition is due to the fact (43) that $Fe_{1-x}Ga_x$ thin films with $0.15<x<0.30$ represent the transition between Fe-like and FeGa-Bulk behavior. One notices that the biaxial iron magnetic anisotropy favoring the (001) axis is lost when $x = 15\%$ and magnetic hysteresis measured along different axes nearly overlap, indicating a Ga-induced quenching of the biaxial magnetic anisotropy. Recent crystallographic studies (44) show that the Ga pairs have a preferential direction along the [001]-growth direction in this kind of thin films and the deformation of the pristine cells along that direction is responsible for this magnetic behavior.

## Magnetic Characterization

The longitudinal hysteresis loop, measured both by MOKE and a vibrating sample magnetometer (VSM), is reported in Figure 1. When the magnetic field was reduced from positive saturation, we observed a linear region of M vs. H, starting around H ≈ 1500 Oe, typical of materials with sizable Perpendicular Magnetic Anisotropy (PMA), that is a condition for the existence and formation of the so called: “stripe domains”. This is possible only if the thickness of the thin film is greater than a critical value. In fact, the existence of stripe domains is proved by MFM measurements as it can be seen in the image below (Figure 1). The image is obtained applying a saturating in-plane field (up to 3 kOe) along the crystallographic direction [110], then reducing the field to remanence. The period of the stripes is obtained by means of the Fourier analysis and is about 90 nm.

The PMA takes place in presence of a positive (negative) magnetostriction constant combined with a planar compressive (tensile) stress. This is the case of the FeGa thin film (43), where a competition between the out of plane energy density $K_n$ and the dipolar one $2\pi M_s^2$ (where $M_s$ represents the saturation magnetization) occurs. The Out Of Plane (OOP) energy would favor the rise of an OOP component of magnetization, while the shape factor would prefer the magnetization all in the plane of the thin film. It is then possible to define the Quality Factor $Q = K_n/2\pi M_s^2$ and, provided that the thickness value is above the critical one, when $Q \leq 1$ stripe domains formation may take place.

In-field and Out-of-field MFM measurements have been performed to understand how the stripe domains behave under the application of an external field. The first measurement was performed to understand whether an 800 Oe in plane field annihilates or at least reduces the intensity of the detected OOP stray field (considering that the MOKE loop displayed that only above 1500 Oe the complete in-plane saturation of the film can be obtained). Then a 800 Oe field is applied along the in plane [110] direction and the MFM image is obtained (see Figure 2). No particular differences in the stripes appearance come out from the field application, nor if a detailed analysis of the OOP profile of magnetization and stripe period (that remains about 90 nm) is performed.

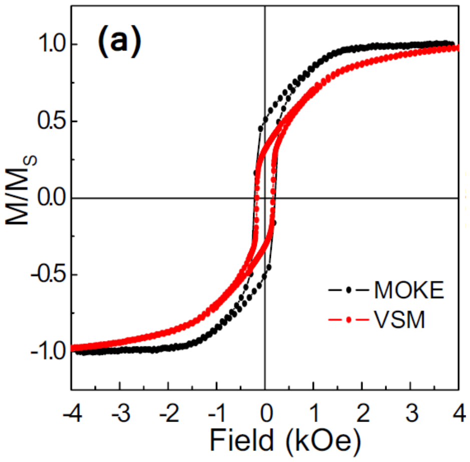

Figure 1: hysteresis loops obtained with MOKE and VSM respectively they give information in the surface and on bulk magnetization behavior.

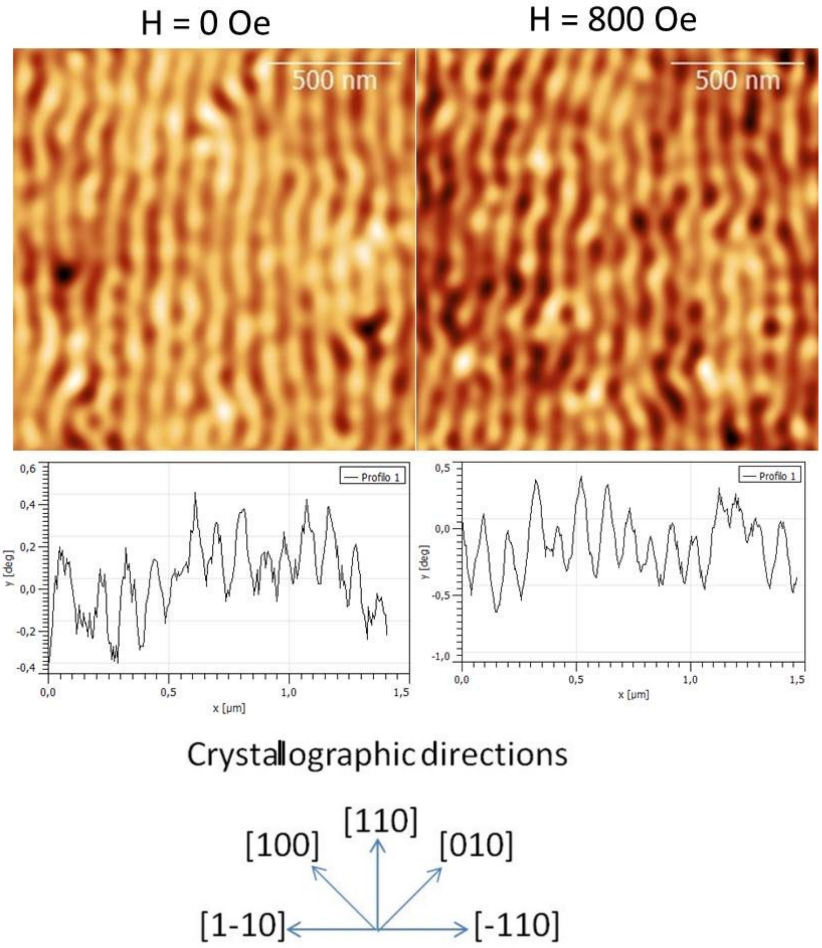

Figure 2: MFM images at remanence and in-field with the magnetization profile in the transverse direction.

Another experiment was the application of an increasing external field along the [1-10] in plane direction (perpendicular to the [110] one) when the stripes are along the [110] direction. The field was increased to 100 Oe along that direction, then was reduced to remanence and the MFM measurement was performed. Then the field was increased to 200 Oe, reduced to remanence and the MFM image was produced. We continued in this way with steps of 100 Oe until reaching the maximum external field value of 800 Oe. The sequence of MFM images so obtained is shown in the image 3. One sees that up to 300 Oe nothing changes, the stripes are still in the [110] direction. When 400 Oe are reached one can notice that the stripes lie no more along the [110] direction but a coherent rotation process has started. While the field is growing one observes that the rotation angle of the stripe domains increases proportionally with the applied field and the rotation along the field direction is completed at 800 Oe. Once the rotation is completed the stripe domains remain permanently in that direction. We performed the opposite rotation (from [1-10] to [110] direction) by the application of an increasing field along the [110] and we saw that it is substantially identical and requires the same field to be completed (we don't report the images sequence here). Factually the direction along which the stripes are induced "runs" as a direction of Easy Magnetization and any in plane direction would become an Easy one. This is the reason why we speak of "Rotatable Anisotropy" or "Pseudo-Uniaxial Anisotropy".

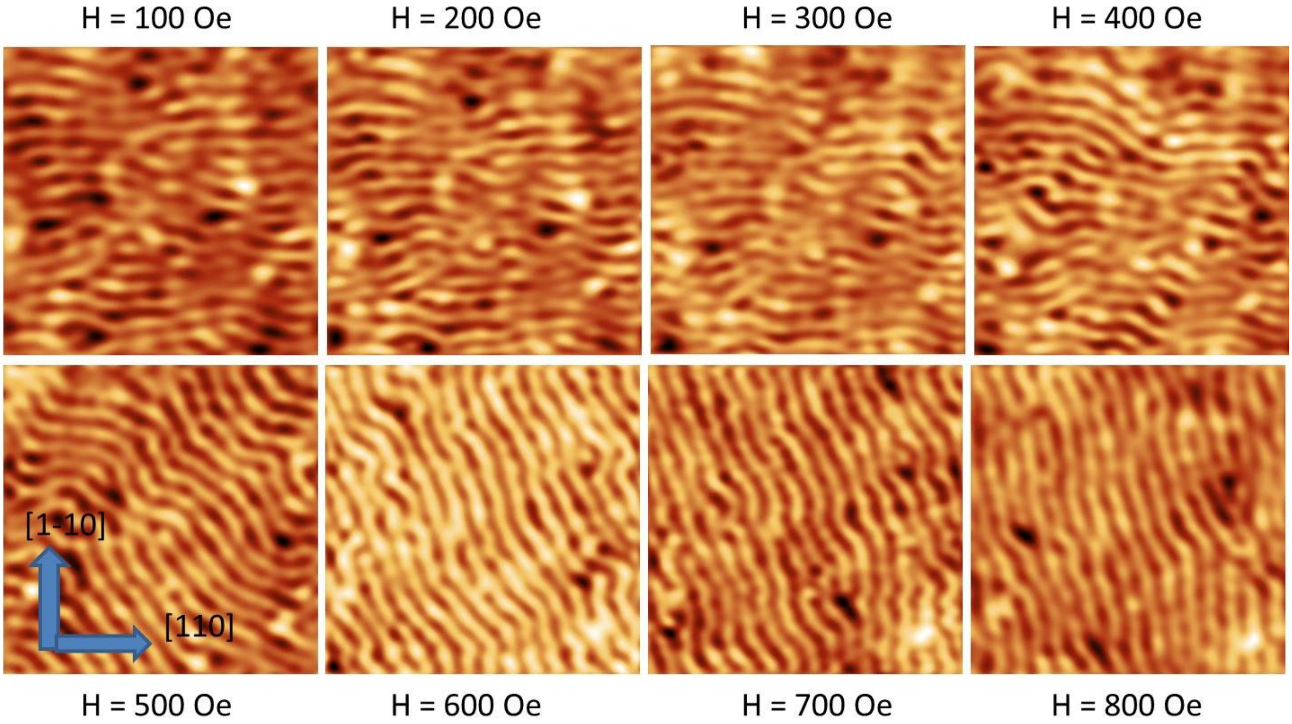

Figure 3: MFM images of the rotation of stripes due to the application of an increasing in-plane field in the direction trasverse to the stripes.

The concept of Rotatable Anisotropy was introduced decades ago in the study of magnetostrictive Ni, Fe, and NiFe films (47) (48) with perpendicular magnetic anisotropy (PMA) because an unexpected isotropic shift was observed in the ferromagnetic resonance (FMR) field (49) (50), or in the Brillouin light scattering (BLS) frequency of spin waves (51). In order to explain such experimental evidence in the framework of a model with a uniform in plane magnetization, it was necessary to invoke a rotatable anisotropy field $H_{rot}$.

## Rotatable Anisotropy in FeGa thin films

“Anisotropy” is a term that simply means that the magnetic properties depend on the direction in which they are measured; in particular in a magnetic crystal one can distinguish one or more directions of Easy Magnetization from other that are Medium or Hard directions. In the traditional concept of Magnetic Anisotropy (as it is for Crystallographic Anisotropy or Shape Anisotropy) it is straightforward to differentiate an easy from an hard direction simply comparing the hysteresis curves: the direction in which the saturation magnetization is reached with the smallest external field is the Easy Direction and the Hard one is the direction in which a greater external field is needed to saturate the sample. The concept of Rotatable Anisotropy comes (as said before) from the fact that in some magnetostrictive magnetic materials a shift was observed in the ferromagnetic resonance (FMR) field, or in the Brillouin Light Scattering (BLS) frequency of spin waves along a particular direction as it was the easy direction: however after the application of a great enough external field along another direction, this last became the new easy direction, showing the same shift of FMR field or spin wave frequency and transforming the previous direction in an hard one.

For its modifiability under external field it results that the rotatable anisotropy field associated with the stripe domain pattern cannot be measured by means of conventional magnetometry techniques (e.g., longitudinal MOKE or VSM hysteresis loop): the measurement of a loop along an hard direction perpendicular to the stripes rotates the stripes themselves and makes it an easy direction. Rather, one can use any (quasistatic or dynamic) experimental technique capable of exerting a nonzero torque on the film magnetization.

A peculiarity of the BLS technique is that the finite in-plane transferred wave vector determines the spin-wave propagation direction with respect to the stripes axis even in the absence of a dc bias field. An ac sensing field is not required either, because BLS probes the spontaneous, thermally excited transversal fluctuations of the magnetization.

BLS measurements were performed (at the Department of Physics at Perugia University) in backscattering geometry focusing about 200 mW of monochromatic light (532 nm wavelength) onto the sample surface. The backscattered light was analyzed by a Sandercock-type (3 + 3)-pass Fabry-Perot interferometer (39). The incidence angle of light was 15◦, corresponding to an in-plane transferred wave vector $q = 0.61 \times 10^5$ $cm^{-1}$. In a first set of measurements, the sample was initially saturated applying a strong magnetic field (H = 3 kOe) along the [110] axis, and then removing it, in order to obtain a stripe structure along that direction. BLS measurements were performed at remanence rotating the sample around the film normal, i.e., varying the angle $\phi q$ between the in-plane transferred wave vector q and the [110] axis (view the inset of Figure 4). The measured frequencies, together with two typical spectra, are reported in Figure 4. We observed two modes having a constant frequency (green and blue solid points), which correspond to perpendicular standing spin-wave modes (nPSSW) characterized by n nodes of the magnetization oscillation through the film thickness. In addition, we observed a spin-wave mode (red points), whose frequency is characterized by a 180◦ symmetry. Since micromagnetic simulations (further described) and MOKE measurements indicated that at remanence there is a noticeable component of the in-plane magnetization directed along the stripes axis, we interpret the above oscillating frequency mode as a dipolar-dominated magnetostatic mode (MW), having the maximum spin precession amplitude in the surface region where the magnetization is directed in plane, parallel to the stripes axis. When ϕq = 90◦ (ϕq = 0◦), the MW mode propagates with q perpendicular (parallel) to the component of the magnetization directed along the stripes axis, i.e., in the magnetostatic surface wave (MSSW) [backward volume magnetostatic spin wave (BVMSW)] configuration. As expected for a mode mainly localized in the surface region (39), the MW mode exhibits a marked Stokes/anti-Stokes asymmetry (top of Figure 4), which can be reversed by simply reversing the direction of the magnetic field used to prepare the stripe structure. When the stripes are prepared along other directions, the frequency of the nPSSW modes remains angle independent, while the MW frequency is rigidly shifted; in Fig.4 one can see that when the stripes are prepared along the [010] direction (open points), the MW mode has a maximum along the [100] direction (ϕq = 45), where q is perpendicular to the stripes. This proves the rotatable and pseudouniaxial character of the observed anisotropy.

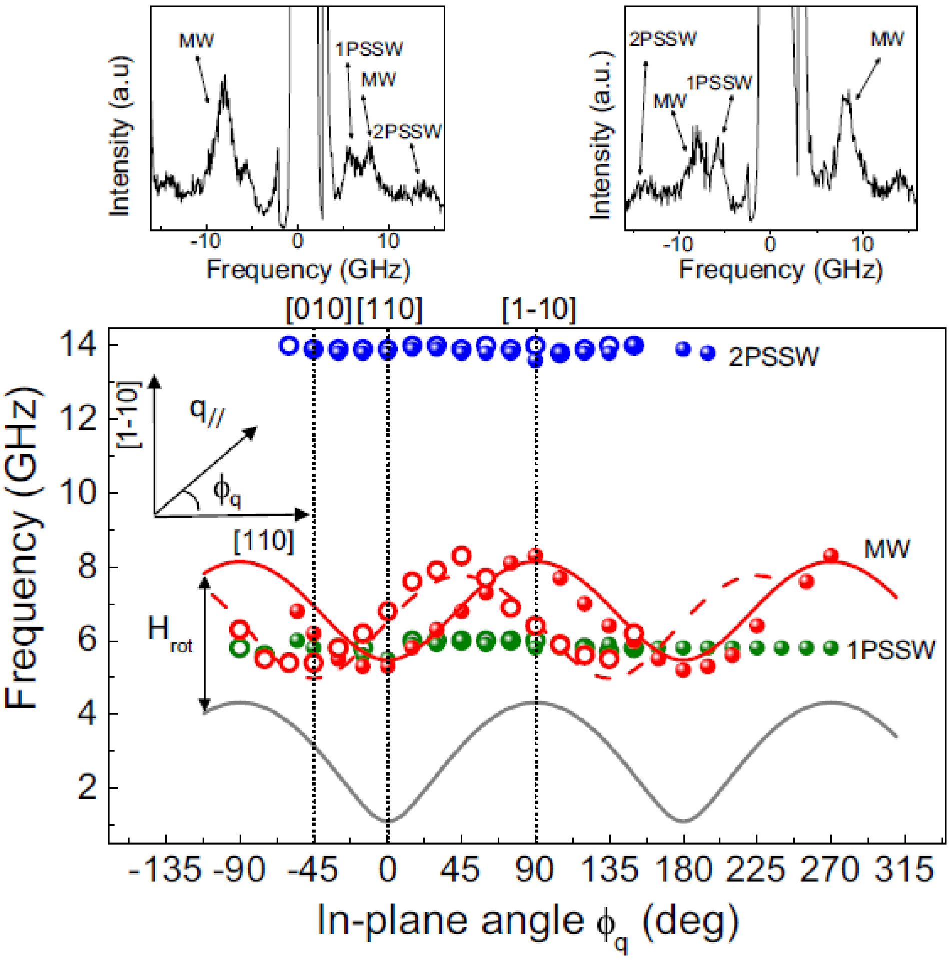

Figure 4: spin wave modes variation under the rotation of the sample in plane. The red dot are the measured, the red lines are those calculated. The grey line represents the calculated modes without the anisotropy field.

## Micromagnetic Simulations

A simulation with the LLG micromagnetic package was conducted to find the configuration of magnetization in the internal stripes structure. For the purpose it was used a magnetization saturation value $4\pi Ms$ = 17580 Oe (derived from VSM measurement); the exchange constant $A_{ex}$= 1.6 $\times$ $10^{-6}$ ergs/cm, the out-of-plane anisotropy constant $K_n$ = 4.2 $\times$ $10^{6}$ ergs/cm$^3$, and the tetragonal anisotropy $K_1 = -0.8 \times 10^5$ ergs/ cm$^3$, favoring the [110] and [1-10] directions were obtained by the fit of BLS and FMR measurements in a high magnetic field, when the magnetization is saturated in plane (not shown here).

The figure 5 shows the calculated hysteresis loops for the bulk and for the upper 10 nm of the film. The remanent magnetization for the Bulk is lower than the Mr for the surface in qualitative agreement with the measured data (VSM probes the bulk while the MOKE interacts with the surface magnetization). The image 6 is a sketch of the spatial distribution of the remanent magnetization as calculated with simulation. In the bulk the magnetization vector rotates around the longitudinal stripes direction alternately clockwise and counterclockwise, so that the separation plane between adjacent domains is alternately upward and downward. In the surface region the magnetization vectors tend to stay in the plane of the surface with a net component along the stripe axis.

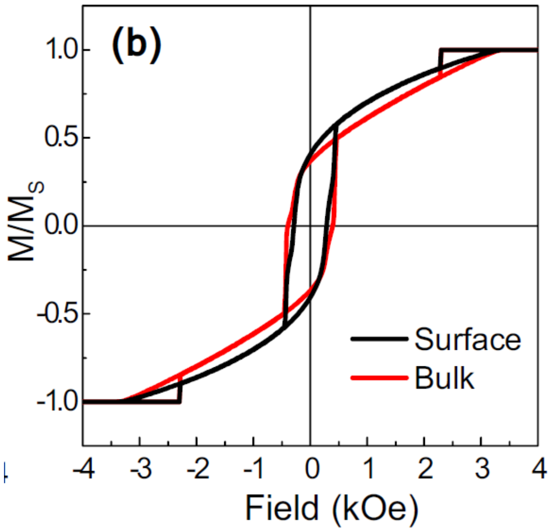

Figure 5: calculated hysteresis loops for surface and bulk magnetization

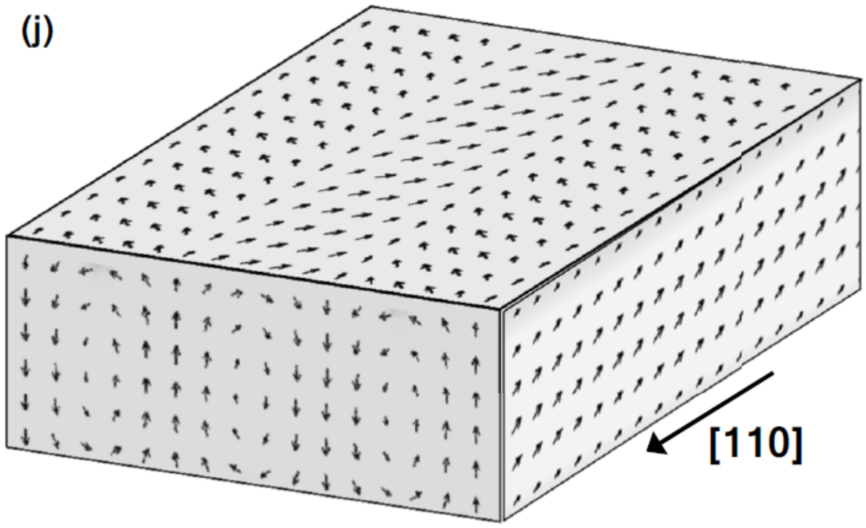

Figure 6: magnetization distribution at remanence calculated with LLG micromagnetic simulator

To easily establish a relationship between BLS and MFM measurements, we exploited an approximate analytic expression (39) that allows the calculation of spin-wave frequency as functions of different variables (including the angle between the field and the stripes direction and the applied fields) valid for thin films with a uniform in-plane magnetization.

$$\left(\frac{\omega_{MW}}{\gamma}\right)^2 = \left[H_{rot} - \frac{K_1}{M_s}\cos^2 2\phi + 4\pi M_s D\left(1-\frac{q_\parallel}{2}\right) \quad 2\frac{K_n}{M_s} + \frac{2A_{ex}}{M_s}q_\parallel^2\right] \times \left[H_{rot} - \frac{K_1}{M_s}\cos^2 4\phi + 4\pi M_s D q_\parallel \quad \frac{K_n}{M_s} \quad \frac{2A_{ex}}{M_s} q_\parallel^2\right] \tag{1.1}$$

Here ϕ (ϕq ) is the angle formed by the in-plane magnetization (the transferred in-plane wave vector q) with the [110] direction, and D is the demagnetizing factor. Owing to the presence of stripes, $H_{rot}$ and D are phenomenologically introduced as fit parameters (52). Using the same parameters of the micromagnetic simulation, we obtain Hrot = 1350 Oe, nearly ten times larger than H1 = $2K_1/M_s$ = 114 Oe (the effective field associated with in-plane anisotropy), and D = 0.51, almost equal to the ratio $M_r/M_s$ measured by MOKE. This substantiates the surface character of the MW mode. Note that $H_{rot} > 0$ is crucial to get a good fit of the MWfrequency: The calculated (red) curve of Fig. would be downshifted (gray curve) by more than 3 GHz in the absence of $H_{rot}$, resulting in a relevant disagreement with the experimental data.

Finally it was calculated the $H_{rot}$ dependence on the value of the applied field. In the approximation formula above, The measured frequencies (red point) were introduced as function of the applied fields, using $D = M(H)/M_s$ derived from MOKE measurements as values for demagnetizing factor $H_{rot}$ vs external field H was determined (see fig 7). $H_{rot}$ presents a linear decrease and reduces to zero in correspondence of a field at which the sample is saturated in plane.

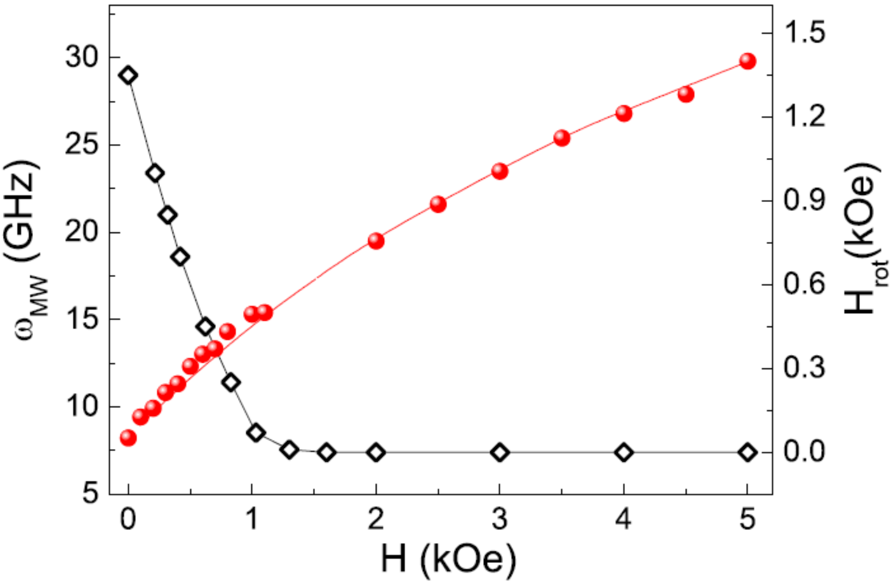

Figure 7: frequency of the spin-wave mode related to the rotatable anisotropy under an external field (red line); calculate anisotropy field value as function of an incresing external field.

## Comparison between BLS and MFM

Since in BLS it is possible to distinguish a MW mode whose frequency is strictly correlated with the angle between the transferred in-plane wave vector and the stripes direction we measured the MW frequency shift in a stripes rotation experiment following the same procedure performed in the MFM measurements.

The stripes were prepared along the [110] direction by applying a 3 kOe external field and the sample was rotated 90 degrees in plane. A 100 Oe field was applied along the [1-10] direction and shutted off while the MW mode frequency was detected. Next the external field was led to 200 Oe, turned off and the MW frequency was measured and so on until an 800 Oe field was reached. In an analogous MFM experiment we saw that the stripes started rotating at about 400 Oe and the angle of rotation increased as the applied field increased. In the image 8 we reported in the graphic below the measured frequencies (red dot) vs the applied field and in the upper graphic the calculated angles of stripe rotation $\phi$ (by mean of the approximation formula 1.1) and compared with the measured angles of stripes rotation (derived from MFM images). There is a good agreement between the calculated and measured angles, proving the goodness of our model.

the MFM.

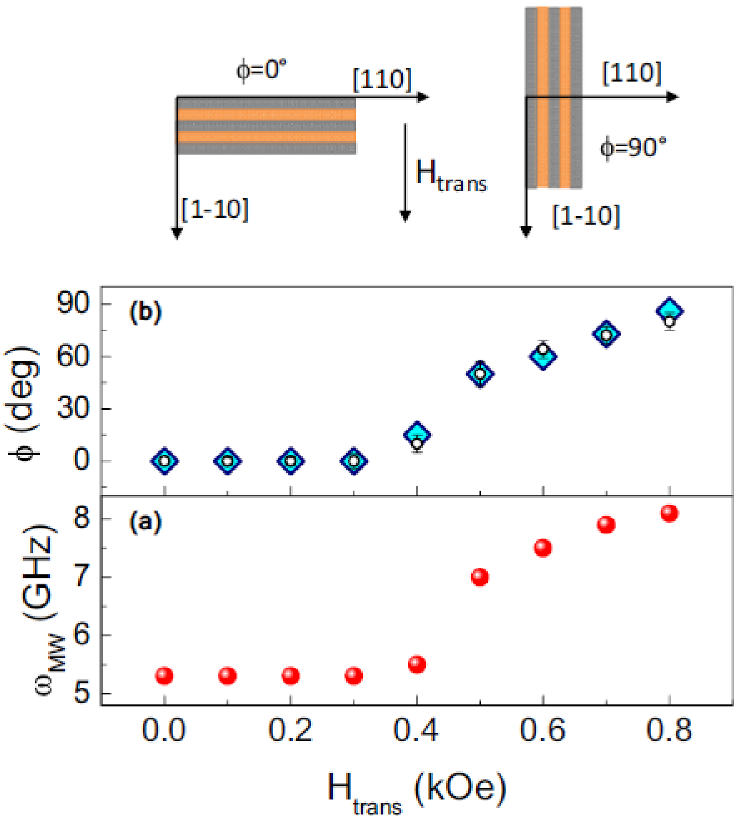

Figure 8: comparison between measured and calculated rotation angle of the stripes.

## Rotation and Reversal Processes

As could be inferred from the MOKE measurements this sample has a coercive field of about 200 Oe, field at which the magnetization changes sign and abruptly increases until it reaches the 65% of the saturation magnetization within a few tens of Oersted. One can argue that it happens between 200 and 300 Oe. Over this field value the linear M vs H behavior starts and the field “works” to smooth the magnetization along the plane of the thin film. In order to understand what happens in the stripes domains when the magnetization is inverted we observed the process with the MFM.

We simply saturate the sample along the [110] direction with a -800 Oe negative field, we performed the MFM in field measurement, then we inverted the field to +800 Oe and observed the stripes at this field. In order to establish if the stripes moved from their position we found the following method to create a precise reference: in the image below (fig 9) we reported (for the same measurement) both the MFM signal and the AFM topography. Imperfections on the topography generally are considered a bother in the MFM technique but, in this measurement, were a help for the creation of a map of the analyzed surface. In fact we put a marker on 5 precise defects and, superimposing on it the MFM image, we transferred the marker position on the stripes. This is done also for the successive MFM image: in this way, if the stripes are not in the precise position with respect to the markers, it is because the stripes moved from their previous position.

In these measurements we circled two markers (red crosses) that we considered the most representative. In the left image (violet circles) the cross in the left is positioned on the center of a white (upward magnetized) stripe. In the right image the same cross instead is positioned precisely in the center of a black (downward magnetized) stripe. In the left image the right circled cross is positioned at the edge of the black/white signal that is between two stripes (the black is on the right the white on the left of the cross). In the right image, the same cross instead is yet in between two stripes but this time the black is on the left and the white on the right. In both the previous two cases, the in-plane magnetization sign inversion produced a complete inversion of the out-of-plane component of magnetization along the transverse direction of the stripes and applied field. Considering this component as a wave, there was a shift of 180 degrees (half wave length) of the magnetization.

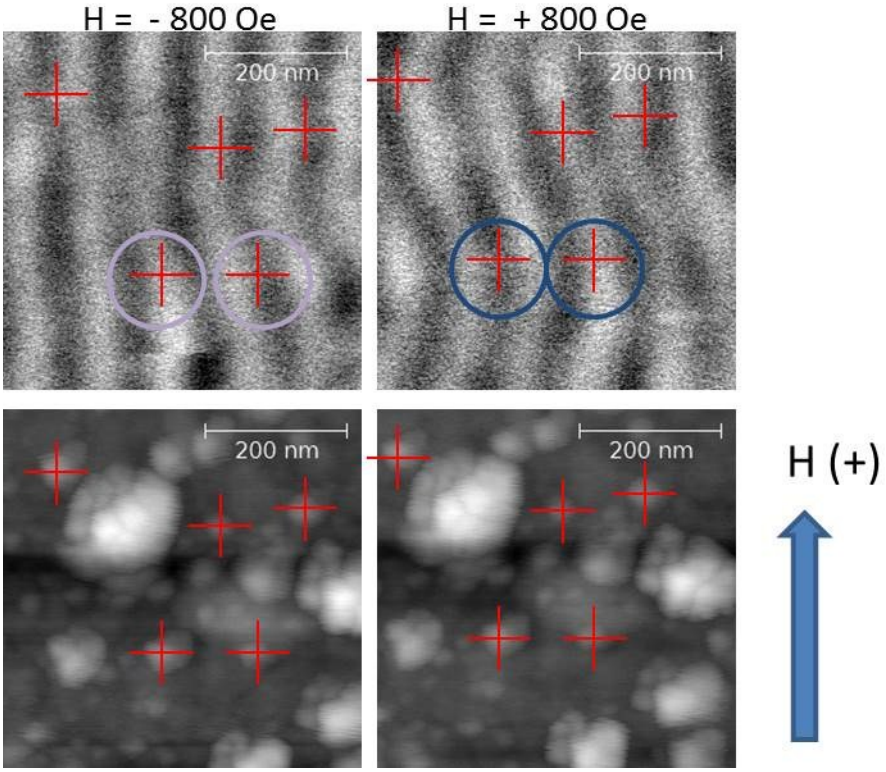

Figure 9: comparison between topography and magnetic information allows to determine the shif of the stripes after the reversal.

For the other three crosses the situation is not so clear because the complete saturation is not achieved and probably the applied field is not sufficient to complete the process of shift of the OOP component of magnetization along the direction transverse to the stripes axis. An indication of this could be found looking at the position of upper portion of the stripes with respect to the case previous the field application: the stripes are bent because only the bottom section has accomplished the transition.

Then we repeated the experiment with closer field steps. After the saturation (and then stripes induction) with a -6000 Oe field in the [110] direction we reduce the field to remanence and then start to increase it to positive value as one can see in the image below (fig 10).

We concentrate on the light-blue marker and the light-blue arrows indicating two “bifurcations”. At +35 Oe field the blue marker encircles a cross on a right border of a white stripe (left border of a black one) while at the upper right of the MFM image there are two bifurcations (two stripes come together to become one indicated with numbers 1 and 2). At 212 Oe the right bifurcation 2 disappears and a new bifurcation (3) is created below it. At 255 Oe also the left bifurcation (1) disappears but leaves place to another (4) at its left : the bifurcation has moved to left in a process that we can call propagation of a dislocation. The propagation of the bifurcation leads to the 180 degrees transversal shift of the stripes before noticed. Finally, the green circles indicate two more crosses showing where inversion leads to the 180 degrees shift of the OOP transverse magnetization; notice that the process is completed at 294 Oe in the field range in which the magnetization changes sign. This is the process by which the stripe domains pattern performs the reversal of in plane magnetization.

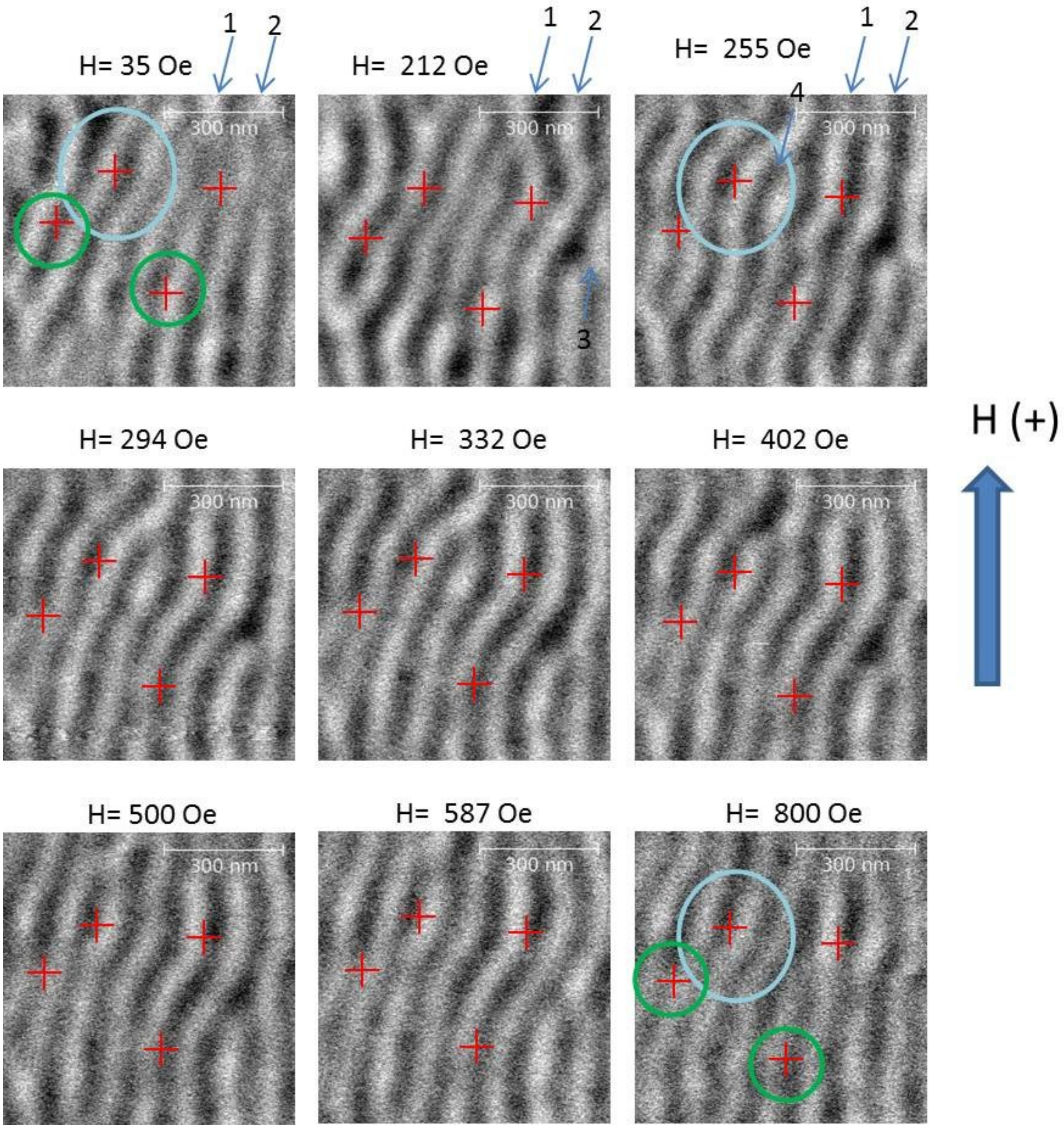

Figure 10: stripes reversal analysis

This analysis performed in the case of the rotation of the stripes suggests that the process is the same. We can conjecture that the rotation process happens with a breaking and propagation of defect points (bifurcations) and terminates with recombination under a different angle. In a series of steps breaking-dislocation-recomposition the rotation goes ahead until the process is completed. While the in plane sign change of M and the 180 degrees shift of the stripes starts at

200-300 Oe external field, the rotation process needs more energy: the stripes in facts start rotating at about 400 Oe and complete the rotation at about 800 Oe. In support to this hypothesis (of the stripes rotation mechanism) we show a rotation of stripes of a 135 degrees angle (fig. 11). After induction of the stripes along the [-110] direction with a +800 Oe field the sample was rotated in plane of 135 degrees. Then an increasing external field was applied along the [100] direction. One can see no coherent rotation, as in the case of the 90 degrees rotation, but unexpectedly above the 400 Oe the stripes break in a lot of segments randomly oriented (but preferentially along the starting direction and the normal direction). This is a clear proof of how the stripe domains don’t rotate on their entire length; instead they break in correspondence of defect point and recompose to form new stripes with different orientation and length.

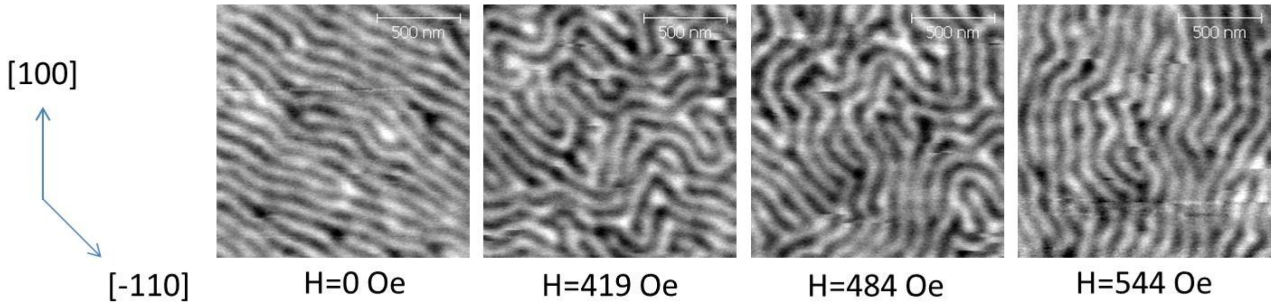

H=0 Oe H=419 Oe H=484 Oe H=544 Oe

Figure 11: rotation of stripes about 145 degrees produces labyrinth domains.

We would like to remember that the stripe domains are not domains with a crystallographic origin, and that their formation is due to the balance between different type of magnetic energy contribution; this is the reason why it is possible to break and recompose them only with the field application.

As a consequence, in some particular conditions (that we now are going to describe), it is possible in the same kind of sample, to produce a particular type of domains, called Bubble Domains.

## Bubble Domains Formation

The experiment consists of applying a strong magnetic field perfectly perpendicular to the plane of the thin film. The images below (figures 12 and 13) were obtained by applying a 1.6 Tesla field along the Out Of Plane direction. The resulting domain pattern is the so called “Mixed Bubble Pattern” (21) that is, as the locution says, a tangle of stripe-like domains and Bubble domains.

Bubble domains are defined as isolated uniformly magnetized domains having a cylindrical shape in which the magnetization vector inside points in a direction opposite to the magnetization vector outside the bubble. The existence of stable bubble domains is governed by the presence of a perpendicular magnetic anisotropy along the cylinder axis (in this case in the OOP direction) and generally it is possible (53) to obtain transient single bubble domains by the application of a Bias field orthogonal to the bubble axis starting from a state of mixed bubble/labyrinth domains (equilibrium state).

In our case we observed the formation of the mixed state (bubbles and labyrinth or stripe domains) by the application of a strong OOP field, so it is logical conjecturing that we increased the anisotropy along the OOP direction. This is a noticeable point: we already demonstrated that the Rotatable in-plane Anisotropy determines the rotation of the stripes and the frequency shift of spin-waves associated to a Rotatable anisotropy Field but, with this experiment we show that we can increase the perpendicular magnetic anisotropy (and then the quality factor $Q= K_n/2\pi M_s^2$) producing a new meta-stable state.

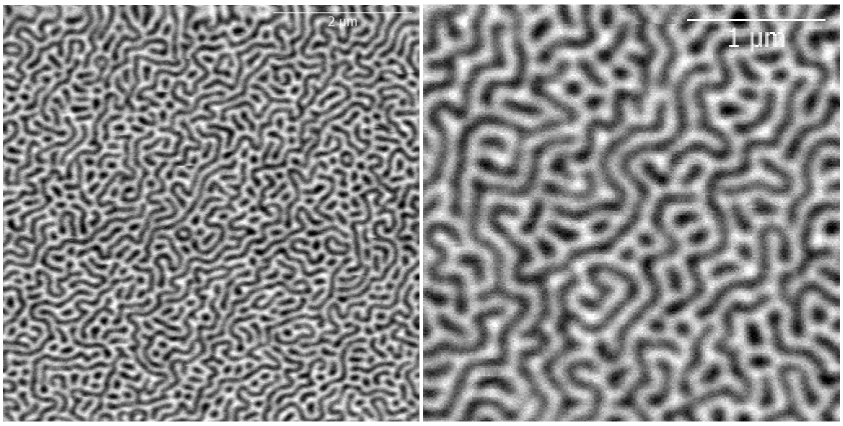

Figure 12 and 13: mangnetic bubbles induced by a strong Out Of Plane field.

It is not possible by now with our instrument to perform an MFM measurement applying a Bias OOP field to produce single bubble domains (as one could expect from this kind of starting domains configuration) but we could see that as it is possible to pass from stripe domains pattern to a this new regime (of mixed bubble domains) it is also possible the inverse process, and the mechanism is totally reproducible. We show this applying a +800 Oe field along an in plane direction and the result is shown in the image below (Fig. 14)

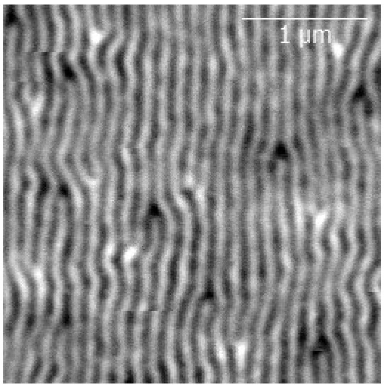

Figure 14: after the application of an in-plane field the stripes return to be aligned.

We then observe the transition from the Mixed Bubble to the stripe domains with an increasing in plane field. After the production of the Mixed Bubbles Pattern by the application of a 1.6 Tesla field perfectly orthogonal to the film ([001] crystallographic direction) we start growing the in plane field along the arbitrary chosen [110] direction. Figures 15 and 16.

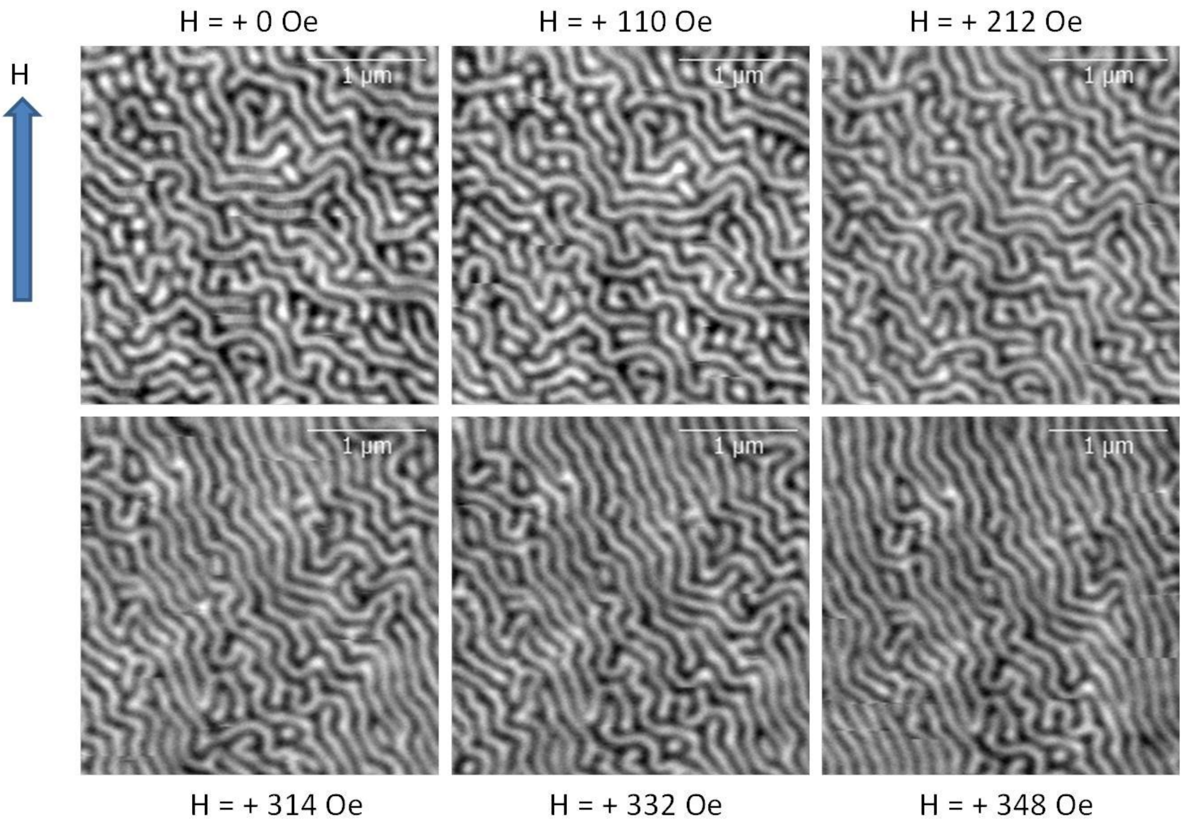

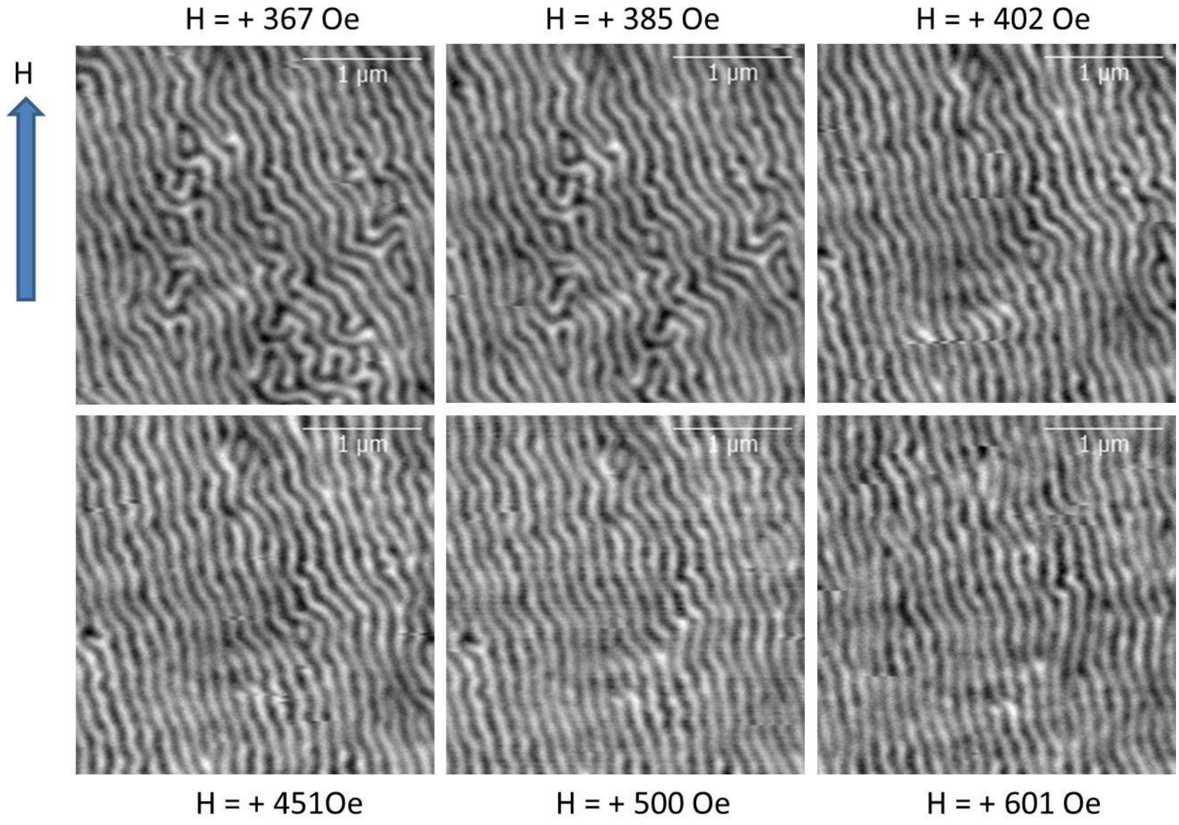

Figures 15 and 16: an incresing in-plane field gradually transform bubble domain pattern in ordered stripes.

Omitting greater field values (because as already said conducting to the stable stripe domains configuration) it is interesting to notice the recurrency of the field range 200 - 400 Oe as the range at which the transition from the mixed bubble to the stripe domains occurs. We conjectured that despite the difference between the reversal of the in plane magnetization and the stripe rotation, the two processes subtend to the same properties that is, the propagation of defects in the domains. It was clear that the reversal required less energy than the rotation because the second process involved a continuous breaking and recomposition of the stripes under different angle. In the case of mixed bubble the situation is not so different: the bubbles evolve with the increasing field until they disappear becoming part of the stripe pattern. Moreover it is helpful to highlight that under the application of about one hundred Oe field the mixed bubbles don't change considerably, but start to disjoint only above 200 Oe: the same field at which the in plane reversal starts. So there should be a bond between the reversal through the bifurcations propagation and the dismemberment of the bubble domains as it would be, if we considered both the bubbles and bifurcation as topological singularities born in defect points.

Another connection between the in plane magnetized domains and the mixed bubble domains in this film comes out from an experiment of stripes rotation: after have induced the stripes along the in plane [110] direction we applied an increasing field along the in-plane [1-10] direction (perpendicular to the stripes) and we performed the MFM measurements in field (see fig. 17). At a field of 419 Oe it is possible to identify two bubbles with opposite polarity (one with the core prevalently upward magnetized and another with the core downward magnetized). At a greater field 484 Oe one of the bubble disappears and leaves place to a stripe domain forming a larger angle with the starting [110] direction. In a 544 Oe field also the second soliton disappeared and another portion of stripe pattern rotated along the field direction. At this field the pattern is rich of bifurcation, and one can really realize how the rotation process is accomplished by means of breaking and recompositions of defects in the stripes pattern. The bubble domains seem to be in this sense a stripe domain that wraps on itself in a defect point or a dislocation. One should notice that the average diameter of a bubble domain is comparable with the period of the stripes: notwithstanding they are two different kind of domain, the minimization of the involved energies brings to the same periodicity.

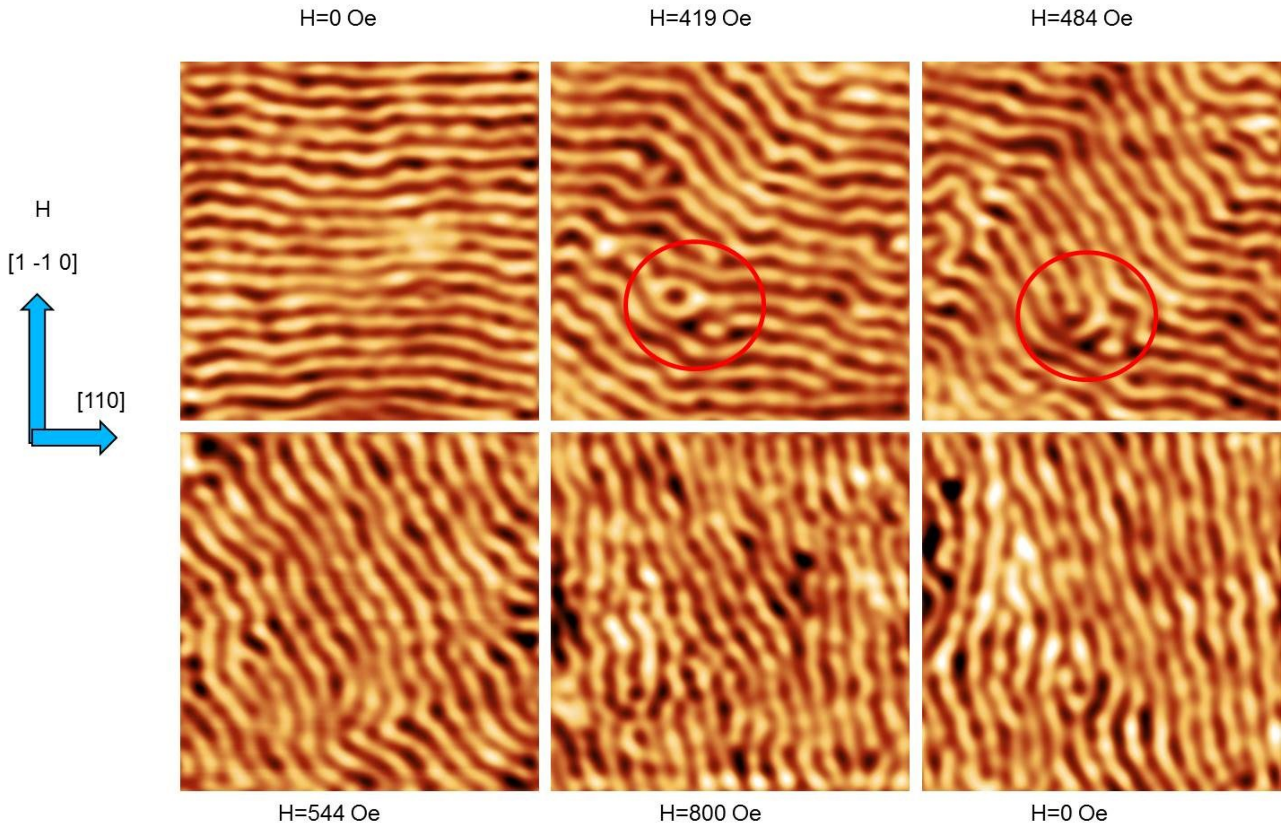

Figure 17: bubble domain in stripe rotation process.

We showed that there is not a precise separation between stripe domain pattern and mixed domains and we can easily travel from one configuration to another acting with an external field. The mixed bubble domains are produced by the application of a perfectly orthogonal to the film field (without this condition, stripes pattern forms along the in plane component of the field), but once the bubbles are formed, they are relatively stable and their destruction requires a field near to the in-plane reversal one.

## Conclusions

In this chapter we studied the magnetic properties of the FeGa thin film deposited on ZnSe/GaAs(001) with a Ga concentration above 15% (the transition composition between the Fe-like to the FeGa magnetic behavior) with thickness between 70 and 90 nm. The FeGa as deposited shows no in-plane Easy direction but presents a relevant Perpendicular Magnetic Anisotropy that allows the formation of stripe domains with period of about 90 nm. The stripes can be rotated by the application of a field of about 800 Oe and remain rotated even after the field removal and that direction becomes the easy one. This effect is known as Rotatable Anisotropy, an unusual type of magnetic anisotropy which we tried to better comprehend creating a link to its dynamical and its static definition. With the Magnetic Force Microscope we imaged the stripe rotation process and obtained the means rotation angle as function of the applied field. With the Brillouin Light Scattering method we derived the spin-waves frequencies as function of the angle between the stripe axis and the transferred wave vector of the incident light. By means of a formula that expresses the spin-wave frequency as function of the applied field and the angle between the stripe and the transferred wave-vector we connected the data from MFM and BLS, calculating the value of the Rotatable Anisotropy field Hrot introduced as fit parameter without which neither the theoretical frequencies of the modes nor the theoretical angles of the stripes vs field didn’t match with the measured one. At this point we described how the magnetization reversal occurs and found that when the magnetization change sing, the OOP component of M transverse to the stripes axis undergoes to a shift of an half period inverting its sign along the perpendicular direction. The mechanism realizes through a series of propagation of dislocations (bifurcations).

The same mechanism guides the rotation of the stripes but with the sequence breaking-rotation-recomposition of stripes in correspondence of those defect points. Finally we showed that is possible to induce a particular magnetic distribution called “Mixed Bubble Pattern” applying a strong field perfectly orthogonal to the film surface (and the orthogonality is necessary condition) that remains also after the field removal. The domains formed in this way (bubbles and stripes) are meta-stable and maintain the same lateral dimensions (for the bubbles we can talk of diameter) than the alternative configuration with aligned stripes.

# Terbium-Iron-Gallium

## Introduction

In the previous chapter we treated the study of thin film systems made of the magnetostrictive alloy FeGa with a relevant PMA which allows the formation of an ordered stripe domain pattern and we described and tried to give a better explanation of the Rotatable Anisotropy. Materials systems with perpendicular magnetic anisotropy (PMA), but in general with arbitrarily adjustable magnetic anisotropy are of great interest because of their applications on patterned media for magnetic storage or in spintronic devices (54) (55). Systems exhibiting PMA have larger magnetic anisotropy energy and the domain configuration is more stable and uniform as compared to most of in-plane anisotropy materials (56). For example, in spintronic devices with ultrahigh density, it is necessary to employ systems with an anisotropy energy constant equal or higher than $10^7$ erg/cm$^3$ (54). Nowadays, different approaches are analyzed to reach this high magnetic anisotropy, leading to various structures such as FePt and CoPt layers (57) (58), multilayer comprising magnetic transition metals (Co, Fe, CoFe) and noble metals (Pt, Pd, Au) (59) (60) (61) or FeCoB layers with PMA (62). We have investigated the domain shape and behavior of cosputtered TbFeGa thin films, deposited by evaporation from two separated cells ($TbFe_2$ and $Fe_3Ga$) using alternately two different power sources (DC or Pulsed) on the cells.

## Production of TbFeGa Thin Films

Samples were deposited (by Dr. Rocio Ranchal at University Complutense in Madrid) (63) at room temperature on 5 x 4 mm$^2$ glass substrates. Two targets with a nominal composition of $TbFe_2$ and $Fe_3Ga$ were employed to deposit by cosputtering the alloys. The cosputtering process was performed in the oblique incidence, being the angle of incidence between each target and the substrate of about 25 degrees (64) (65) and the distance between the targets and the substrate of 15 cm. Two series of samples have been obtained depending on the type of power source (DC or pulsed) used in each target. In series A, a fixed DC power of 100W is applied in the $Fe_3Ga$ target and different compositions are achieved by modifying the pulsed power from 60 to 120 W in the $TbFe_2$ target. In series B, the DC source is applied at a fixed power of 100W in the $TbFe_2$ target, whereas the pulsed power ranged between 80 and 120W in the $Fe_3Ga$. In all cases, the frequency (25 kHz) and the dead-time (5 µs) were fixed parameters in the pulsed source. The thickness of the TbFeGa layers was around 250 nm. Mo layers (20 nm) were used as buffer and capping layers for all the samples. They were grown with a DC power of 90 W. The Ar pressure was $2x10^{-3}$ mbar to evaporate all the layers: buffer, capping, and ternary TbFeGa alloys. The samples grown are listed in table 1, and for every sample the anisotropy direction and value, the compensation temperature and the composition are reported.

The composition of the samples was analyzed by means of the Energy Dispersive X-ray Spectroscopy (EDS) in a Leica 440 SEM microscope operated at 10 kV and 2 nA. θ-2θ X-ray diffractometry patterns were measured in the Bragg–Brentano configuration. At room temperature, in-plane and out-of-plane hysteresis loops were performed in a vibrating sample magnetometer (VSM). In the VSM we can measure the in-plane loops at different angles between the applied magnetic field and the in-plane reference direction. Moreover field-cooled (FC) curves were performed in a superconducting quantum interference device (SQUID) magnetometer as done and explained in a previous work (66). Before measuring the temperature dependence of the magnetization, the sample was first cooled from room temperature to 5 K under a saturation field of 2 kOe and then, the FC curves were recorded with an applied magnetic field of 100 Oe during the warming-up. We have measured the composition of all the samples by the EDS technique

(Table 1). The TbFeGa alloys were compositionally homogeneous and we have not observed any of the compositional fluctuations.

By means of the technique used in the present work we are able to tune the composition of the samples acting on the growth power. The decrease (increase) of pulsed power in the $TbFe_2$ ($Fe_3Ga$) target raises the Ga content in the TbFeGa alloys. Moreover, the use of a DC or a pulsed power source in each target allows to obtain the same composition from different growth conditions (Table 1).

Table 1

| Composition | Growth conditions | Magnetic anisotropy (erg/cm$^3$) | $T_{Comp}$ (K) | Tb in the $Tb_xFe_{1-x}$ (at.%) | |
|---|---|---|---|---|---|
| $Tb_{10}Fe_{77}Ga_{13}$ | $TbFe_2$. Pulsed: 120 W $Fe_3Ga$. DC: 100 W | PMA $\geqslant 1.5 \times 10^6$ | $\geqslant$300 | $\geqslant$28 | Series A |
| $Tb_{10}Fe_{76}Ga_{14}$ | $TbFe_2$. Pulsed: 100 W $Fe_3Ga$. DC: 100 W | Weak PMA $0.6 \times 10^6$ | 176 | 22 | |
| $Tb_9Fe_{75}Ga_{16}$ | $TbFe_2$. Pulsed: 60 W $Fe_3Ga$. Pulsed: 100 W | In-plane $0.5 \times 10^6$ | 31 | 18 | |
| $Tb_{10}Fe_{77}Ga_{13}$ | $TbFe_2$. DC: 100 W $Fe_3Ga$. Pulsed: 80 W | PMA $\geqslant 1.5 \times 10^6$ | $\geqslant$300 | $\geqslant$28 | Series B |
| $Tb_{10}Fe_{76}Ga_{14}$ | $TbFe_2$. DC: 100 W $Fe_3Ga$. Pulsed: 100 W | PMA $1.0 \times 10^6$ | $\geqslant$300 | $\geqslant$28 | |
| $Tb_9Fe_{75}Ga_{16}$ | $TbFe_2$. DC: 100 W $Fe_3Ga$. Pulsed: 120 W | In-plane $0.4 \times 10^6$ | 15 | 16 | |

X-ray diffraction patterns of the two series of samples only exhibit one main diffraction peak at around $2\theta \approx 40.5°$ (Figure 1). This peak is close to the peak of the $TbFe_2$ Laves phase, that appears at $2\theta = 40.74°$. We have not found evidences of any other peak close to any of those previously reported in $Fe_{1-y}Ga_y$ or TbFeGa alloys and then, the experimentally observed diffraction peak can be related to the presence of crystalline $Tb_xFe_{1-x}$ phases with a structure close to the cubic $TbFe_2$. In any case, the intensity of this peak is low and we can consider our samples as polycrystalline.

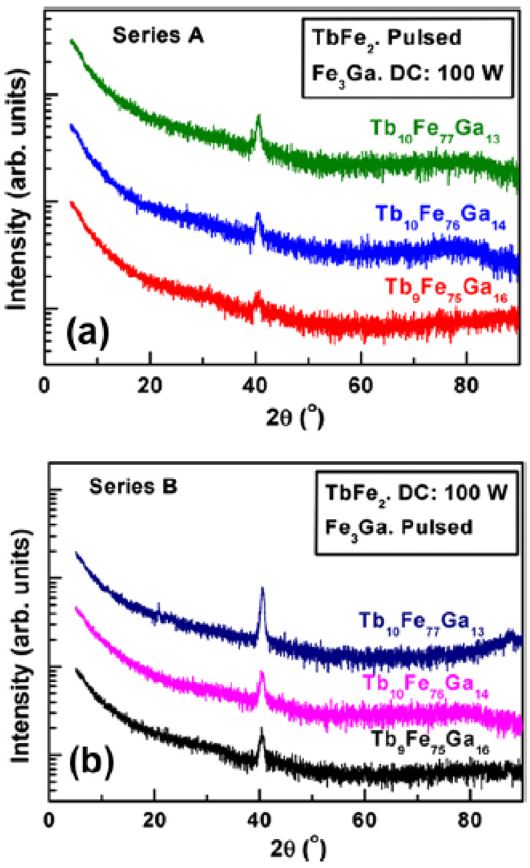

Figure 1

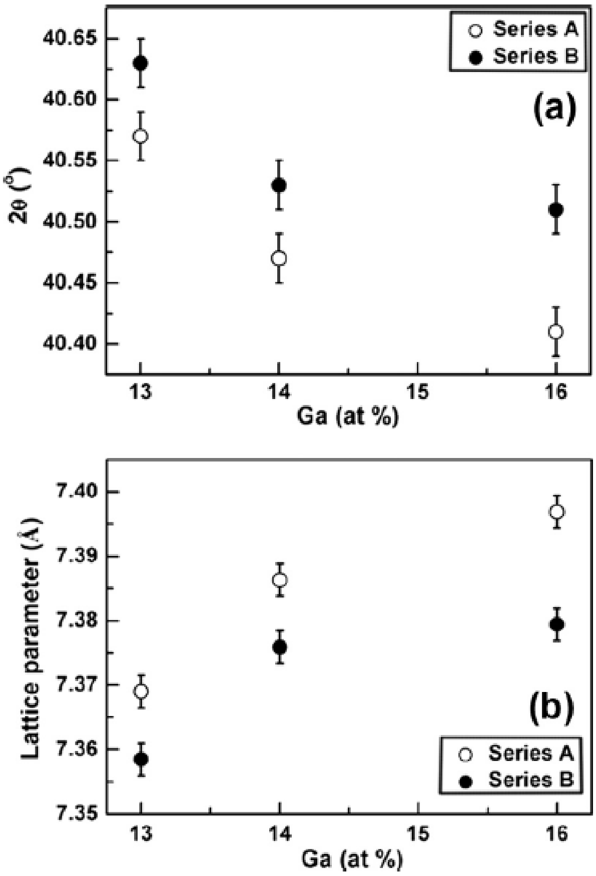

Figure 2

In Fig 2a we present the diffraction angle as a function of the Ga content for the two series of samples. In both series, the decrease of the Ga content shifts the diffraction peak towards the theoretical diffraction angle of the $TbFe_2$ cubic structure (40.74°). Nevertheless, for samples with the same composition the position of the diffraction peak depends on the growth conditions. The peak appears closer to 40.74° in layers from set B (Fig. 1b) revealing a structure more similar to the $TbFe_2$. We have calculated the lattice parameter from the diffraction scans considering a cubic structure (Fig. 2b). In all cases, the lattice parameter is higher than the theoretical value of $TbFe_2$ (7.341 Å) and in both series it depends on the Ga content. Mo grows as a polycrystal on glass and there is a possible influence of the lattice mismatch between Mo and TbFeGa.

The influence of the Ga content and the growth conditions on the lattice parameter (Fig. 2b) is greater than a hypothetical lattice mismatch between the Mo buffer and the TbFeGa layers.

The type of power source appears to be relevant since samples with the same composition but deposited in different ways exhibit a different intensity for the diffraction peak and different lattice parameters (Figs. 1 and 2b). The increase of the Ga content promotes the decrease of the peak intensity suggesting that Ga doping disturbs the crystalline structure (Fig. 1). The peak intensity is higher in set B in comparison to A revealing that the use of the DC power source to evaporate the $TbFe_2$ favors layers with a higher structural quality. Moreover, layers of set B have a lattice parameter closer to the theoretical value of $TbFe_2$ (7.34 Å) that indicates a $Tb_xFe_{1-x}$ crystalline phase more similar to the Laves phase (Fig. 2b).

We have determined the type of magnetic anisotropy at room temperature following the methodology used in a previous work (64). In Table 1 we have summarized the magnetic anisotropy found in each sample following this procedure. In the two series of samples, the magnetic anisotropy evolves from in-plane to PMA as the Ga content is decreased. In the VSM, the maximum possible applied magnetic field was of 12.5 kOe and in some cases, the hysteresis loops could not be saturated. In Table 1 we present the inferred values for all the studied samples although the anisotropy constant could not always exactly be evaluated. In samples showing a clear PMA, we have inferred an anisotropy constant of at least $10^6$ erg/cm$^3$, a value of the same order of magnitude to what reported in (67) (68). Nevertheless, the growth conditions also have an effect on the anisotropy. The $Tb_{10}Fe_{76}Ga_{14}$ alloy does show a different anisotropy in each set of samples and in Fig. 3 we present the VSM hysteresis loops recorded with magnetic field applied perpendicularly and in-plane: the magnetization curves indicate that the alloy from series A exhibits a weak PMA (Fig. 3a) whereas the samples from series B show a distinct PMA Fig. 3b). Moreover, the inferred anisotropy energy constant is different in each sample (Table 1).

Therefore, the magnetic anisotropy can be tuned by means of both the composition and the type of power source (growth conditions).

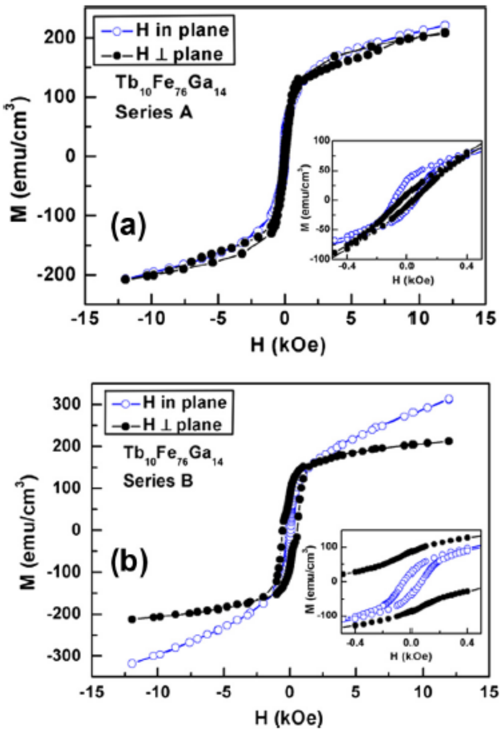

Figure 3: in-plane and out-of-plane hysteresis loops for both A and B samples.

## MFM and MOKE measurements

In order to gain a deeper insight into the properties of TbFeGa alloys in thin film form we have performed Magnetic Force Microscopy measurements on all the samples described in this paper. Films with high PMA often show stripe domains, as in the case of the thin film (FeGa) treated in previous chapter. We starting by measuring TbFeGa film of series A and with increasing content of Ga.

Henceforward we will indicate the sample listed in Table 1 as A1, A2 and A3 for series A and B1, B2, B3 for those of series B: an increase of the index number indicates a reduction of the Ga content.

## Series A

We want to describe the MFM results beginning from sample A1. In the image 4a we show the MFM image performed at remanence. The magnetic signal is formed prevalently by mixed bubble and stripe domains without a preferential orientation. We applied an 8 kOe field along the indicated direction and the resulting magnetization configuration is reported in image 4b. As one can see, in spite of the strong in plane field applied, the stripe domains have not assumed any particular orientation and are substantially unchanged. In the figure 4c we performed an IN-FIELD measurement with a 800 Oe field (in the same direction) and observed the same area of the previous measurement. When the two last images are compared, one sees that nothing changed and that the stripe domains are exactly identical. The strong PMA not only allows the creation of this kind of magnetic domains with a net upward/downward Out Of Plane component of the magnetization but is strong enough that a 800 Oe field is not sufficient to alter them. Notice also that bubble-like domains are present, in agreement with the previous statement in which we said that a greater PMA favors the existence and stability of that kind of domains.

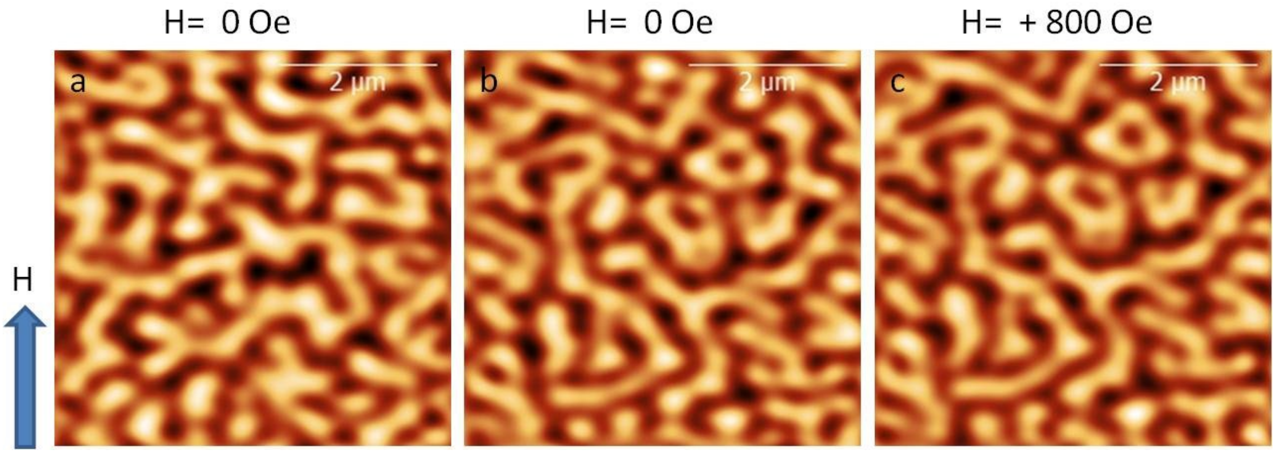

Figure 4: MFM image of the sample A1, at remanence (a), after the application of a strong field (b) and in a 800 Oe field (c).

The MFM image at remanence on the second sample A2 is reported in figure 5.

This sample has a weaker PMA with respect to the sample A1 and shows a magnetic domain patter very similar (in shape) to the previous one, but with a stripe lateral dimension very different.

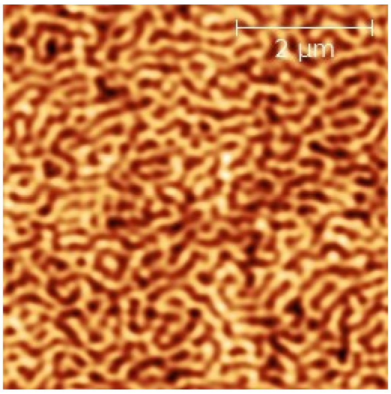

Figure 5

In order to show this, we computed the 2D Fast Fourier Transform to determine the so called Power Spectral Density (PSD) distribution, whose maximum represents the average dimension of the domains. In the image 6 the 2D FFT for the sample A1 is reported.

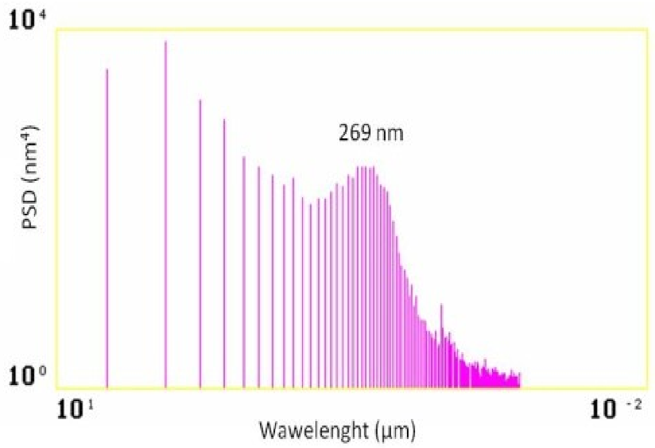

Figure 6: PSD of the MFM image at remanence for the sample A1.

As the reader can see, the maximum value of the PSD for the sample A2 is 269 nm.

Then we applied an 800 Oe in plane magnetic field (see fig. 7a) and we saw that it is sufficient to completely annihilate the OOP magnetic signal or equivalently to achieve the total reorientation of the perpendicular component of the magnetization along the field direction. This effect is proved also by means of MOKE magnetovectometry, as reported in figure 8, where in the ordinates the ratio $M_z/M_{sat}$ versus the applied in plane field gives the behavior of the OOP magnetization.

Therefore the weakening of the PMA on this thin film produced stripe domains with a lower lateral dimension (or period) and with a weaker strength of the OOP component of the magnetization with respect to the previous sample A1.

Reducing the external field to 400 Oe (figure 7b) we saw that the domains reappear and finally, shutting off the field (figure 7c), we observed that the domain pattern is preferentially oriented along the field application direction. The stripes followed a rotation mechanism similar to what described in the previous chapter concerning the FeGa thin films.

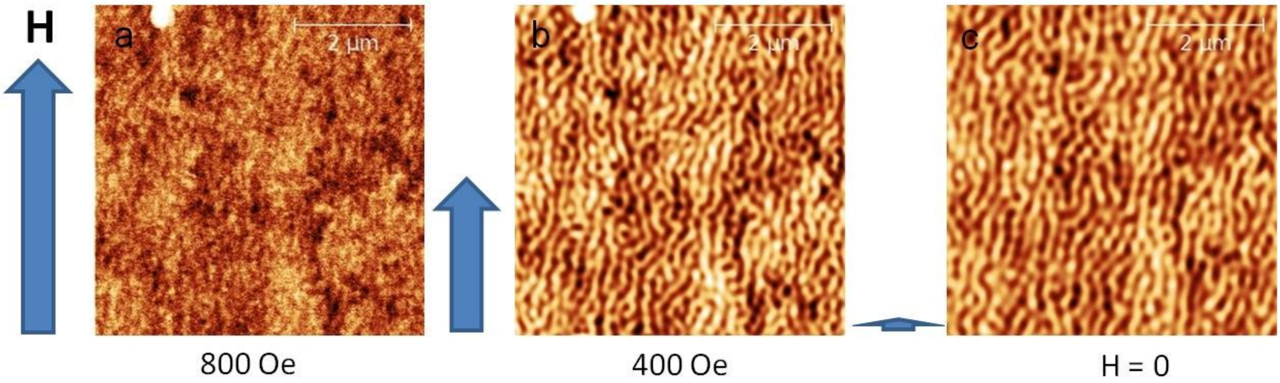

Figure 7: MFM images of the sample A1 performed in-field (a), at 400 Oe (b) and at remanence (c).

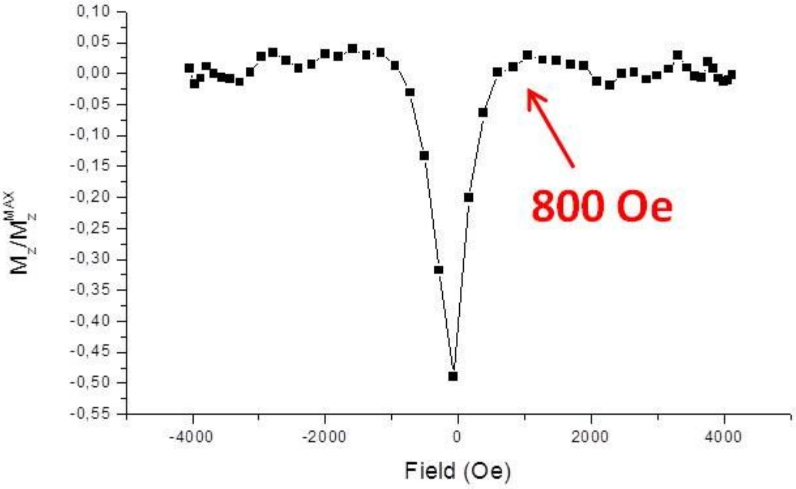

Figure 8: behavior of the OOP component of the magnetization during an hysteresis cycle with the field applied in plane.

To get more insight into the stripes pattern reorientation process we performed the in-field rotation of the domains by applying a transversal field as shown in figure 9.

Due to the fragmentation of the domains in mixed bubble and stripes (even at remanence), a precise domain’s orientation cannot be defined and a coherent rotation process cannot be observed; therefore a precise detection of the angle vs field dependence could not be established.

Nevertheless it is possible to notice that in a field range between 330 and 470 Oe the rotation achieves its completion and after the OOP saturation in a 800 Oe field, the stripes are preferentially rotated along the field direction after the field removal.

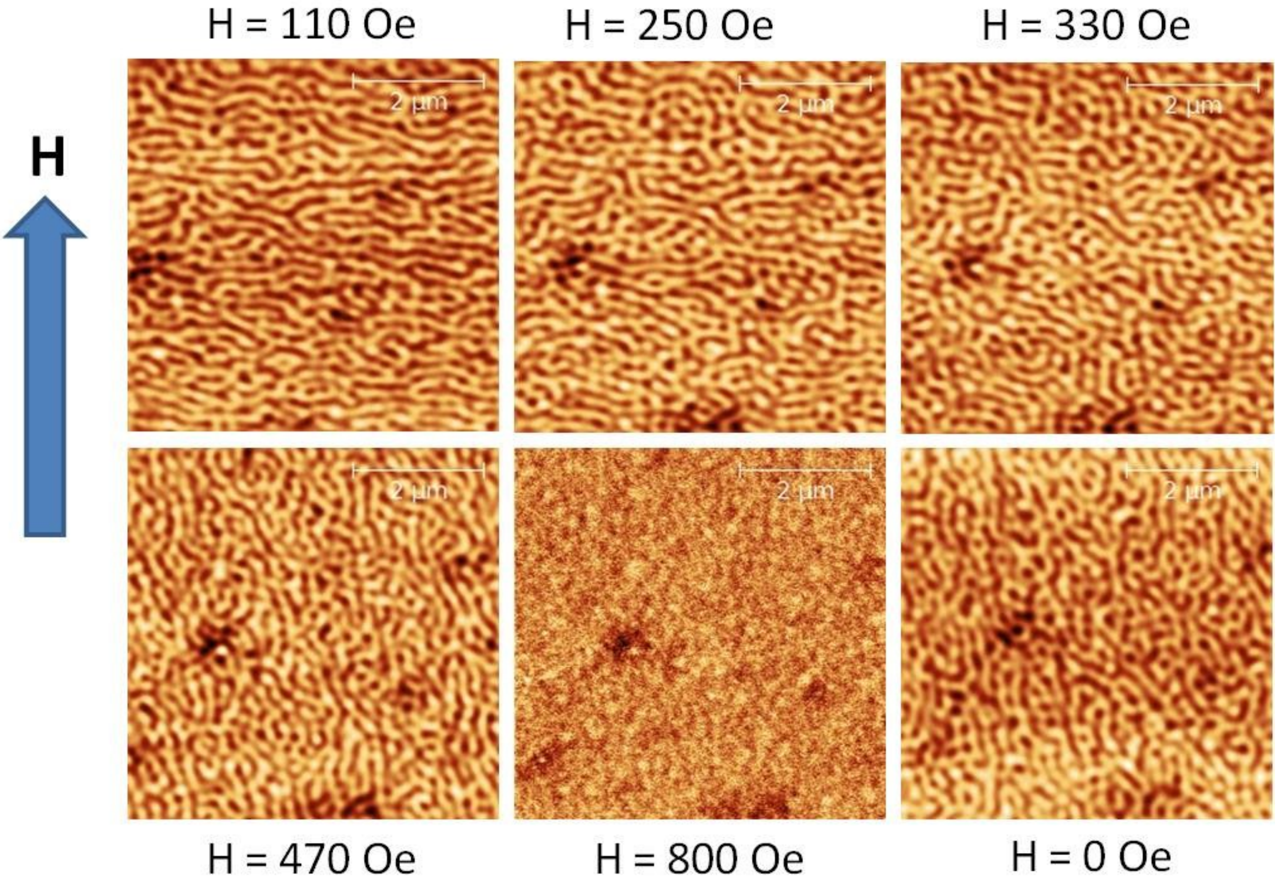

Figure 9: stripes reorientation under the application of an increasing in-plane field.

We can also in this case refer to Rotatable Anisotropy due to the character of directional stability of the stripes pattern once they are rotated, even though with all the restrictions of the case (absence of the dynamical counterpart, absence of a pure stripe domains pattern, impossibility to study the stripes angle dependence with the external field strength).

The last sample of the A series, A3, is the one with the minimum content of Gallium and from the preceding VSM characterization we revealed that it has a little perpendicular magnetic anisotropy, comparable but lower than that of the sample A2. The MFM image performed at remanence and in field is reported below in figure 10.

The case of the sample A3 is the most unusual for the presence of two different magnetic phases that are revealed when the sample is subjected to an in plane field.

In figure 10a the MFM image performed at remanence is reported. On the visible magnetic phase (that we can call "first magnetic phase") we distinguish little domains with a structure that fairly recalls the mixed bubble domain pattern with a very little lateral size. Increasing the applied in plane field to 250 Oe (figure 10b) it seems that while the little domains start disappearing, a second structure with a net OOP magnetization emerges. At 800 Oe the first phase is completely annihilated while the second structure dominates (hereafter we call it "second magnetic phase").

After the field removal (fig. 10d) the system returns to its previous configuration, and there is a coexistence of the two phase phases.

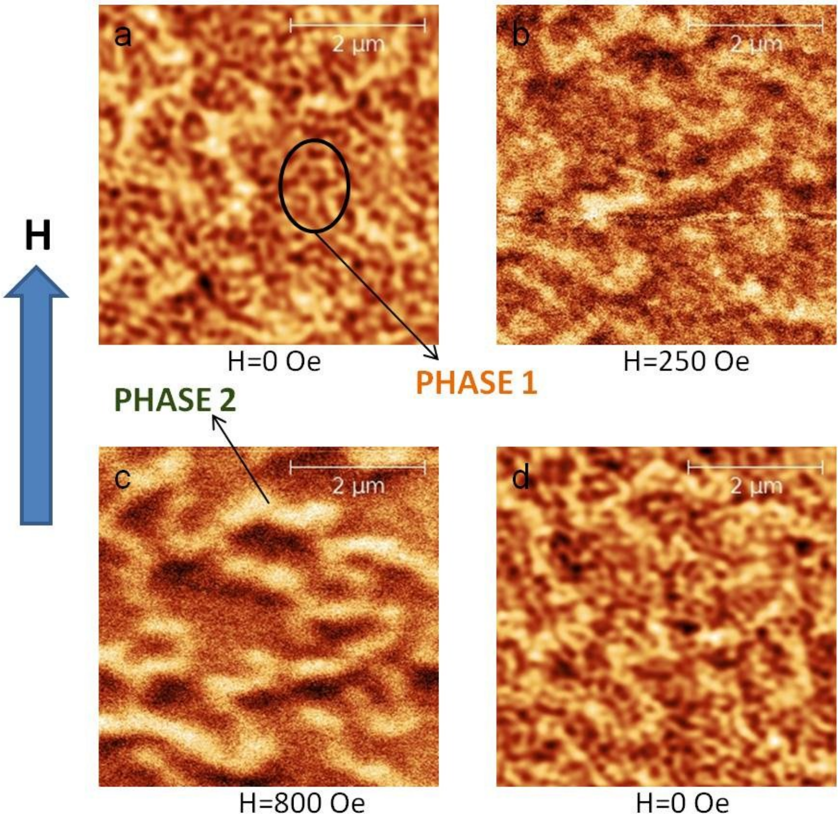

Figure 10: in-field MFM images for the sample A3.

Up to now we didn't find an unquestionable explanation of this particular double magnetic phase coexistence. Our data suggest (as would become more clear later in this chapter) that due to the growth conditions, the creation of a $TbFe_2$ crystalline phase immersed in an amorphous TbFeGa phase would be favored: the two magnetic phases could be associated to two different crystallographic phases induced by the particular growth parameters (both pulsed on the $TbFe_2$ and the $Fe_3Ga$ target, see table 1).

## Series B

The first two samples of series B have both a strong PMA and, as it is predictable, the domains of these two samples are formed by mixed bubble and stripe pattern. We treat the two samples in the same paragraph due to their reciprocal similarity, as the reader can see observing their MFM image at remanence (figures 11a and 12a)

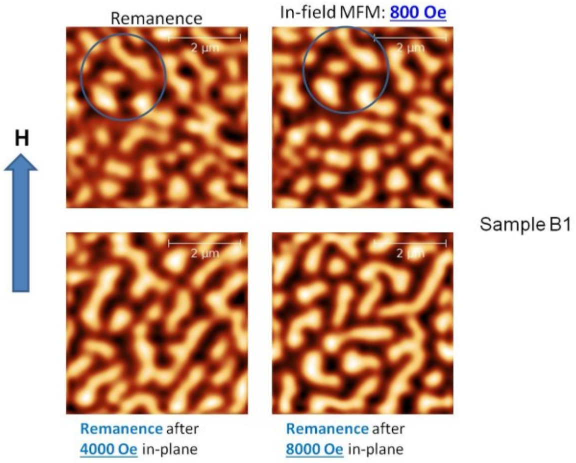

Figure 11: sample B1

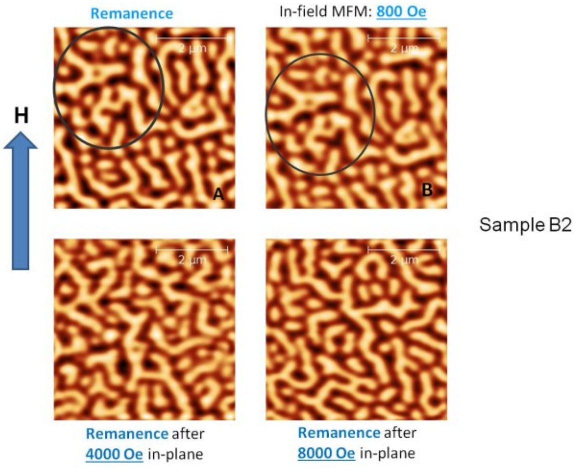

Figure 12: sample B2

The 2D Fast Fourier Transform analysis reveals an average domain lateral dimension of about 850 nm for the sample B1 and about 550 nanometers for the sample B2. The larger is the PMA value the bigger is the size of the stripe.

The application of an in plane field up to 800 Oe doesn't modify the aspect of the domains. The surface region indicated with a circle in the insets a and b of both the figures 11 and 12 encloses domains that result completely unchanged in a 800 Oe field (applied in plane) with respect to the same area at remanence. This is due to the strong PMA that generates domains with an OOP component of the magnetization very robust under the influence of an external field.

Finally we apply a strong external in plane field, up to 4000 Oe and after up to 8000 Oe. For the sample B1 we assist to a little elongation of domains (not along the field direction); in the sample B2 nothing considerably changes.

We finally mention sample B3, that having no PMA, doesn't show any OOP signal when analyzed with Magnetic Force Microscope.

In conclusion: the growth conditions play a crucial role in determining the out of plane (OOP) component of the magnetization in TbFeGa alloys. The Perpendicular Magnetic Anisotropy (PMA), the size and topology of domain patterns can be tailored by changing the evaporation parameters of $TbFe_2$, being the series A and B grown with different power sources but delivering to the same composition. The OOP component of the magnetization is enhanced when the DC power source is used to evaporate the $TbFe_2$ (samples B, strong PMA). We correlate this effect with Tb enrichment of the $Tb_xFe_{1-x}$ phases present in the samples.

Films with a weak PMA display rotatable anisotropy (sample A2): stripes direction can be changed by an external field and maintained when the field is switched off.

Finally we have found two different magnetic phases that can coexist in a films with weak PMA (samples A3) but we have not yet found a satisfactory explanation of this result (although some steps forward are already done).

# Arrays of magnetic nanoparticles: “Configurational Anisotropies”

# Bicomponent Ellipses (Co/Py, Py/Ni): Configurational Anisotropy

## Introduction

In the previous two chapters we discussed the magnetic peculiarities of thin films like perpendicular and rotatable magnetic anisotropies, and studied how the anisotropy influences the domain's configuration and stability. The concept of perpendicular magnetic anisotropy is related to the fact that the thin film has one of the three spatial dimensions limited in the range of the mesoscopic scale (under the micron) or in the nanoscale (few tens of nanometers). In the field of nanophysics, the reduction of one dimension under the microscopic scale is equivalent to produce a 2 dimensional object (69): only thanks to the low dimensionality the stripe domains with the above described characteristics can form because they are the result of the competition between the Perpendicular Magnetic Anisotropy and the dipolar energy that favors the in plane magnetization in a two dimensional nanostructure. If we limit the dimension of 2 sides of an object reducing again the dimensionality of the nanostructure, we obtain a wire. We can reduce all the 3 spatial dimensions under the microscopic scale and we can speak about "dots". A magnetic dot has magnetic properties that differ from the 3D (or bulk) counterpart or in general from objects made of the same material but with different dimensionality.

In the last decade magnetic dots have been extensively studied in their different shape or dimension, either from the point of view of the static magnetic domain configuration and hysteresis behavior or in the field of the dynamical spin-waves spectrum (70), (71), (72), (73), (74), (75). For example acting on the shape we can modulate the so called "shape anisotropy" creating easy direction along the major axis of an elliptical or rectangular dot (5). We can also change the ferromagnetic material keeping the same shape. Finally it is possible to bring two different dots very close and their mutual interaction modifies the properties of each single dot: this last case is a type of “configurational anisotropy” (76) due to the fact that with the same dot shape we can construct an infinite combination of 2 or more dots that interact reciprocally and giving to the system different magnetic properties.

We aim to modify together the configurational anisotropy and the composition of the dots, acting both on the reciprocal position of dots and changing the material in the same configuration. To this purpose a collaboration with different international partners have been started for the production and characterization of samples. In particular the group of professor Adeyeye (University of Singapore) provided the samples, the group of professor Giovanni Carlotti (University of Perugia) performed the BLS measurements. Here in Ferrara the group of magnetism performed the simulations, MOKE and MFM analysis of samples.  We produced four series of samples all with the same base shape consisting of two ellipses very close and parallel along the long axis, constituted of two different materials that we call “bicomponent dots” or ellipses. Two series are made of bicomponent particles (interacting and non-interacting along their easy axis) of Cobalt and Permalloy, two (interacting and non-interacting) of Permalloy and Nickel, see Figure 1.

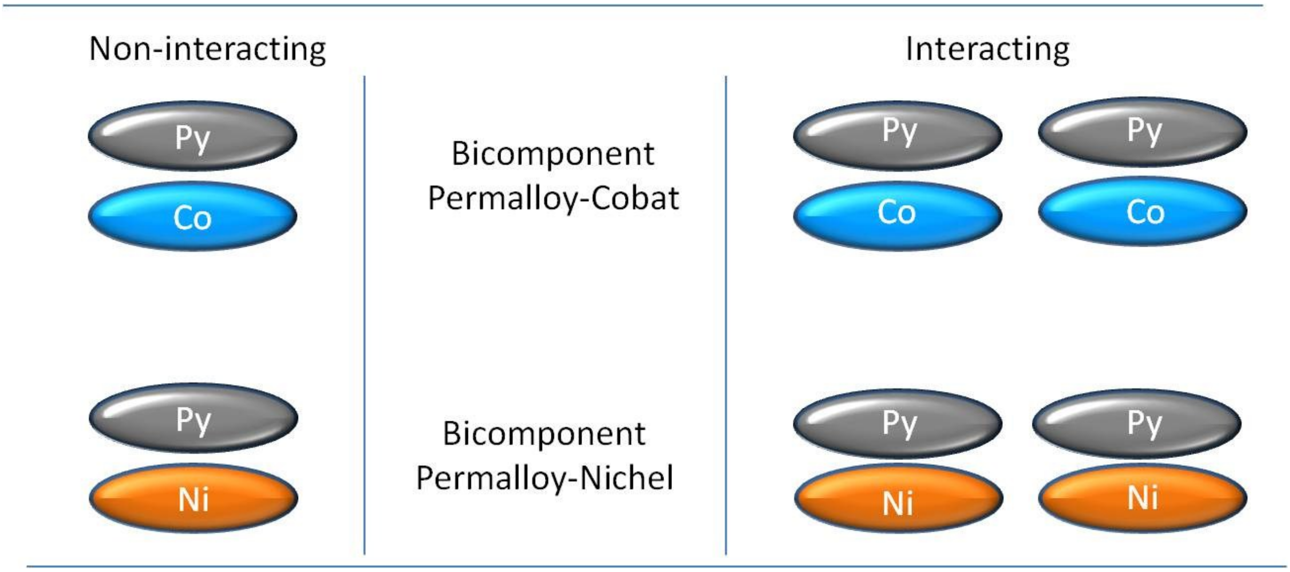

Figure 1: schematic representation of the four different samples produced and analyzed in this work

The major axis of the single ellipse is 1 micron and the minor axis is 200 nm. The thickness for all the samples is 25 nm.

In both interacting Co/Py and Ni/Py bicomponent nanostructures the separation along the major axis was 140 nm, while in the non-interacting bicomponent the distance was 600 nm. The little separation along the minor axis is about 30 nm.

The sample was produced at Singapore University by prof. Adeyeye and collaborators by a self-aligned shadow deposition technique (77) improved; all the details of this kind of deposition process is well described in the indicated reference.

## Bicomponent Co/Py

### Non interacting Co/Py dots

In the image below (figure 2) we report the hysteresis cycle obtained with MOKE for the Non-Interacting Co/Py bicomponent pattern. The sample was saturated with a strong in-plane negative field and the bicomponent dot was magnetized in the direction of the field. Reading the graph we distinguish a zone in which the hysteresis branch forms a plateau: it corresponds to a state in which the Py particle (that is the softer material) has switched its magnetization along the field direction, whereas the Co particle has not yet switched. The switching process for the Py starts at about 200 Oe, has a maximum rate at about 305 Oe (the slope reaches a maximum, see fig 2), and at about 380 Oe is completed. At this point the particles of Py and Co are magnetized Antiparallel (78).

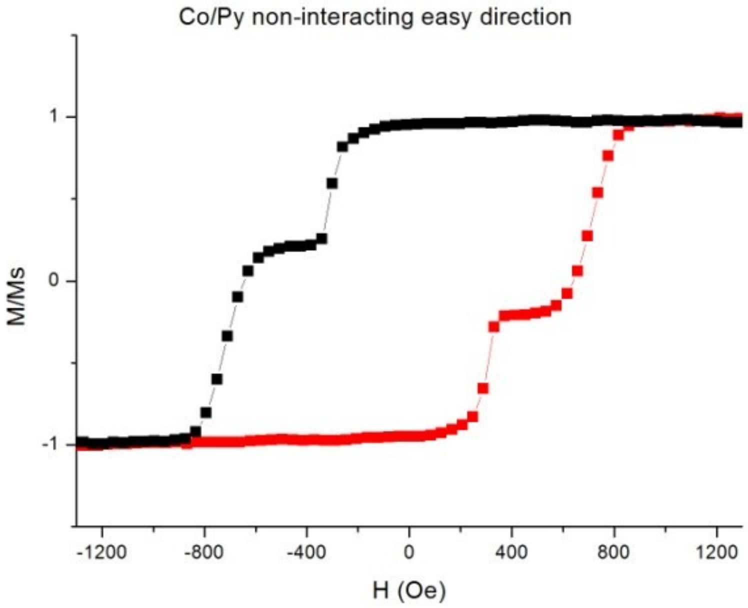

Figure 2: hysteresis cycle obtained with MOKE for the Non-Interacting Co/Py bicomponent pattern

The plateau extends until the Co begins to rotate its magnetization in the field direction, namely at about 580 Oe, then the switching of the Co grows at his maximum rate (corresponding to the maximum of the first derivative dM/dH purple colored in figure 3) namely at 720 Oe. Then the entire system goes to saturation which is reached at a field equal or greater than 900 Oe. The state is characterized with the Co and Py particle magnetized parallel to the applied field.

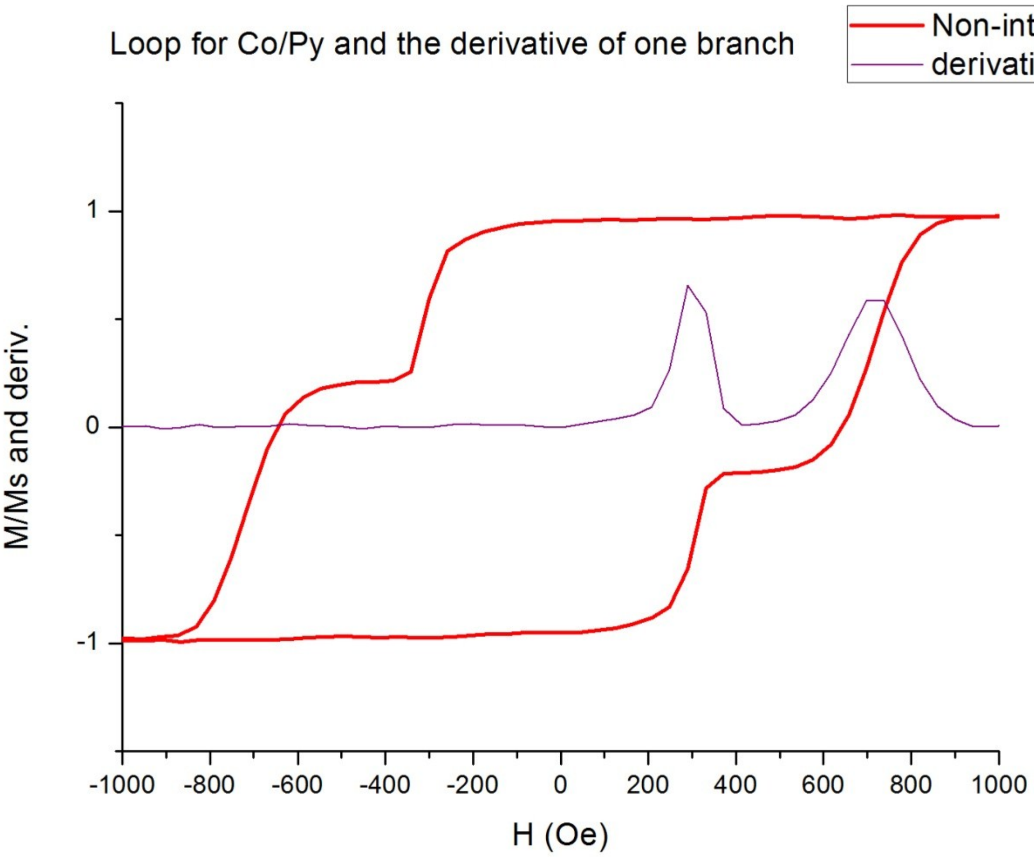

Figure 3: Hysteresis loop produced with L-MOKE along the easy direction for the interacting Co/Py dot pattern.

The entire process was followed also with the Magnetic Force Microscope (See figure 4). Here we report MFM images taken at relevant fields: at the first magnetization change coincident with the Py inversion field, inside the range of the plateau, at the second M change (Co inversion), near the saturation and finally at remanence, after the saturation.

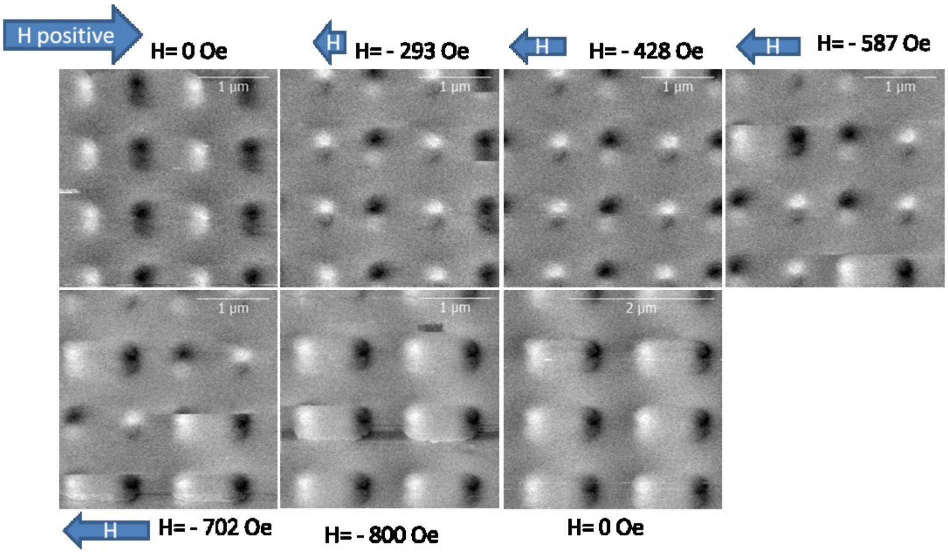

Figure 4: MFM images taken at relevant fields

Notice that after the sample has completed the inversion of magnetization for both particles and the field is lowered to zero, the system remains in a stable parallel state. This could be inferred also from the MOKE cycle, considering that at remanence the magnetization remained near to saturation: a confirmation of the fact that the two particles remain in the parallel state also after field removal.

Let's consider now a minor hysteresis loop, with a field range that stands between the two plateau (figure 5), therefore a range of fields within which only the Py switches, while the Co remains magnetized in a steady direction. Properly we start applying a saturating field in a direction, then passing through the remanent state we increase the external field until We reach 463 Oe in the opposite direction. We are on the plateau so in the field range in which the Py has switched, while the Co has not, we are in the Antiparallel state (AP). Then we go to remanence and observe that the AP state persists. At this point, following the minor loop, we increase the field in the initial direction until the Py re-switches (at +428 Oe) making the system returning in the original Parallel state (P).

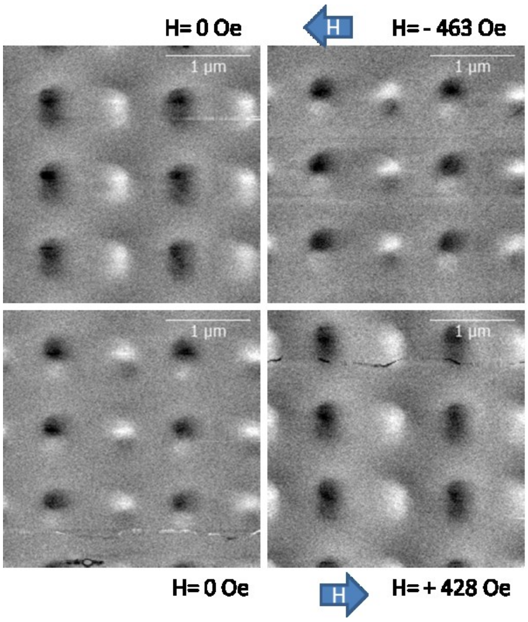

Figure 5: MFM images of Co/Py non-interacting particles produced following a minor loop (within the Py switching fields)

## Interacting Co/Py

We now discuss the case of interacting Co/Py particles consisting of a chain of bicomponent Co/Py dots disposed head to tail along the easy magnetic direction with a distance of about 140 nm. We report the hysteresis cycle along the easy direction in Figure 6. The shape of the branches is very similar to the case of non-interacting particles: from the saturation parallel state, there is a Py switching field that brings the system on the plateau, corresponding to the AP state. Continuing the field increase also the second material starts to invert its magnetization in the field direction, until the achievement of the P state and then the saturation is obtained. The main differences between single particle and interacting particles pattern are the switching fields and consequently the plateau widths and positions and we'll discuss this feature in detail later in a next section.

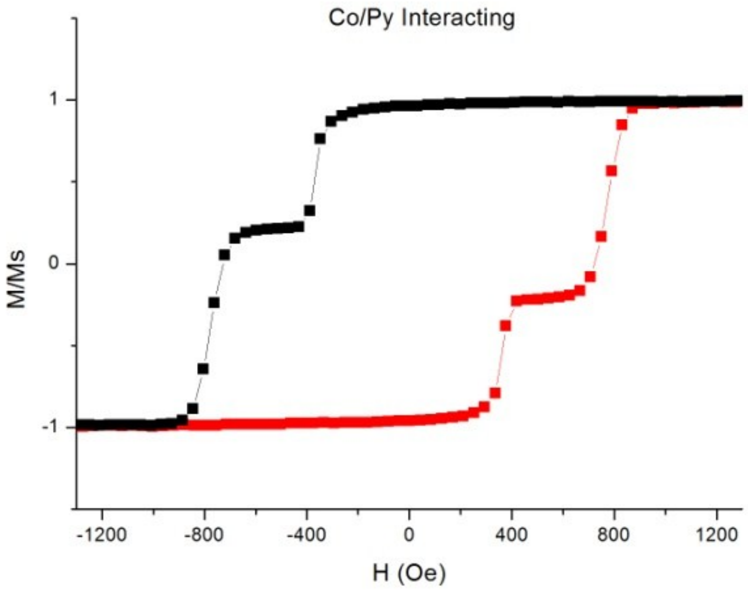

Figure 6: hysteresis cycle obtained with MOKE for the Interacting Co/Py bicomponent pattern

We now continue with the description of the interacting bicomponent chain, showing the MFM images correspondent to the ascending branch of previous hysteresis loop (see figure 7).

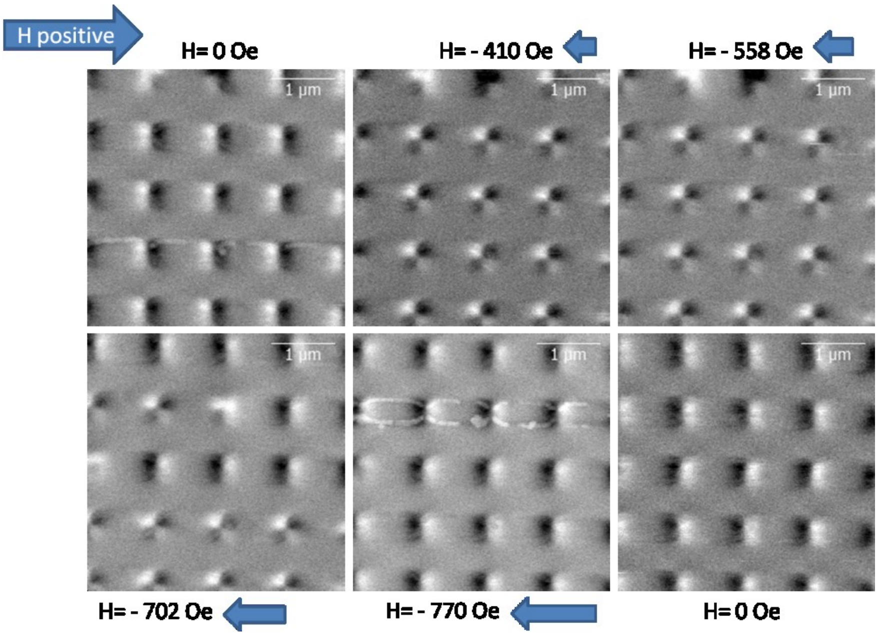

Figure 7: MFM images of the Interacting Co/Py taken at relevant fields.

As in the case of non-interacting particles we reported the more significant MFM images, corresponding to relevant external field values; in particular in the images above we see the magnetization configuration at remanence, after the application of a positive saturating field, two images at the beginning and in the middle of the plateau (-410 and -558 Oe), at the end of the plateau (-702 Oe) when the Co start switching, and near the end of the slope (-770 Oe). The last image is kept at remanence, after we have saturated the sample. See as all the particles remain in the P state, stably.

For completeness we report the MFM images taken following the minor loop as we did in the case of non-interacting particles (figure 8).

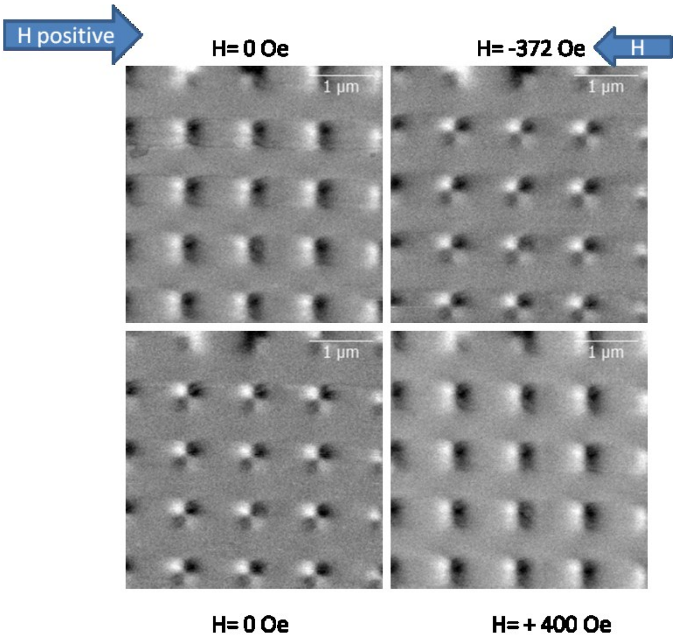

Figure 8: MFM images of Co/Py Interacting particles produced following a minor loop (within the Py switching fields)

## Comparison between interacting and non-interacting Co/Py particles

Below in figure 9 we report the hysteresis loops corresponding to the patterns, in particular the red continuous line represents the cycle for the non-interacting dots, while the black continuous line the cycle of the interacting dots.

We observe that the hysteresis curve for the interacting dots is wider than the other and that the plateau is larger. Going from the remanence to greater positive field we see that the switching Py field is lower for the non-interacting dots than for the interacting (305 Oe and 360 Oe respectively). This is due to the head-to-tail dipolar interaction whose effect is to keep the magnetization of adjacent Py dots in the same direction and that is greater for the interacting dot. This effect is also indicated as configurational anisotropy that is the magnetic anisotropy rising from the different configuration of a same dot in a pattern. Notice that the two samples reach the saturation at the same external field in spite the different hysteresis.

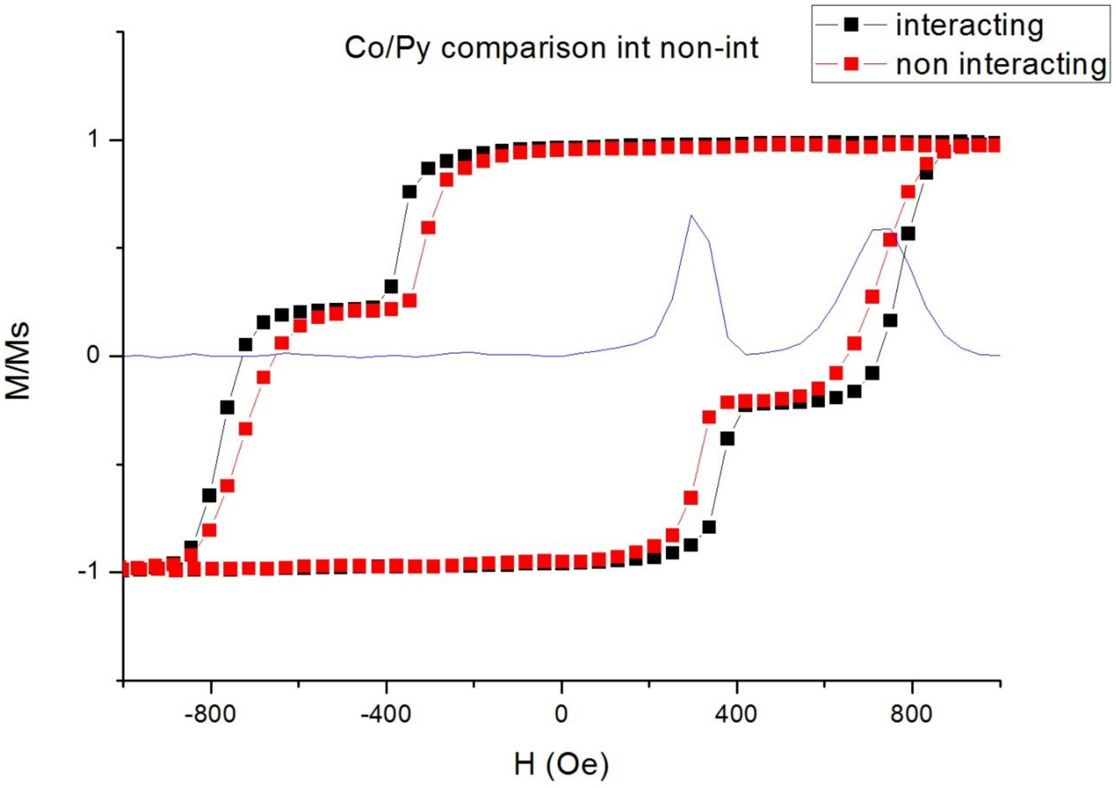

Figure 9: hysteresis loops corresponding to the pattern; the red continuous line represents the cycle for the non-interacting dots, the black continuous line the cycle of the interacting dots. The blue line is the derivative of the positive branch of loop relative to the non-interacting dots.

We found a confirmation of different switching fields also with numerical simulation performed by the micromagnetic simulator OOMMF (acronym for Object Oriented MicroMagnetic Framework).

The simulations were performed by Dr. Perla Malagò (Department of Physics of Ferrara University).

In the image 10 one can see the hysteresis loops as simulated for interacting and non-interacting Co/Py dots.

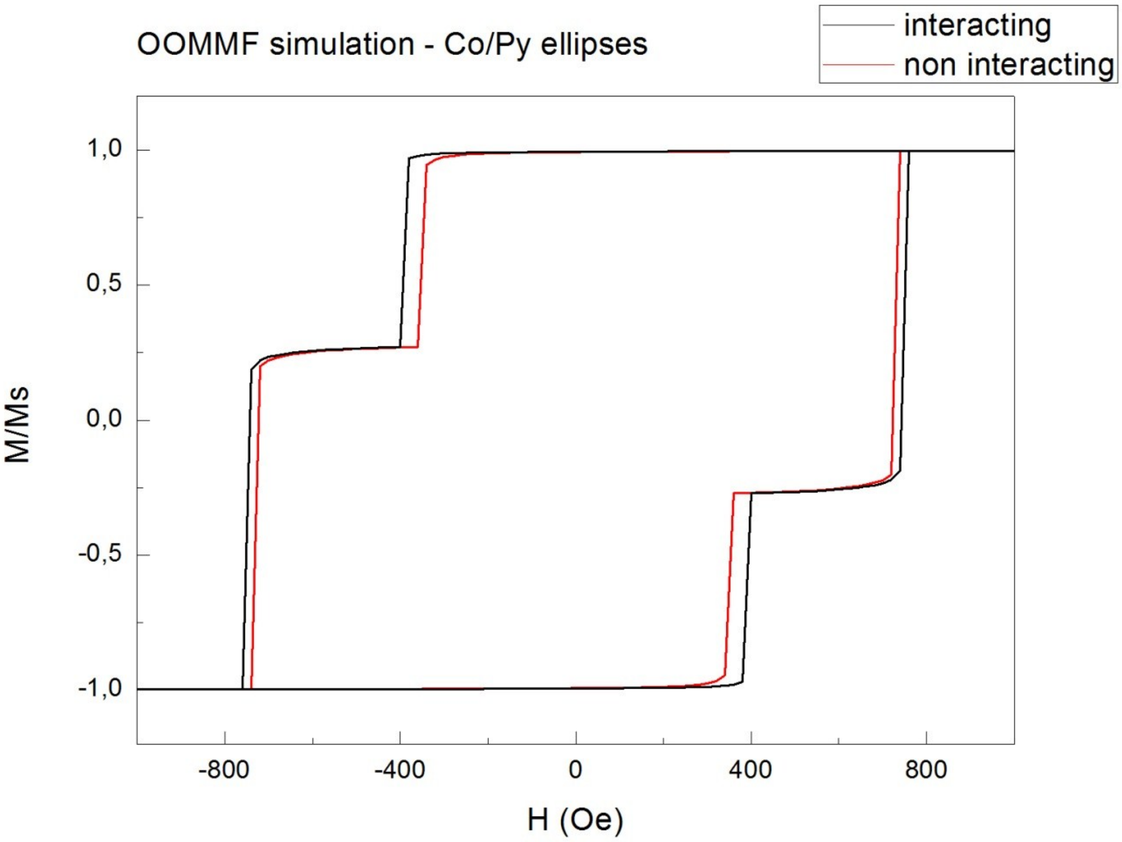

Figure 10: simulated hysteresis loops for interacting and non-interacting Co/Py dots

As often found in the comparison between simulated and experimental hysteresis loops (79) (80), the switching fields are not perfectly identical but, what is important to notice is that there is a shift toward higher value of the switching field following qualitatively the same behavior seen in the experimental case.

Another confirmation of this behavior comes from the measurements performed with MFM. In figure 11 we have done a comparison between interacting and non-interacting dots when an external field (in the range between the plateau and the saturation) is applied.

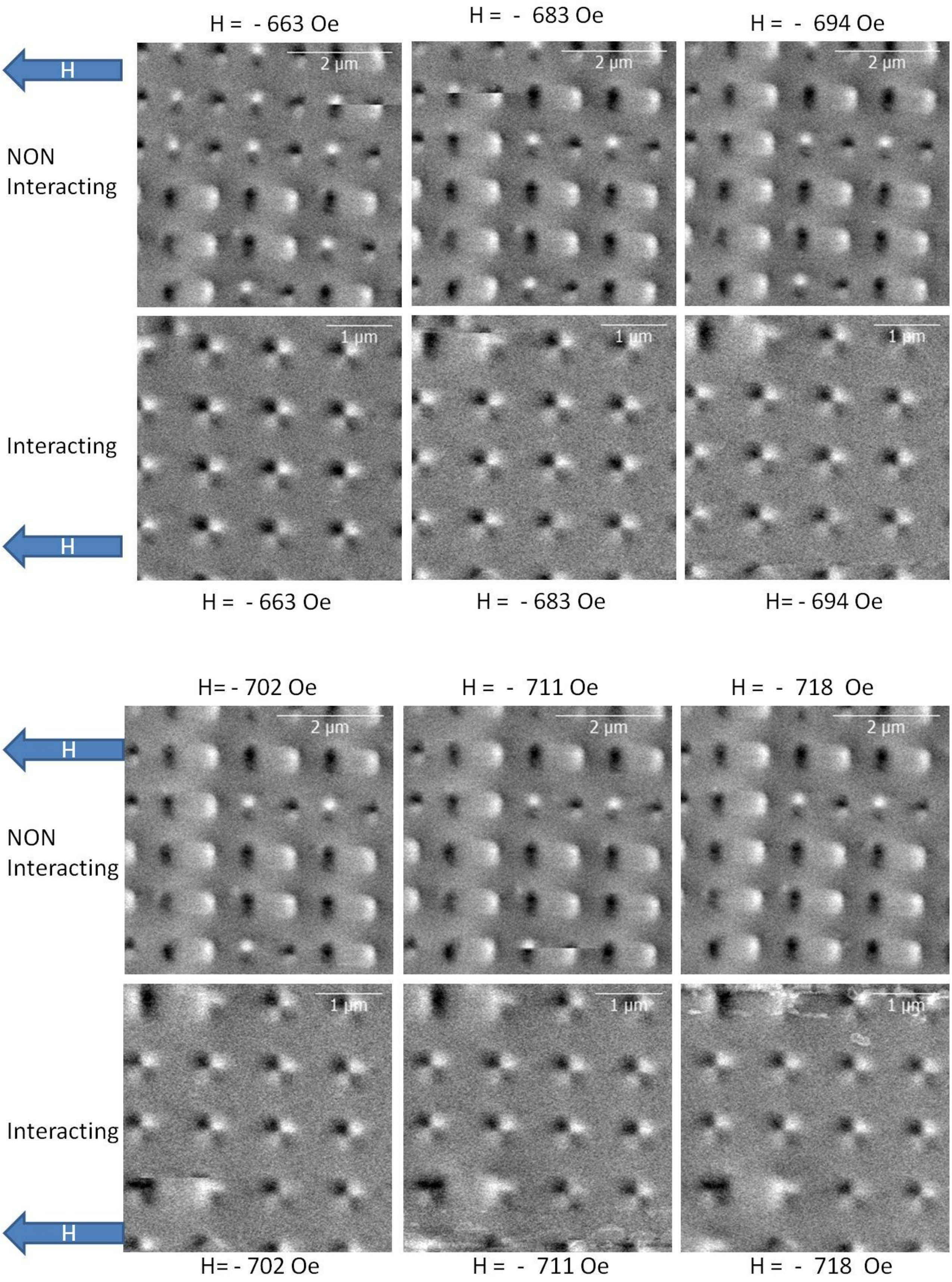

Figure 11: MFM comparison between interacting and non-interacting dots when an external field is applied in the range between the plateau and the saturation.

Looking at the comparison of the two different samples at -663 Oe: half of the non-interacting dots have switched both the Py and the Co along the field direction, instead the interacting particles are all still in the AP state.

Increasing the field we can see as the interacting particle inversion is always retarded. At -718 Oe almost all the non-interacting particles have passed to the Parallel state, instead the interacting particles are in the AP state.

The situation is completely reproducible also for the reversal of Py particle (first step of the hysteresis loop).

## Bicomponent Py/Ni

Now we present a system of patterned nanodots with shape and dimensions identical to the case above described but with one of the two particles of the bicomponent dot made of Nickel rather than Co. Nickel is a material magnetically softer ($Ms=490x10^3$ A/m) than the Py ($Ms=800x10^3$ A/m) which is in turn softer than Cobalt ($Ms=1300x10^3$ A/m) ; as we will see in the hysteresis loop along the easy direction (the long axis of the ellipses) there still are Parallel and Antiparallel (plateau) states due to the different switching field (and the stair shape of the loop is conserved also with the change of materials), but the Py keeps the place of Co in terms of switching order, while the Ni takes the place of Py.

### Non-Interacting Ni/Py dots

In the image below (Fig. 12) we report the hysteresis loop along the easy direction of the non-interacting Ni/Py obtained with L-MOKE. The loop shows two steps and the plateau: the Ni starts switching at about 100 Oe; when all the Ni dots completed their reversal the loop is in the plateau (or in the antiparallel state) that extends between 180 and 300 Oe. Finally when also the Py particles start switching the Magnetization grows until it reaches the saturation at about 400 Oe.

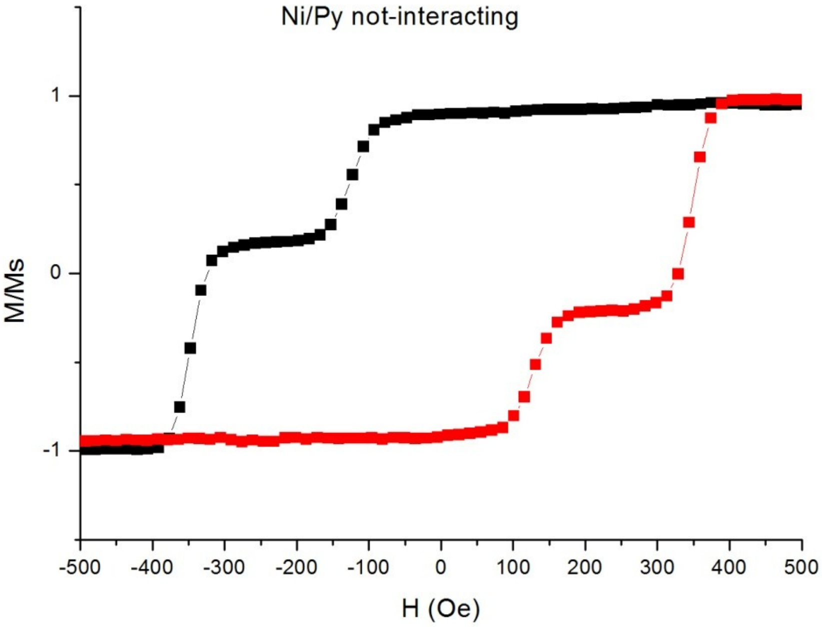

Figure 12: Hysteresis loop produced with L-MOKE along the easy direction for the non-interacting Ni/Py dot pattern.

We verified the Parallel – Antiparallel – Parallel transition, by the MFM in field measurements by the application of an increasing field along the easy direction after saturation of the sample in the opposite direction in a + 800 Oe field. See figure 13.

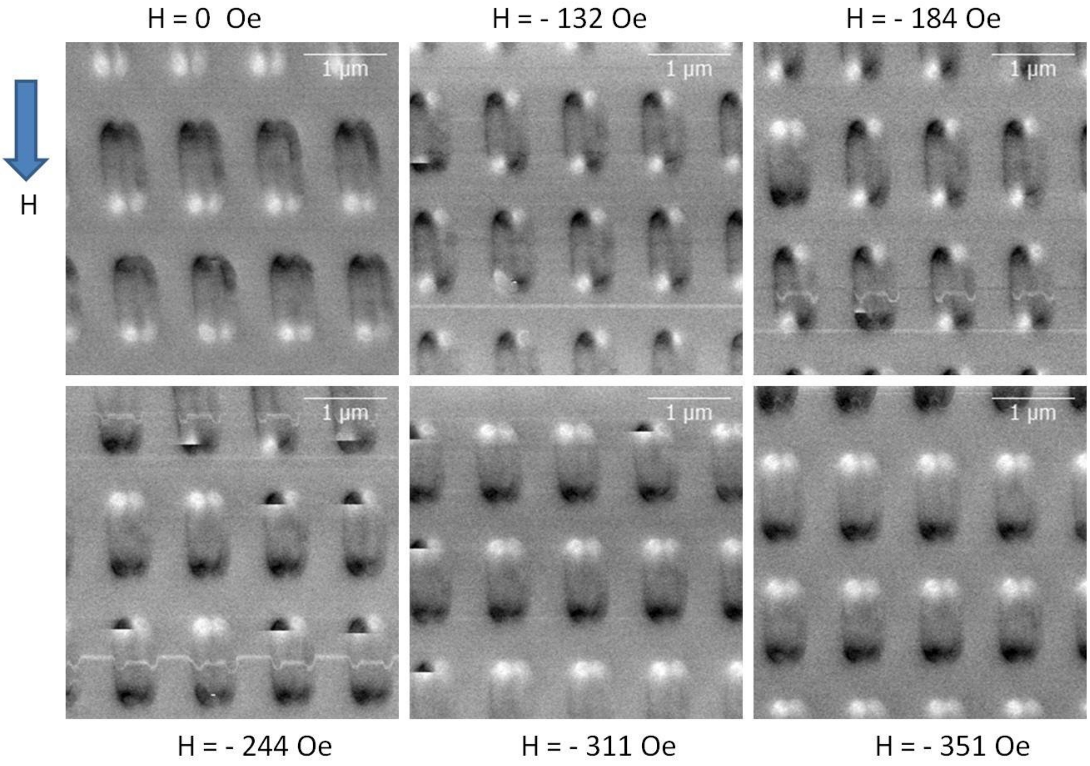

Figure 13: MFM images of the Non-Interacting Ni/Py taken at relevant fields.

The field at which the MFM contrast is completely reversed doesn’t coincide exactly with the reversal of the magnetization measured with MOKE: this is due to the known anticipatory interaction of the magnetic tip on the magnetic dots (81) (82). Nevertheless the transition P-AP-P is confirmed.

## Interacting Ni/Py dots

We have performed the same measurements also in the case of the interacting particles in the same configuration (head to tail) and the hysteresis loop is reported in fig. 14

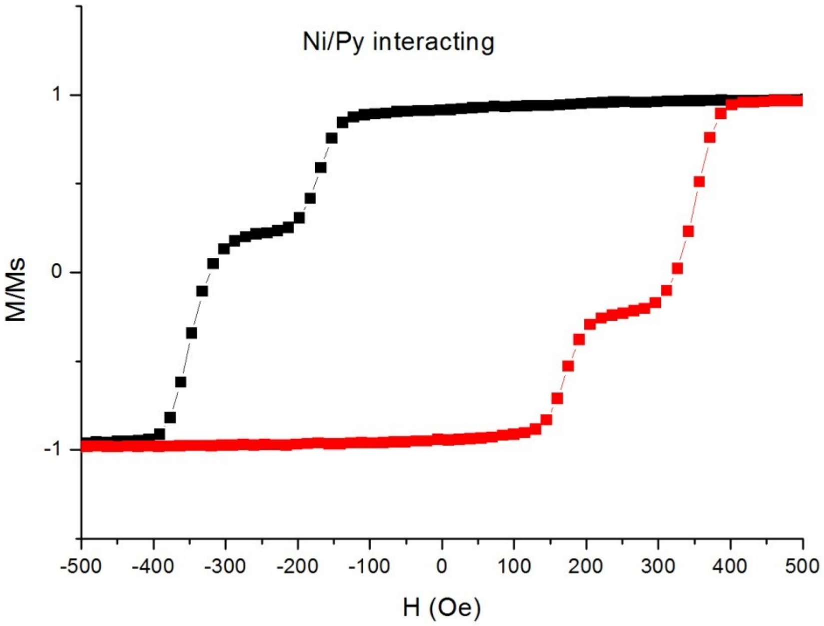

Fig 14: Hysteresis loop produced with L-MOKE along the easy direction for the interacting Ni/Py dot pattern.

MFM images give the confirmation of the P-AP-P steps (not shown here).

## Comparison between interacting and non-interacting Ni/Py particles,

Finally we performed a comparison between interacting and non-interacting particles and report the relative hysteresis loops in the figure 15.

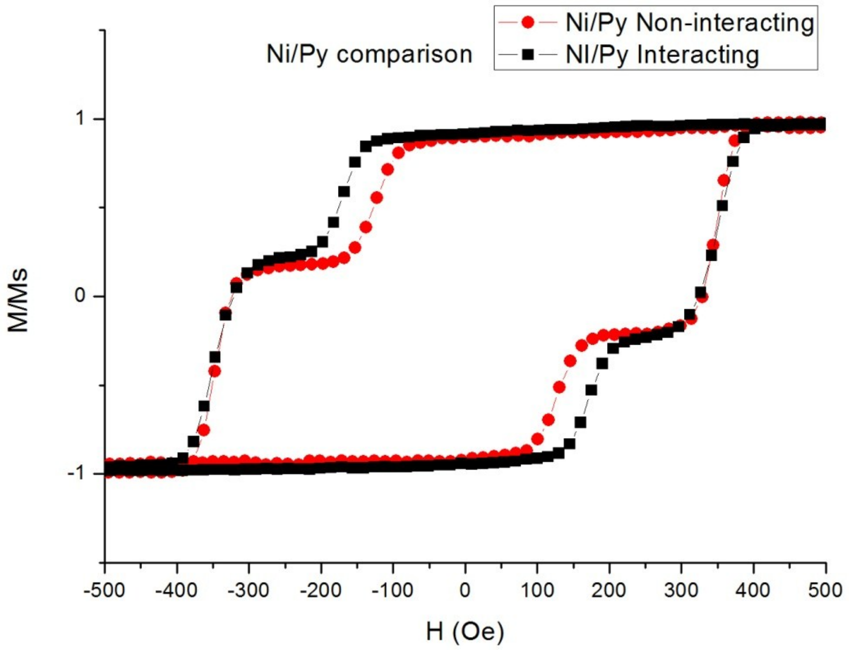

Figure 15: hysteresis loops corresponding to the patterns; the red continuous line represents the cycle for the non-interacting dots, the black continuous line the cycle of the interacting dots. The regions of Py inversion overlap, differently from what happened in the previous cases.

The graph explicitly confirms the shift of the Ni reversal from lower to higher fields when we pass from the non-interacting to the interacting case. As for the Co/Py comparison we could affirm that this behavior is due to the head-to-tail interaction that tends to keep the Nickel particles magnetization aligned, or equivalently, the configurational anisotropy (due to the reciprocal position of the dots in the array) would see the magnetization of Non-Interacting Nickel particles in the preferred direction easier to achieve.

As done in the previous case of Co/Py we performed a simulation with OOMMF (figure 16) and obtained the following result in which the comparison of interacting and Non-Interacting Nickel/Permalloy dots is reported. The behavior is very similar to the experimental case in particular we notice that there is not a difference in the Py reversal field (exactly as happened in the MOKE cycle), the reason is not well known but it is a topic of present research.

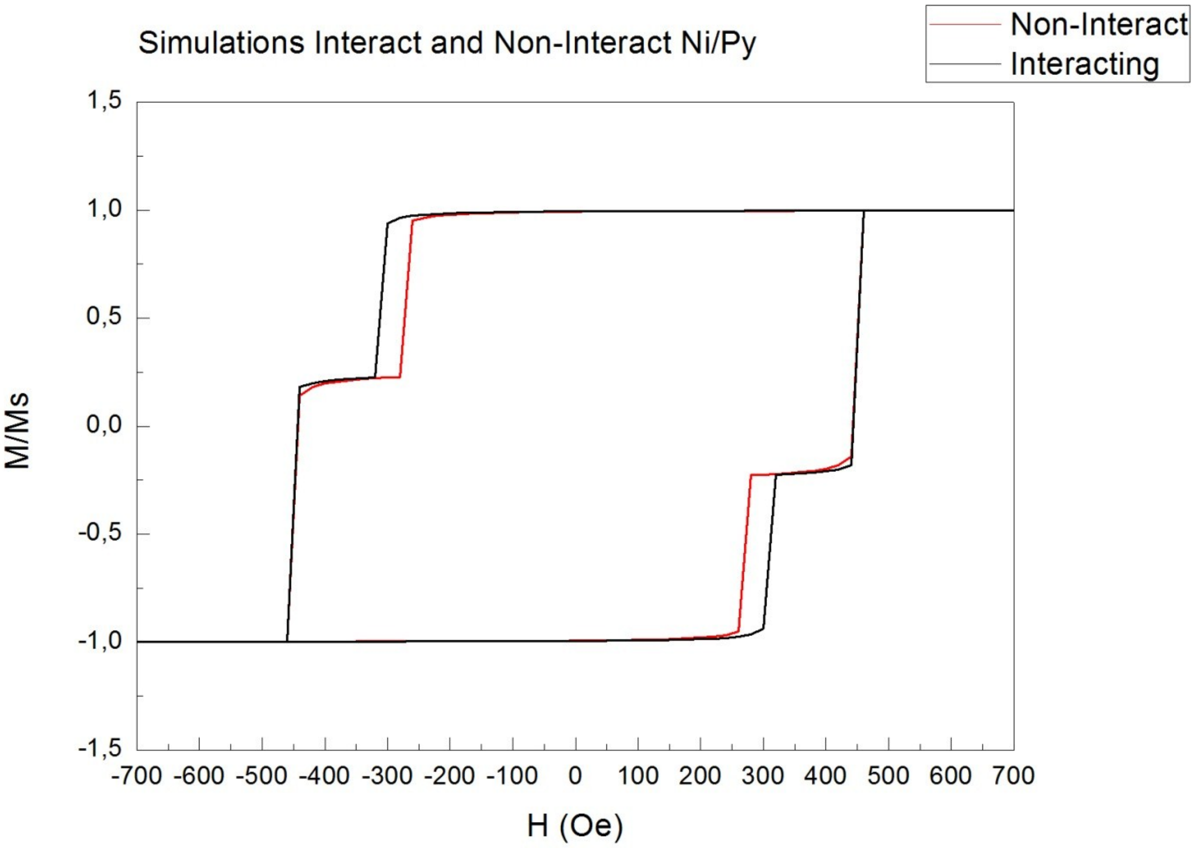

Figure 16: Hysteresis loops obtained with Micromagnetic Simulations with OOMMF. The red curve is relative to the non-interacting dots, the black curve to the interacting dot. The behavior is compatible with the measured cycles.

## Conclusions

In this section we presented the study of different combinations of the same dot shape in different configurations and materials. The studied dots were constituted by two ellipses made by different magnetic material and placed side by side along the easy magnetic direction; we studied the different cases in which two dots were far (along the easy direction) enough so that they didn't interact and the case in which they were placed at a distance of 140 nm and magnetically interacting. We also studied what happens when one of the two materials is changed and substituted with a softer magnetic material (i.e. Nickel instead of Cobalt) and leaving the Permalloy constituting the other ellipse of the dot.

The change of reciprocal distance of the dot inside an array changes the width of the hysteresis loop, in particular the interaction between the dots along the easy direction enlarges the loop due to the increasing of the switching field in the reversal mechanism. Nevertheless it doesn’t alter its shape.

The substitution of Co with Ni transforms the Py in the harder material and the loop preserves the “stair shape” but with the switching field of Ni less than Py (that switchs after).

The MFM measurement confirmed the behavior seen with MOKE loops and allows to directly observe the three different states: Parallel, Antiparallel and again Parallel that was inferred by the analysis of hysteresis cycles.

Finally we performed a comparison of loops calculated with the simulator OOMMF and experimental measurements finding the same behavior. In particular there is an overlap hysteresis loops corresponding to the switching fields of Permalloy in the Ni/Py dots in the interacting and non-interacting cases that emerges either in the measured and in the simulated loops: this is in contrast with the widening of the loop expected for interacting particles that is present in all the other cases and this is a topic of present research.

# Finite Arrays of Py Disks: Global Configurational Anisotropy

## Introduction

In the previous chapters we analyzed samples with different magnetic properties and we classified the magnetic anisotropies characterizing them. In particular in the last chapter we introduced the Configurational Anisotropy deriving from different interactions due to the relative positions of nanoparticles in a periodic array. Here we would extend those principles to the case of a squared array with interacting particles but with an extension that is finite, that is, when the size of the array is not large when compared with the periodicity of the composing dots. The behavior is that the particles in the array are affected by a demagnetizing field which is different in each spatial position and the switching process is not uniform on the entire array: we called this effect “Global Configurational Anisotropy”.

In this chapter we will analyze with MFM and MOKE finite squared arrays of circular magnetic dots and perform simulations with MuMax, a GPU-based software (83). We will show as for limited size of the periodic arrays the transition of the magnetization during the reversal process starts at the borders and the corners of the array and propagates inside the array so that at every applied field the magnetization results to be not uniformly distributed.

While the shape of the dots (circular, elliptical, etc.) introduces a *Configurational Anisotropy*, (84), (85), (86) we find that the finite array dimensions introduces an additional *Global Configurational Anisotropy* (87). Both effects originate at the demagnetizing interactions playing at different space scales: the dot and total sample space scale, respectively.

Simulations of dot arrays are often restricted to one dot assuming isolated non-interacting magnetization processes, e.g., when studying reversal processes. (88) (89) (90) (91). Periodic boundary conditions are often used to incorporate interdot interactions, still limiting computations to a restricted number of dots and assuming infinite lattice periodicity (92), (93), (94), (95). Then, configurational anisotropy is accounted for, but global configurational anisotropy is not. In this section, we show that mutual dot interactions together with finite array dimensions have a non-negligible impact on the magnetization reversal of a dot array. We numerically and experimentally study the hysteresis properties of a Permalloy (Py) array of 16x16 circular and elliptical dots. In magneto-optical Kerr effect (MOKE) measurements, in-field magnetic force microscope (MFM) measurements and simulations, we find that global shape anisotropy steers the magnetization reversal of the array: the dots run through different magnetization states depending on the dot location and sample properties and collective magnetization processes occur, leading to transition avalanches and formation of magnetization chains. Moreover, we find that external perturbations as the MFM measurement itself anticipate the dots reversal path set by the global configurational anisotropy and promote field induced magnetization state changes.

## Samples Fabrication

The arrays were fabricated (by prof. Paolo Vavassori group at CiC Nanogune in San Sebastian, Spain) on Si (100) chip of 10 × 10 mm$^2$ by electron beam lithography processing. The desired pattern is drawn with the electron beam on electron sensitive resist layers previously coated on Si (100) substrate. The electron sensitive resists we have used are double layered Poly(methyl methacrylate) (DL PMMA) where the bottom and top layers are PMMA 450 K A4 with a thickness of 200 nm and PMMA 950 K A2 with thickness of 50 nm, respectively. To perform electron beam lithography a RAITH 150$^{\mathrm{TWO}}$ tool was employed. The patterns on the DL-PMMA were generated using an acceleration voltage of 10 kV, 10 µm aperture, and a measured current of 15 pA. Subsequent to developing the generated patterns, a Permalloy layer was deposited at a rate of 0.8 Å/s onto the electron-beam lithography structured sample using an electron-beam evaporator, while rotating the sample at 15 rpm to obtain a homogeneous distribution of the magnetic material with a thickness of about 15 nm. Finally, the DL-PMMA was removed in a lift-off process, leaving the desired arrays of Permalloy disks on the silicon substrate.

We fabricated samples with two different dots shape: circular and elliptical. For each shape we chose different lateral dimensions, distances and thickness, as we will describe with more detail in the relative section.

## Circular Dot Arrays

We produced three series of squared 16x16 arrays of circular dots with the same periodicity of 400 nm and with different diameter, respectively: 350, 315 and 280 nm, that hereafter we can call simply: large, medium and small particles. We report the SEM micrographs of the samples in fig. 1

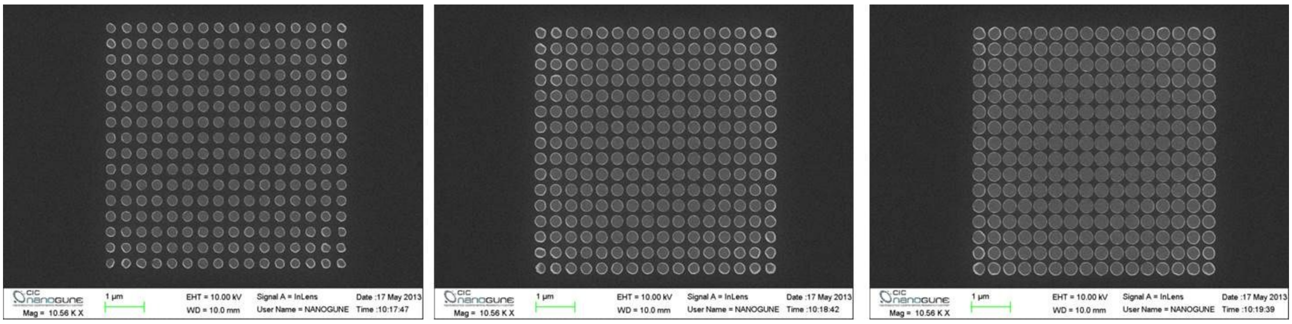

Figure 1: SEM micrographs of the three geometries of circular dot array: from the left small, medium and large disks.

## Medium Size Disks

### MFM and MOKE analysis

We start describing the medium size disk array: a 16x16 array composed of circular dots with a period of 400 nm, a diameter 315 nm and thus an interdot separation of 85 nm along the x and y direction and about 250 nm along the diagonal. We estimated an average thickness of about 13.5 ± 1.5 nm making use of the profile extracted with AFM topography.

The reason why we start describing the medium size dot array is that we have performed a complete characterization, both with experiments and simulations and it is a good reference to make the comparison when we will describe the other samples.

In the image 2 we report the MFM measurements of the reversal mechanism. They are obtained by the following procedure: we apply a magnetic field to saturate the sample along the y direction (as indicated with the blue arrow) then the field is reduced to a certain value and the MFM image is performed and saved. After this, the field is reduced to a lower value and the MFM measurement is done; so on for every indicated field.

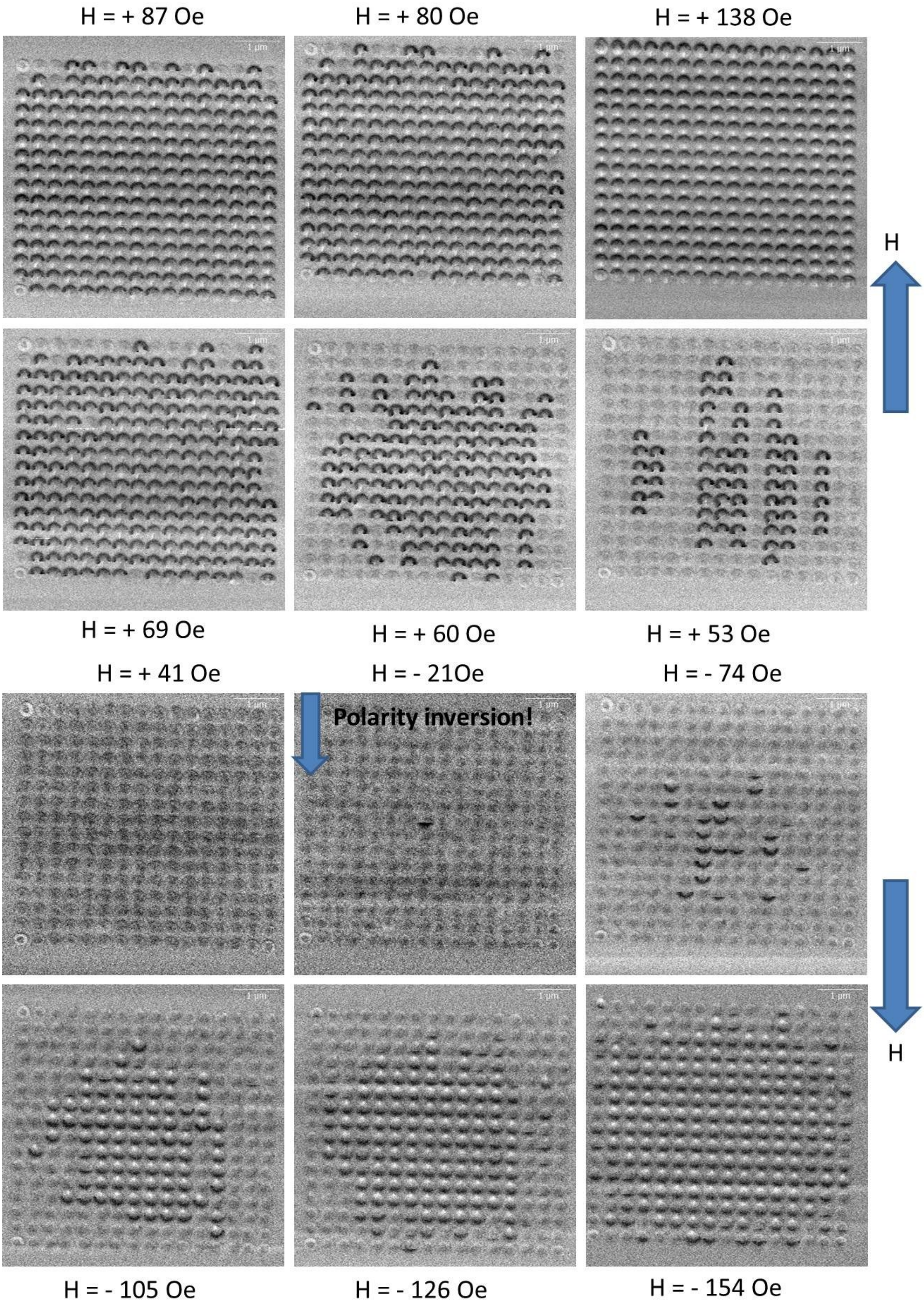

Figure 2: MFM measurements

When the field is reduced to +138 Oe all the particles are in the so called Single Domain (SD) state, in fact we see that in each particle the black and white contrast is the same, black in the upper part and white in the lower. When the field is decreased to +87 Oe something, not trivial, begins to happen. Some particles at the borders, in particular at the corners, are no more in the SD magnetization state but the grey contrast suggests that particles are in the vortex state: due to the absence of strong stray field, and the presence of a black point in the center of the disk where the magnetization has a "topological singularity" and comes up with postie (black) value. The reason why there is a position dependent switching field is linked to the global interdot interaction: the dots at the center of the array are influenced by the stray field of all the surrounding particles, and this influence is different at the corners of the array where the spatial symmetry is broken. This is the reason why we called this effect "Global Configurational Ansisotropy", due to the fact that the magnetization reversal is determined by the finite-size essence of the array.

The particles in the center of the array are influenced by the stray field of the particles above and below, all in the Single Domain state (the particles at right and left are in SD state but for geometrical reasons the interaction is greater along y). Differently a particle in a corner is influenced by only one particle along the y direction. Due to the fact that particles are magnetized along the y direction we can define (for brevity) the interaction along this direction as "head to tail" interaction. Moreover there is also the dipolar coupling with the particle placed on the array diagonal.

In the following image (figure 3) we want to describe the dipolar interaction of a particle in the center, at the lateral boarder and in the corner.

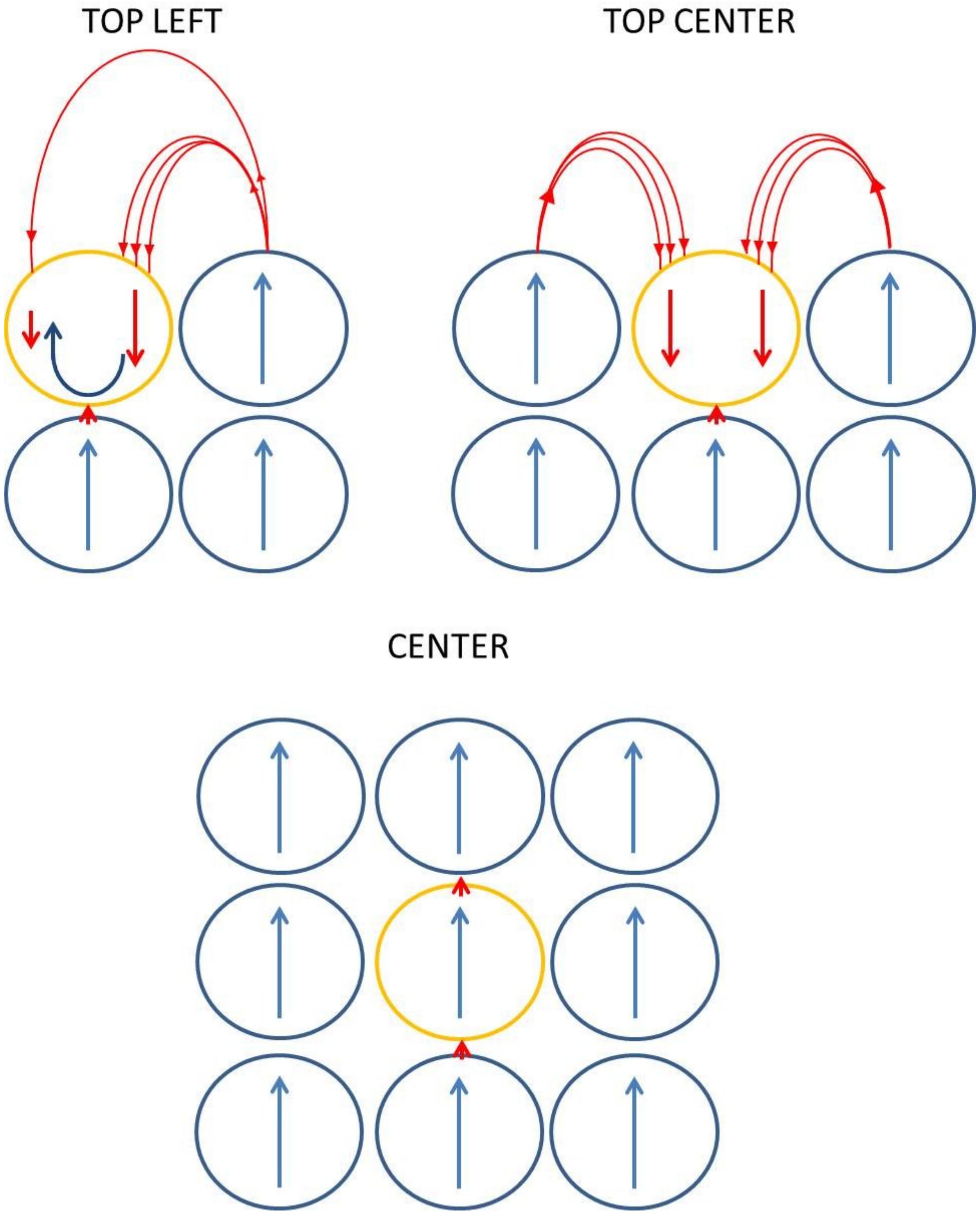

Figure 3: dipolar coupling between the dot in the array. With red arrows we represented stray-field lines. Blue arrows correspond to the magnetization of the dot.

At the corner the disk feels the stray field prevalently of three surrounding particles. The dot below favors the magnetization in the same direction; in fact the head to tail coupling works to maintain the single domain configuration. It is very important to keep in mind that, due to the fact that the sample is magnetized along y, le flux lines exit and enter from the top and the bottom of each particle and there the density of the flux lines has its maximum. The interaction along y is thus sharply stronger than the interaction along x. We could say that along y the dipolar coupling is of the first order, while it is of the second order along x. The particle at its right produces a dipolar interaction that tends to demagnetize it, as sketched in the image 3 (top left): the flux lines of the stray field have decreasing density as the distance increases, so the stray field of the right particle on the left particle has a different intensity in different disk area positions. It is possible to show that the diagonal particle, with a lower intensity (let’s say, third order dipolar coupling), has the same influence. This means that there is a net clockwise torque acting on the top left particle which favors a vortex with a preferential chirality.

The global asymmetrical behavior seen with MFM is not explained until we don’t consider which is the difference between the particles in the corners, in the top center and in the center.

The influence of the surrounding particles on the top center one, is sketched in the figure 3 too. The greater effect is due to the particle below it, which tends to maintain the single domain magnetization; conversely the particles on the right and on the left “try” to demagnetize it, but with the same intensity. So there is not a net torque on the top center dot but only a strong demagnetizing field. This is the reason why the switching field from Single Domain to Vortex is greater in the corner than in any other place of the array.

Finally, to complete the analysis we comment the interactions in the center: it is clear that there are two first order interactions along y, and both favor the maintaining of the single domain state on the center dot and in general this is valid for all the particles which interact along y with two dots uniformly magnetized; this explains why in the core of the array the SD is more stable.

When the field is lowered again the switching mechanism (from SD to Vortex) propagates to the inner particles of the array.

When the vortex is formed the stray field emerging from the particle is largely reduced: as discussed in the first chapter, the vortex state is the configuration that minimizes the density of free poles on the lateral surface, therefore, the stray field reaches a minimum. The switching mechanism is guided by the particles that are still in the SD state and as said, prevalently along the y direction. The formation of chains along the y direction is so explained: once one particle has switched to vortex state, the nearest neighbor along the y axis lacks of the stray field sustaining the Single Domain and along the x axis the other particles work against the SD maintaining.

At +41 Oe all the particles are in the vortex state, also with a relative uncertainty all with the same polarity: the particles have a black point in the center representing an outwards magnetization but it is not always visible. Moreover is shown that when the interdot separation is sufficiently small (compared with the dot dimension) the chirality of the vortex along a switching chain is congruent (15).

The vortex state is an equilibrium state for the circular particle for a given range of thickness and diameter and a certain amount of energy is needed to expel the vortex core and establish again the Single Domain state with opposite magnetization sign. For this reason when an increasing negative field (opposite in-plane direction) is applied, the switching field is not symmetric.

The switching order instead is symmetric, in the sense that the vortex expulsion and the Single Domain state formation follow the preceding symmetry: the Single Domain is favored in the center and from the center the switching begins propagating towards the outer part of the array until reaching the corners. The transition from the vortex to the SD state is about specular to the vortex nucleation, apart from the field values.

The explanation is not simple, for the complexity of the vortex expulsion mechanism, but we could imagine that when an external field is applied each dot (even in the vortex state) gains a net magnetic polarization along the external field direction. The dipolar interactions along y (head to tail) sum and enforce so that the center is the array position where the expulsion is more favored. In the external position (in particular in the corners) the head to tail interaction is minimized.

In a real sample the dimensions of the dots, their distance and thickness are not perfectly constant due to the imperfections in the production of each dot of the array. It is meaningful to notice that despite the inevitable discrepancy of the real sample shape with respect to the theoretical one the overall behavior is not chaotic but follows a well arranged distribution.

The asymmetry in the reversal mechanism is confirmed also with MOKE. We report in figure 4 the hysteresis loop produced with MOKE based on an optical wide-field polarization microscope optimized for Kerr microscopy (Evico Gmbh) (96).

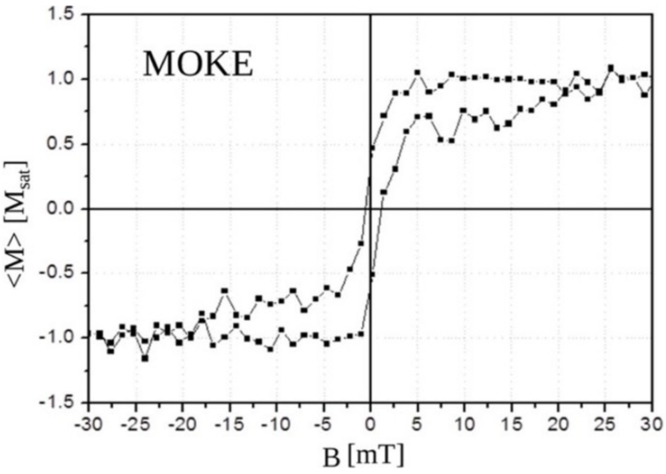

Figure 4: Hysteresis loop produced by MOKE microscopy.

In the descending branch (coming from positive field) we observe that the magnetization along the applied field starts to decrease rapidly at about 2,5 mT (25 Oe). At a zero applied field there is a non-zero remanence, but going versus negative field the coercive field is very low (a few Oersteds). The negative part of the descending branch is not perfectly symmetric compared with the positive: there is a “tail” in the M vs H curve meaning that the magnetization is somehow stable in the remanent (or coercive) distribution. In fact from the above, the vortex is a stable state for the disk with these dimensions and its expulsion needs energy. The tail in the hysteresis branch represents the difficulty of the vortexes expulsion during the reversal process.

Notice that there is not a perfect quantitative agreement with the MFM measurement. We explained the incoherence considering that in the MFM measurements there is always an interaction between the magnetized tip and the magnetization of the sample and this could anticipate the transition from the Single Domain to the vortex state and viceversa (81) (82).

### Micromagnetic Simulations

Simulations are performed using MuMax considering in-plane sample dimensions identical to the fabricated sample. The thickness is varied between 10 nm and 15 nm. Simulations of descending hysteresis branches reproduce the MOKE and MFM experiments by starting from saturation and reducing the applied field with steps of 1mT (10 Oe). After every field jump, the magnetization processes are computed for 50 ns. A high damping $\alpha=1$ ensures that the system is in equilibrium after this time span. Cells of 3.125nm × 3.125 nm$^2$ are used to discretize the sample (2048 × 2048 cells). A saturation magnetization $M_{sat}=740 \times 10^3$A/m, exchange stiffness $A = 1.2 \times 10^{-11}$ J/m, and zero anisotropy is considered.

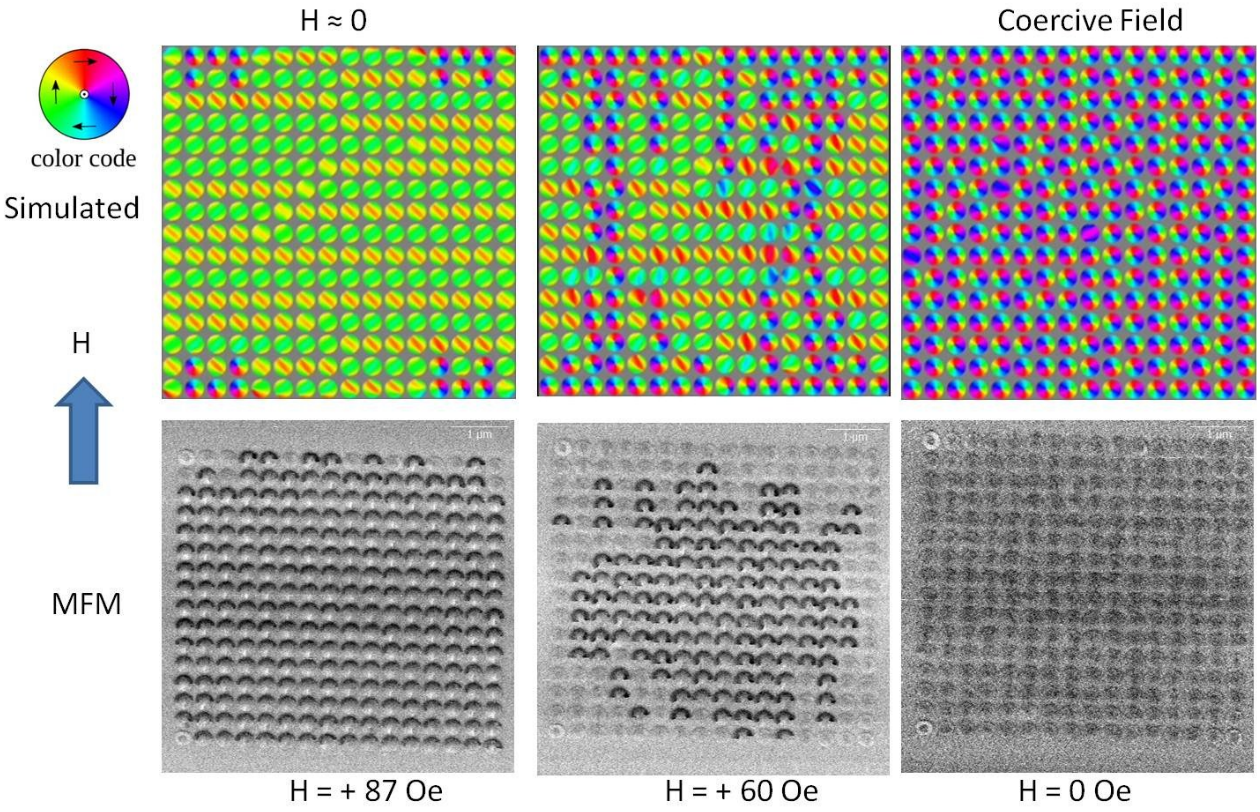

Figure 5: comparison between simulations and MFM measurements at three different fields.

In figure 5 we made a comparison between simulation and MFM measurements at external fields for which the reversal progress is comparable: in the first (left) the switching mechanism has just begun, in the second (center) a 35-40% of the particles has switched and the remaining is still in the SD state; in the third image all the particle are in the vortex state.

As in the case of MOKE the switching fields do not quantitatively overlap, due to the already explained anticipatory effect of the magnetic tip on the sample. Nevertheless it is noteworthy that also in the simulations the space-dependent switching to the vortex state qualitatively match with the MFM measurements. Our simulation method, which allows taking into account the reversal for the entire array (without applying periodic boundary conditions) takes into account the Global Configurational Anisotropy due to the finite size dimensions of the array.

The comparison with MOKE evidences a qualitative and quantitative agreement: see figure 6 which reports the descending hysteresis branch obtained with the simulation for three different thicknesses.

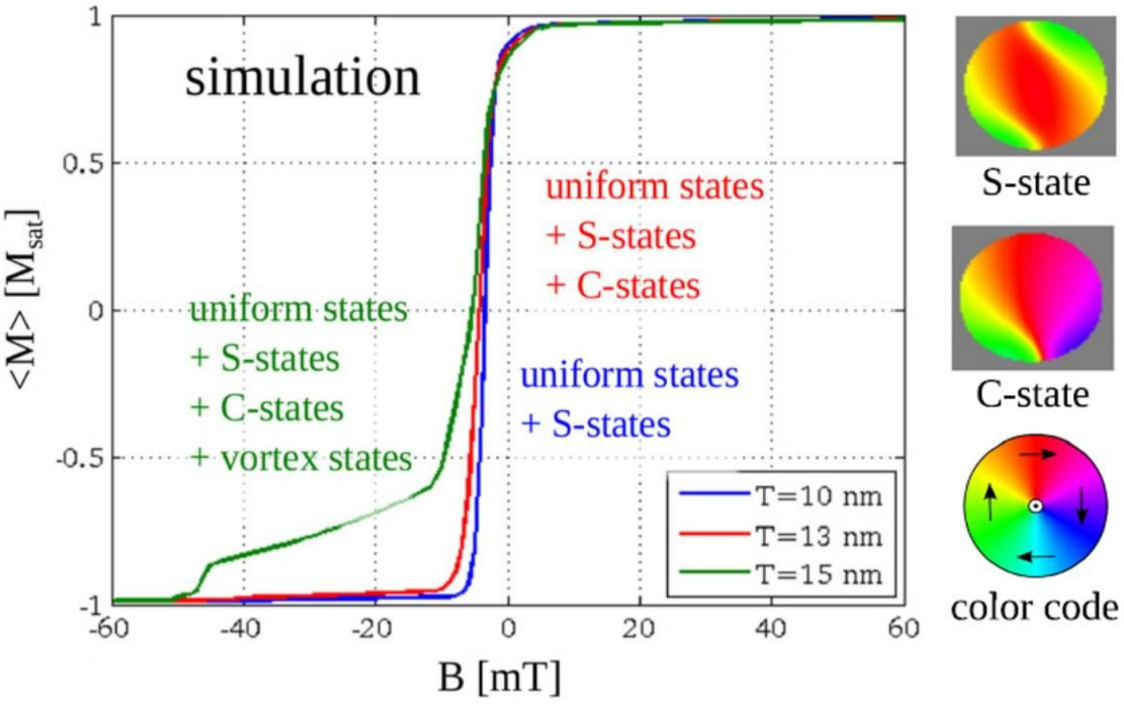

Figure 4.6: calculated descending hysteresis branch for three different thicknesses

For a thickness of about 15 nm (green line) the shape of the hysteresis loop is the same seen with MOKE. Simulations results evidenced that the chosen thickness represent (theoretically) a threshold thickness. Below this value vortex states are not formed and only configuration magnetization called “C and S states” are stable during the reversal.

## MFM analysis on different arrays

In Figure 7 we report the MFM measurements performed on an array having circular dots with a lower diameter and a greater interdot distance (being the period always the same) respectively D=280 and s=120 nm.

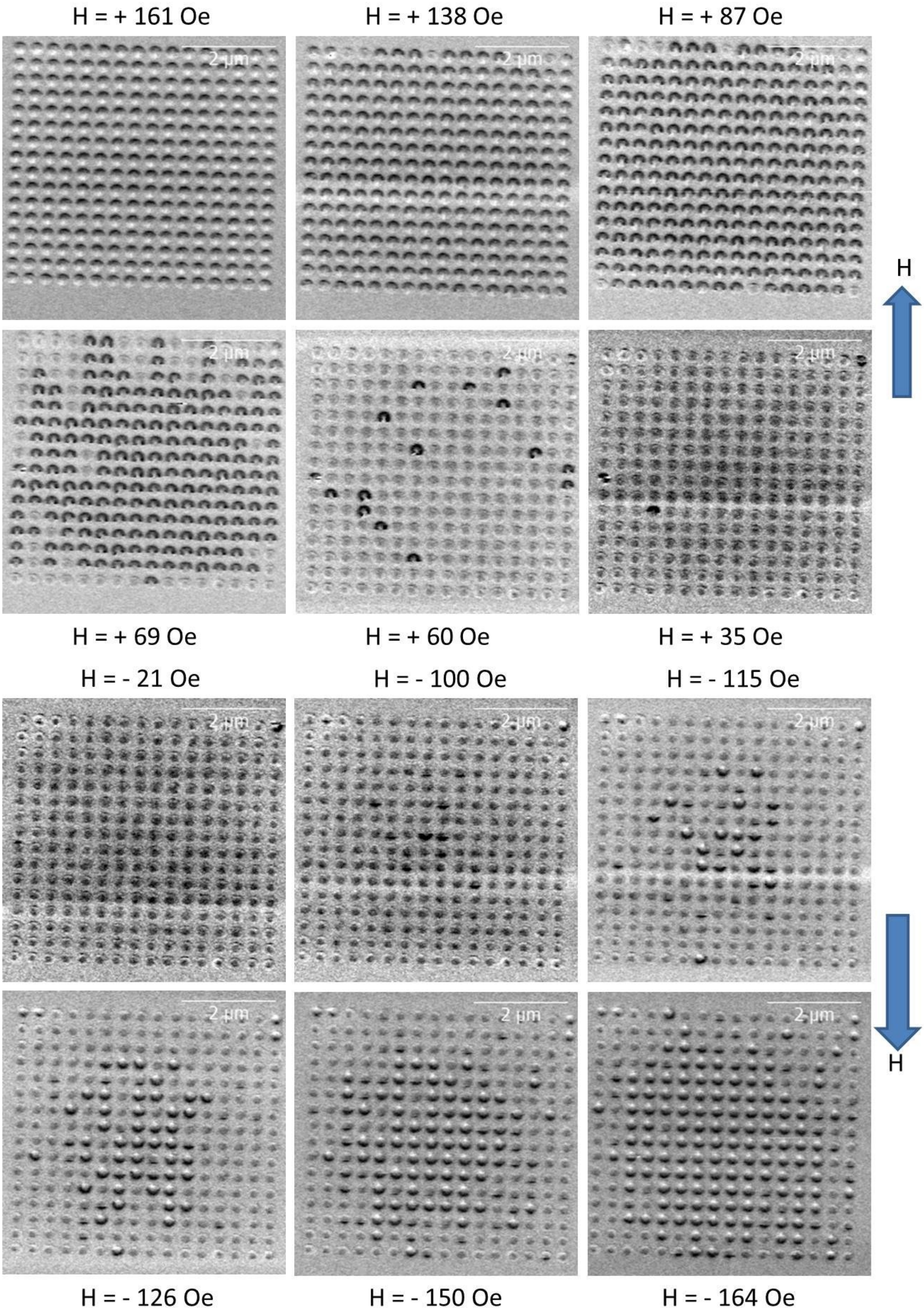

Figure 7: MFM measurements for small circular dots array.

As one can observe the reversal behavior is totally similar to that seen in the previous sample (the GCA acts to give an asymmetric progress of the vortex nucleation over the array) but the switching fields are noticeably different: the transition from SD to vortex state is reached at greater field values (at +138 Oe the particles in the corner have already changed their state) and symmetrically the transition from vortex to SD is further shifted to higher negative fields. We can say that in this geometrical layout the vortex state is favored with respect to the previous sample.

We can argue that this behavior is prevalently due to the greater interdot separation: we explained that the proximity of the dots favors the SD state due to the dipolar interaction “head to tail”; it is clear that if the interdot separation increases (and this is the case) the SD state is less favored and the Vortex state is energetically more stable.

The reduced diameter for a single particle would favor the SD state (as it is well explained in reference (97)), hence the field range of vortex existence should be reduced, contrary to what actually happens: this is another proof of the fact that the dipolar interaction along y has a considerable importance in the formation of the vortexes during the reversal mechanism.

Following the just described process it is reasonable to expect that when the interdot separation decreases, the vortex state is less favored. In the image 8 we present the MFM measurement of the reversal for the large particles array (Diameter=350 nm, separation=50 nm).

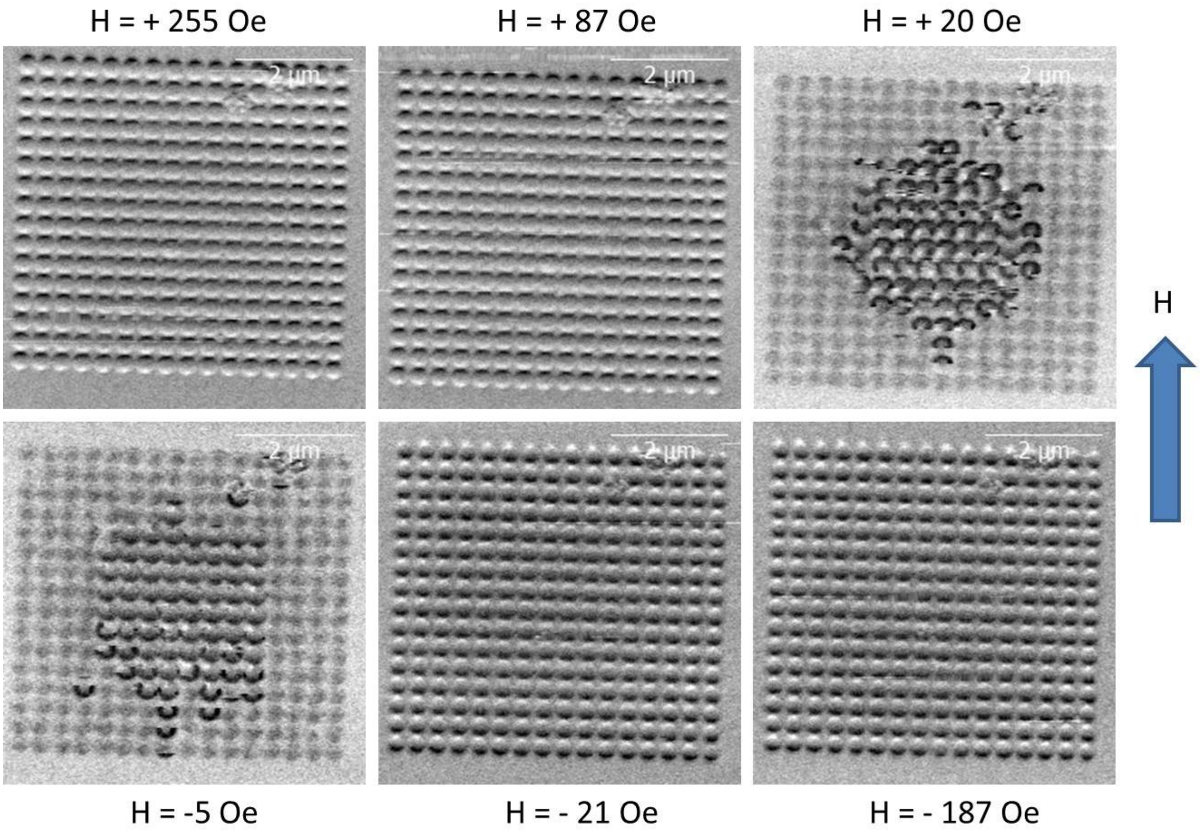

Figure 8: reversal mechanism measured with MFM for the large particle array.

In fact, despite a greater diameter (in a single non-interacting particle) would favor the Vortex State, the dipolar interaction prevails and reduces considerably the stability of the vortex state. Notice that in this case there is not a field under which the array is uniformly in the vortex state and also at remanence the core particles remain in Single Domain.

Finally, we see the effect of the thickness increase. In figure 9 we report the MFM images of the reversal for an array with 16x16 circular dots with medium diameter but with a thickness of 18 ± 1,5 nm. It has substantially a pattern identical to the first sample described but with a greater particles thickness.

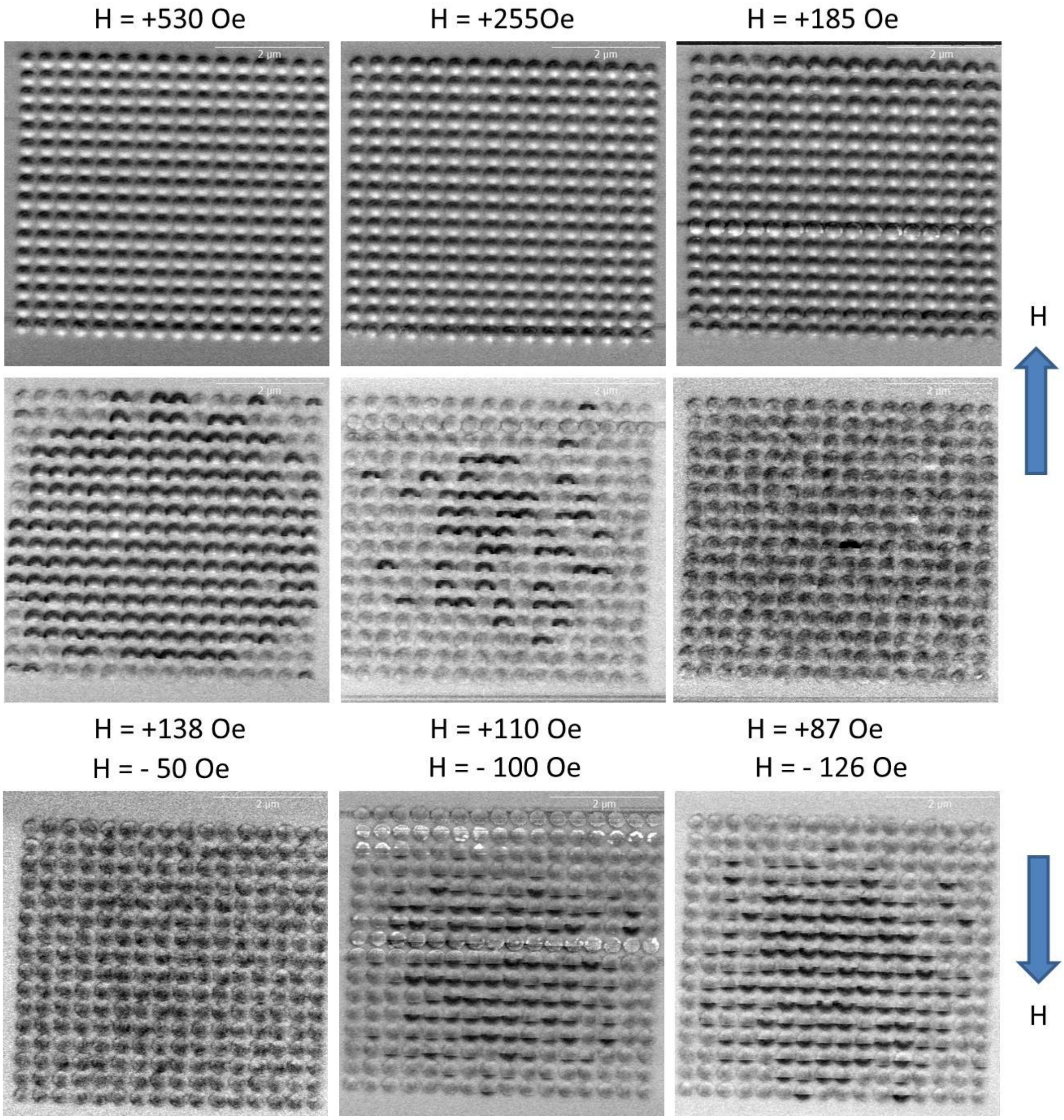

Figure 9: MFM images of the reversal for medium size particle with an increased thickness

One sees immediately that for increased thickness (equal diameter and period) the vortex nucleation is more favored and this is in good agreement with what occurs for circular non-interacting particle (97).

## Micromagnetic simulations on different arrays

We have seen that for a single circular dot the increase of the diameter and thickness brings to a stability of the vortex state and consequently to the enlargement of the field range of existence of the vortexes (97). We have proved experimentally that when the dots are put in an array and they magnetically interact, the reduction of the distance increases the strenght interaction and for this reason, when the array is magnetized by an external field, the interactions among particles will favor the Single Domain State reducing the stability of Vortex and therefore reducing the field range of existence of the vortex itself.

We performed a series of simulations in which we changed both the thickness and the diameter, keeping the period of the unit cell of the array constant, as done in the experiment described above. We saw that simulation confirms the importance of interaction among the particles inside the squared array in the determination of the vortex formation.

In the figures 10 and 11 we report a scheme which synthetically resumes the physical content of the analysis, reporting, for each simulation, only two representative frames at given fields (at remanence and at 10 mT) of the hysteresis loop.

From left to right we have an increasing thickness and from top to bottom the diameter increases.

We see that at remanence (figure 10) some samples show vortex state and some other are in the SD state (or hybrid C and S state). Let's consider for example the diameter 280 nm, close to the experimental one: we see that for increasing thickness the vortex nucleation is favored as we already know to be the predicted behavior. We find that for thicker arrays at the borders the particles are in the Vortex state in an greater amount than in the thinner arrays.

Now let's consider (for a given thickness, for example: 20 nm) how the vortex formation is affected by the diameter (with no change of the periodicity of the unit cell). Here the situation is more complex: under the diameter 240 nm the vortex is not yet formed (or it could not nucleate).

Above 240 nm the simulation result is clear: as the diameter increases the vortex formation is favored until a certain value at which the increase starts to disadvantage the vortex nucleation, due to the interaction between the particles which makes the vortex less stable. Globally this confirms what we experimentally observed: the dipole interactions of the circular particles in the array strongly affect the vortex nucleation and (contrary to what happens for the single non-interacting particle) to an increase of the diameter corresponds an instability of the vortex state.

Figure 11 shows the same arrays at a different external field value: 10 mT. For the thicknesses 10 and 12 nm and for smallest and largest diameters the magnetization switches directly from positive to negative single domain. This is another confirmation of what seen experimentally: above a certain diameter the interaction among the adjacent particles is very strong and the field range existence of the vortex is narrower than it would be for the single particle with the same diameter.

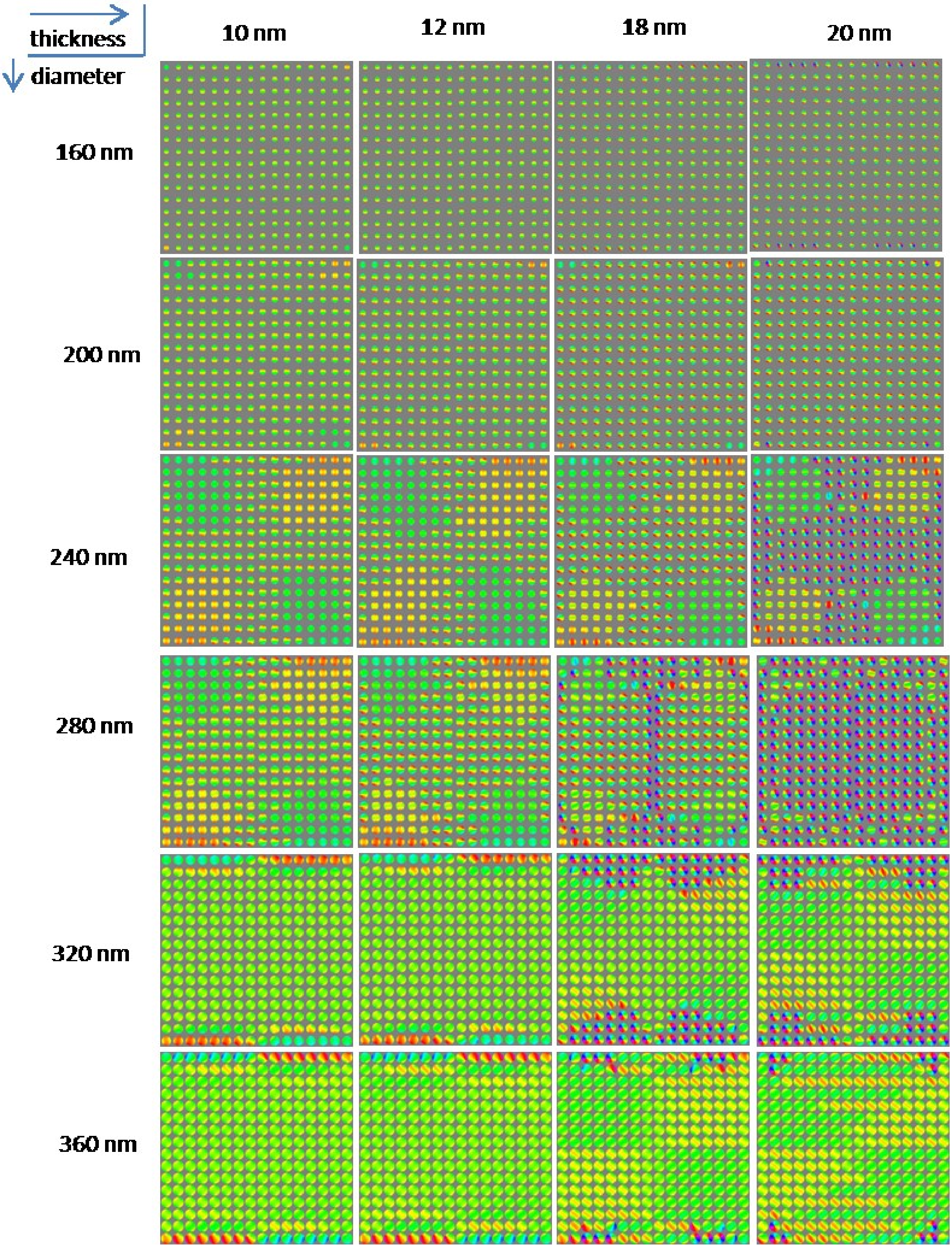

Figure 10: magnetization distribution for squared array of 16x16 dots with different dimensions at remanence

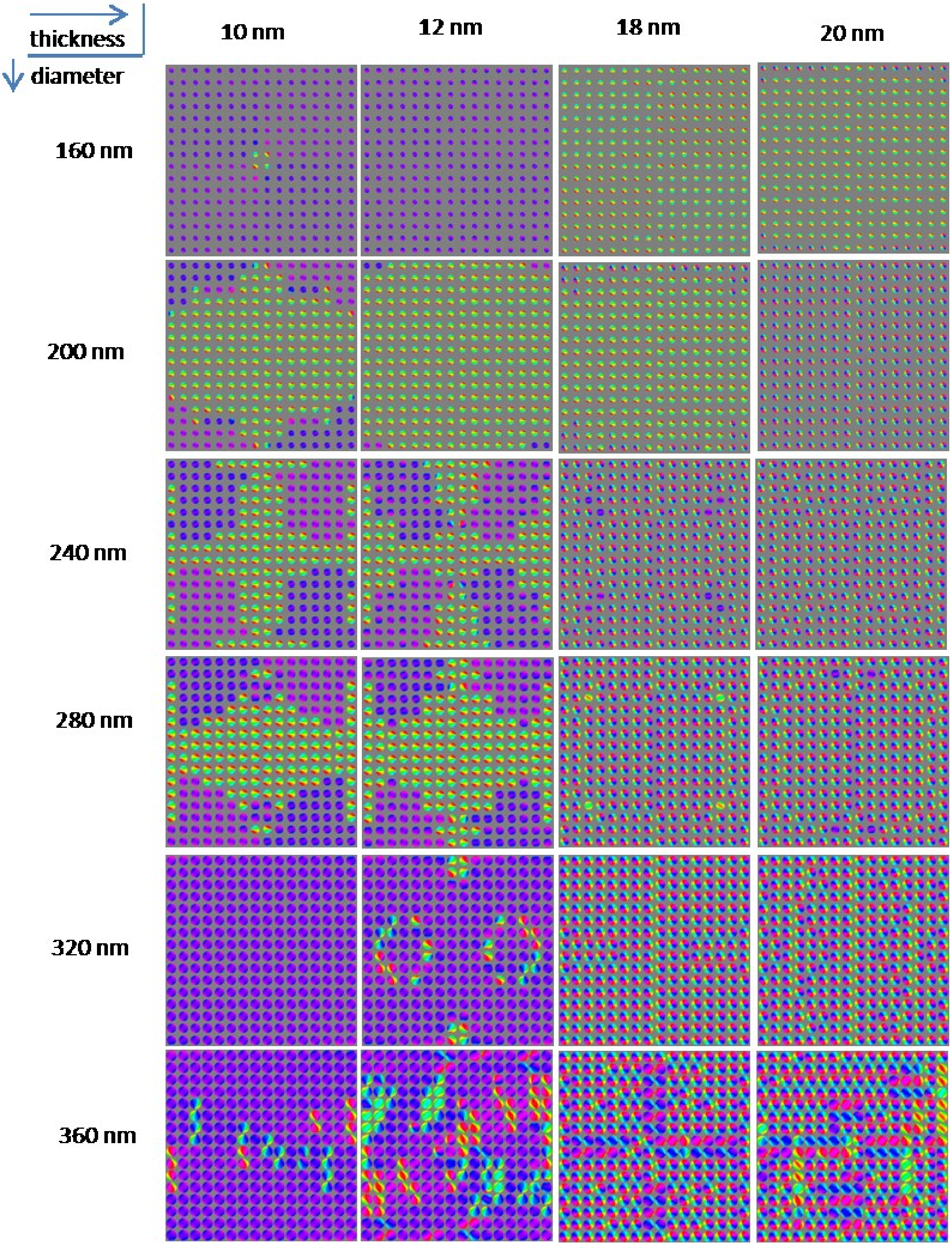

Figure 11: magnetization distribution for squared array of 16x16 dots with different dimensions and with an external field of 10mT

## Conclusions

In this section, thanks to a powerful simulation method and an experimental characterization of finite-size array of circular nanostructured particles, we introduced the “Global Configurational Anisotropy” namely the inhomogeneity on the magnetization distribution over the whole array in the reversal process: the evolution depended on the particle position, i.e. the border particles switched to vortex state before than the particles in the inner positions of the array. The inner particles are more influenced by the surrounding particles, especially along the y axis and consequently the Single Domain State is energetically favored.

We saw that the interdot separation plays an important role in determining the field range within which the vortexes exist: when the interdot distance is increased (by the reduction of the diameter), the dipolar interaction is reduced and the vortex formation is energetically more stable (even though the reduction of the particle diameter favors the SD state). When the interdot separation is reduced (by the increase of the diameter) the vortex state is energetically self-defeating (despite the increase of the diameter would favor the vortex nucleation).

Finally we observed how the thickness influences the vortex nucleation and expulsion, comparing two arrays with the same in-plane geometry but different thickness and proved that for thicker particles the vortex formation is favored, exactly as in the case of single, non-interacting, circular particles.

All this experimental observations are completely confirmed by systematic simulations with which we proved the influence of particle separation in the determination of vortex stability and therefore on the field range of the vortex existence.

# Conclusions

In this thesis work the main scope was the description of magnetic properties of nanostructured materials and in particular the interpretation of the magnetic anisotropies characterizing them. Two types of nanostructures were studied: thin magnetostrictive film and array of interacting nanodots.

The first type of system we analyzed was FeGa thin film deposited on ZnSe/GaAs(001) with a Ga concentration above 15% (the transition composition between the Fe-like to the FeGa magnetic behavior) with thickness between 70 and 90 nm. The FeGa as deposited shows a relevant Perpendicular Magnetic Anisotropy, that allows the formation of stripe domains. The stripes can be rotated by the application of a field of about 800 Oe and remain rotated even after the field removal and that direction becomes the easy one. This effect is known as Rotatable Anisotropy, an unusual type of magnetic anisotropy, which we tried to better comprehend, creating a link to its dynamical and its static definition. To this purpose we used an approximate formula that expresses a connection between MFM and BLS data, calculating the value of the Rotatable Anisotropy field Hrot, introduced as a fit parameter for the matching of the theoretical frequencies of the modes and the theoretical angles of the stripes vs field. At this point we described how the magnetization reversal occurs and found that the mechanism evolves through a series of propagation of dislocations (bifurcations). The same mechanism guides the rotation of the stripes, but with the sequence breaking-rotation-recomposition of stripes in correspondence of defect points of the film. Finally we showed that is possible to induce a particular magnetic distribution called “Mixed Bubble Pattern”, applying a strong field perfectly orthogonal to the film surface (and therefore enhancing the Pependicular Anisotropy) that is still present also after the field removal.

Remaining on the thin magnetostrictive film topic we analyzed a different material produced by sputtering and proved that the growth conditions play a crucial role in determining the Perpendicular Anisotropy (PMA). The PMA, the size and topology of domain patterns can be tailored by changing the evaporation parameters of $TbFe_2$, we found the optimum conditions to enanche the OOP component of the magnetization producing a Tb enrichment of the $Tb_xFe_{1-x}$ phases present in the samples. Films with a weak PMA display rotatable anisotropy: stripes direction can be changed by an external field and maintained when the field is switched off.

The second system involved a different type of magnetic nanostructures: arrays of elliptical and circular nanodot, in which the shape anisotropy played a crucial role in the determination of the properties of the single nanodot but we concentrated our attention on the reciprocal interactions of the particle inside an array and evidenced the configurational anisotropies which steer the behavior and equilibrium states of the magnetization.

We presented the study of different combinations of elliptical dots in different configurations and materials combinations. The single dot were constituted by two ellipses placed side by side along the easy magnetic direction and made by different magnetic material; we analyzed the different cases in which two dots were far (along the easy direction) enough so that they didn’t interact and the case in which they were placed at a distance of 140 nm and magnetically interacting. We also studied what happens when the harder materials is changed and substituted with a softer magnetic material. The change of reciprocal distance of the dot inside an array changes the width of the hysteresis loop, in particular the interaction between the dots along the easy direction enlarges the loop due to the increasing of the switching field in the reversal mechanism. The substitution of the hard material with the soft one transforms the intermediate magnetic material in the harder material and the loop preserves the shape.

Finally we performed a comparison of loops calculated with the simulator OOMMF and experimental measurements finding the same behavior.

In the last chapter, we introduced the “Global Configurational Anisotropy”, that is the inhomogeneity on the magnetization distribution over an array of nanoparticles during the reversal process: the evolution depended on the particle position, i.e. the border particles switched to vortex state before than the particles in the inner positions of the array. We saw that the interdot separation plays an important role in determining the field range within which the vortexes exist, i.e.: the increase/reduction of distance (by the reduction/increase of the diameter) favors/disadvantages the vortex formation. We also observed that for thicker particles the vortex formation is favored, exactly as in the case of single, non-interacting, circular particles.

Experimental observations are confirmed by simulations with which we proved the influence of particle separation in the determination of vortex stability and therefore on the field range of the vortex existence. The Global Configurational Anisotropy is an effect that is always present in dot array with spacing comparable with the dot dimensions and one should take it into account in the development of magnetic ICT applications relying on the control and/or manipulation of the magnetization state of individual dots within a dot array.

The Magnetic Anisotropies discussed in this work are all originated by the reduction of one or more dimensions under the microscopic scale and each dimension confinement brings to new types of anisotropies and magnetic behaviors. The work we performed was aimed to a deepening of the comprehension of those new phenomena, so that it will help the realization of magnetic nanostructures with specific characteristics, for an improvement of the scientific state of the art and increase of performance of new technological devices.

# Bibliography

1. **Mecit Yaman, Tural Khudiyev et al.** Arrays of indefinitely long uniform nanowires and nanotubes. *Nature Materials.* 2011, Vol. 10, 494.

2. **L. Piraux, J. M. George et al.** Giant magnetoresistance in magnetic multilayered nanowires. *Appl. Phys. Lett.* 1994, Vol. 65, 2484.

3. **Cowburn, R P.** Property variation with shape in magnetic nanoelements. *J. Phys. D: Appl. Phys.* 1999, Vol. 33, 1.

4. **Bonanni, Valentina.** *Magnetostatic interactions in arrays of nanostructures - PhD Thesis.* 2008.

5. **B. D. Cullity, C. D. Graham.** *Introduction to Magnetic Materials, 2nd Edition* . s.l. : Wiley, 2009.

6. **Stoner, E. C.** *Phil. Mag.* 1945, Vol. 36, 803.

7. **Osborn, J. A.** *Phys. Rev.* 1945, Vol. 67, 351.

8. **W.H. Meiklejohn, C. P. Bean.** *Phys. Rev.* 1957, Vol. 105, 904.

9. **R. Carey, E. D. Isaac.** *Magnetic Domains and Techniques for their Observation.* London : English Universities Press, 1966.

10. **Neel, L.** *Ann. Geophys.* 1949, Vol. 5, 99.

11. **Kittel, C.** *Rev. Mod. Phys.* 1949, Vol. 21, 541.

12. **Guimaraes, A. P.** *Principles of Nanomagnetism.* Berlin : Springer-Verlag, 2009. Vol. 25.

13. **T. Shinjo, T. Okuno, R. Hassdorf, K. Shigeto, T. Ono.** *Science.* 2000, Vol. 289, 930.

14. **E. H. Frei, S. Shtrikman, and D. Treves.** *Phys. Rev.* 1957, Vol. 106, 446.

15. **M. Natali, I. L. Prejbeanu et al.** Correlated Magnetic Vortex Chains in Mesoscopic Cobalt Dot Arrays. *Phys. Rev. Lett.* 2002, Vol. 88, 15.

16. **Kruglyak V.V, Demokritov S.O, Grundler D.** Magnonics. *J. of Phys. D: Appl. Phys.* 2010, Vol. 43, 264001.

17. *MultiMode SPM Instruction Manual.*

18. **S. Porthun, L. Abelmann, C. Lodder.** Magnetic force microscopy of thin film media for high density magnetic recording. *J. Magn. Magn. Mater.* 1992, Vol. 182, 238-273.

19. **Kerr, J.** *Philos. Mag.* 878, Vol. 5, 161.

20. **Faraday, M.** *Trans. Royal Soc.* 1846, Vol. 5, 592.

21. **A. Hubert, R. Schaefer.** *Magnetic Domains.* Berlin : Springer, 1998.

22. **D. A. Allwood, Gang Xiong, M. D. Cooke, R. P. Cowburn.** *J. Phys. D: Appl. Phys.* 2003, Vol. 36, 2175.

23. **Z. Q. Qiu, S. D. Bader.** *Rev. Sci. Instrum.* 2000, Vol. 71, 1243.

24. **Hulme, H. R.** *Proc. R. Soc. London.* A, 1932, Vol. 135, 273.

25. **Kittel, C.** *Phys. Rev.* 1951, Vol. 83, 208.

26. **Argyres, P. N.** *Phys. Rev.* 1955, Vol. 97, 334.

27. **C Penfold, R. T. Collins, A. P. B. Tufaile, Y. Souche.** *J. Magn. Magn. Mater.* 1996, Vol. 1, 06017.

28. **Freiser, M. J.** *IEEE Trans. Magn.* 1968, Vols. MAG-4, 152.

29. **C.-Y. You, S.-C. Shin.** *J. Appl. Phys.* 1998, Vol. 84, 541.

30. **A. K. Zvezdin, V. A. Kotov.** *Modern Magnetooptics and Magnetooptical Materials.* New York : Taylor and Francis Group, 1997.

31. **Hunt, R. P.** *J. Appl. Phys.* 1967, Vol. 38, 1652.

32. **Y. J. Yang, M. R. Scheinfein.** *J. Appl. Phys.* 1993, Vol. 74, 6810.

33. **J. M. Florczak, E. Dan Dahlberg.** *J. Appl. Phys.* 1990, Vol. 67, 12.

34. **Vavassori, P.** *Appl. Phys. Lett.* 2000, Vol. 77, 1605.

35. **Bonfiglioli, Edgar.** *Film sottili di Fe50Co50 cresciuti mediante dc-magnetron sputtering: meccanismo di crescita e proprietà magnetiche - Thesis.* 2012.

36. **Jones, R. C.** *J. Opt. Soc.* 1941, Vol. 31, 488-493.

37. **R. M. Osgood, S. D. Bader, B. M. Clemens, R. L.White, H. Matsuyama.** *J. Magn. Magn. Mater.* 1998, Vol. 182, 297.

38. **Foner, S.** *Rev. Sci. Instrum.* 1959, Vol. 30, 548-557.

39. **G.Carlotti, G. Gubbiotti, Riv. Nuovo Cimento, 22, 12 (1999).** *Riv. Nuovo Cimento.* 1999, Vol. 22, 12.

40. **Sandercock, J. R.** *Opt. Commun.* 1970, Vol. 2, 73.

41. **M. Eddrief, M. Marangolo, V. H. Etgens, S. Ustaze, F. Sirotti, M. Mulazzi, G. Panaccione, D. H. Mosca, B. Lépine, and P. Schieffer.** Interface bonding of a ferromagnetic/semiconductor junction: A photoemission study of Fe⁄ZnSe(001). *Phys. Rev. B.* 2006, Vol. 73, 115315 .

42. **Adam McClure, S. Albert, T. Jaeger, H. Li, P. Rugheimer, J. A. Schaefer and Y. U. Idzerda.** Properties of single crystal Fe1−xGax thin films. *J. Appl. Phys.* 2009, Vol. 105, 07A938 .

43. **M. Barturen, B. Rache Salles, P. Schio, J. Milano, A. Butera, S. Bustingorry, C. Ramos, A. J. A. de Oliveira, M. Eddrief, E. Lacaze, F. Gendron, V. H. Etgens and M. Marangolo.** Crossover to striped magnetic domains in Fe1−x Ga x magnetostrictive thin films. *Appl. Phys. Lett.* 2012, Vol. 101, 092404 .

44. **M. Eddrief, Y. Zheng, S. Hidki, B. Rache Salles, J. Milano, V. H. Etgens and M. Marangolo.** Metastable tetragonal structure of Fe100−xGax epitaxial thin films on ZnSe/GaAs(001) substrate. *Phys. Rev. B.* 2011, Vol. 84, 161410.

45. **Guozhi Chai, Nguyen N. Phuoc and C. K. Ong.** Exchange coupling driven omnidirectional rotatable anisotropy in ferrite doped CoFe thin film. *Nature.* 2012, Vol. doi:10.1038/srep00832.

46. **Wee Tee Soh, Nguyen N. Phuoc, C. Y. Tan and C. K. Ong.** Magnetization dynamics in permalloy films with stripe domains. *J. Appl. Phys.* 2013, Vol. 114, 053908 .

47. **R. J. Prosen, J. O. Holmen and B. E. Gran.** Rotatable Anisotropy in Thin Permalloy Films. *J. Appl. Phys.* 1961, Vol. 32, S91.

48. **Lehrer, Sherwin S.** Rotatable Anisotropy in Negative Magnetostriction Ni–Fe Films. *J. Appl. Phys.* 1963, Vol. 34, 1207 .

49. **R. D. McMichael, M. D. Stiles, P. J. Chen, and W. F. Egelhoff, Jr.** Ferromagnetic resonance studies of NiO-coupled thin films of Ni80Fe20. *Phys. Rev. B.* 1998, Vol. 58, 8605 .

50. **R. Lopusnik, J. P. Nibarger, T. J. Silva and Z. Celinski.** Different dynamic and static magnetic anisotropy in thin Permalloy™ films. *Appl. Phys. Lett.* 2003, Vol. 83, 96 .

51. **Tomasz Blachowicz, Andrea Tillmanns, Michael Fraune, Reza Ghadimi, Bernd Beschoten, and Gernot Güntherodt.** Exchange bias in epitaxial CoO⁄Co bilayers with different crystallographic symmetries. *Phys. Rev. B* . 2007, Vol. 75, 054425 .

52. **S. Tacchi, S. Fin, G. Carlotti, G. Gubbiotti, M. Madami, M. Barturen, M. Marangolo, M. Eddrief, D. Bisero, A. Rettori, and M. G. Pini.** Rotatable magnetic anisotropy in a Fe0.8Ga0.2 thin film with stripe domains: Dynamics versus statics. *Phys. Rev. B.* 2014, Vol. 89, 024411.

53. **al., Thiele et.** The energy and general traslation force of cylindrical magnetic domains. *The Bell system technical journal.* 1970, Vol. 50, 3.

54. **T. Zhu, Y. Yang, R. C. Yu, H. Ambaye, V. Lauter and J. Q. Xiao.** The study of perpendicular magnetic anisotropy in CoFeB sandwiched by MgO and tantalum layers using polarized neutron reflectometry. *Appl. Phys. Lett.* 2012, Vol. 100, 202406.

55. **S. Mangin, D. Ravelosona1, J. A. Katine, M. J. Carey, B. D. Terris and Eric E. Fullerton.** Current-induced magnetization reversal in nanopillars with perpendicular anisotropy. *Nature Materials.* 2006, Vol. 5, 210 - 215.

56. **R. Sbiaa, H. Meng andS. N. Piramanayagam.** Materials with perpendicular magnetic anisotropy for magnetic random access memory. *Physica Status Solidi (RRL).* 2011, Vol. 5, 12.

57. **F. Casoli, F. Albertini, L. Nasi, S. Fabbrici, R. Cabassi, F. Bolzoni and C. Bocchi.** Strong coercivity reduction in perpendicular FePt⁄Fe bilayers due to hard/soft coupling. *Appl. Phys. Lett.* 2008, Vol. 92, 142506 .

58. **H. Sato, T. Shimatsu, Y. Okazaki, H. Muraoka, H. Aoi, S. Okamoto and O. Kitakami.** Fabrication of L11 type Co-Pt ordered alloy films by sputter deposition. *J. Appl. Phys.* 2008, Vol. 103, 07E114.

59. **Baptiste Carvello, Clarisse Ducruet, Bernard Rodmacq, Stéphane Auffret, Eric Gautier, Gilles Gaudin and Bernard Dieny.** Sizable room-temperature magnetoresistance in cobalt based magnetic tunnel junctions with out-of-plane anisotropy. *Appl. Phys. Lett.* 2008, Vol. 92, 102508 .

60. **Ochiai, Y.** Co/Pt and Co/Pd ultrathin-multilayered films as new magneto-optical recording materials. *Magnetics, IEEE Transactions.* 1989, Vol. 25, 5.

61. **K. Yakushiji, T. Saruya, H. Kubota, A. Fukushima, T. Nagahama, S. Yuasa and K. Ando.** Ultrathin Co/Pt and Co/Pd superlattice films for MgO-based perpendicular magnetic tunnel junctions. *Appl. Phys. Lett.* 2010, Vol. 97, 232508 .

62. **Ikeda, S.** A perpendicular-anisotropy CoFeB–MgO magnetic tunnel junction. *Nature Materials.* 2010, Vol. 9, 721-724.

63. **R. Ranchal, S. Fin, D. Bisero, C. Aroca.** Tailoring the magnetic anisotropy and domain patterns of sputtered TbFeGa alloys. *Journal of Alloys and Compounds.* 2014, Vol. 582, 839–843.

64. **R. Ranchal, V. Gutiérrez-Díez.** Perpendicular magnetic anisotropy in TbFeGa ternary alloys grown by cosputtering. *Thin Solid Films.* 2013, Vol. 534, 557–560.

65. **M. Romera, R. Ranchal, D. Ciudad, M. Maicas and C. Aroca.** Magnetic properties of sputtered Permalloy/molybdenum multilayers. *J. Appl. Phys.* 2011, Vol. 110, 083910 .

66. **González-Martín, R. Ranchal and V.** Investigation on the structural and magnetic properties of sputtered TbFe2/Fe3Ga heterostructures. *J. Appl. Phys.* 2011, Vol. 110, 053901.

67. **V. G. Harris, K. D. Aylesworth, B. N. Das, W. T. Elam, and N. C. Koon.** Structural origins of magnetic anisotropy in sputtered amorphous Tb-Fe films. *Phys. Rev. Lett.* 1992, Vol. 69, 1939 .

68. **Gyorgy, F. Hellman and E. M.** Growth-induced magnetic anisotropy in amorphous Tb-Fe. *Phys. Rev. Lett.* 1992, Vol. 68, 1391 .

69. **Guimarães, Alberto P.** *Principles of Nanomagnetism.* s.l. : Springer, 2009.

70. **Dr. Burkard Hillebrands, Dr. Kamel Ounadjela.** *Spin Dynamics in Confined Magnetic Structures II.* s.l. : Springer, 2003.

71. **Cowburn, R P.** Property variation with shape in magnetic nanoelements. *J. Phys. D: Appl. Phys.* 2000, Vol. 33, R1.

72. **K. S. Buchanan, K. Yu. Guslienko, A. Doran, A. Scholl, S. D. Bader, and V. Novosad.** Magnetic remanent states and magnetization reversal in patterned trilayer nanodots. *Phys. Rev. B.* 2005, Vol. 72, 134415 .

73. **Angles, Spin-Wave Eigenmodes of a Saturated Magnetic Square at Different Precession.** Spin-Wave Eigenmodes of a Saturated Magnetic Square at Different Precession Angles. *Phys. Rev. Lett.* 2007, Vol. 98, 157203 .

74. **al., G. Gubbiotti et.** Finite size effects in patterned magnetic permalloy films. *J. Appl. Phys.* 2000, Vol. 87, 5633 .

75. **al., J.I. Martin et.** Ordered magnetic nanostructures: fabrication and properties. *J. Magn. Magn. Mater.* 2003, Vol. 256, 449–501.

76. **S Jain, A O Adeyeye and N Singh.** Spin re-orientation in magnetostatically coupled Ni80Fe20 ellipsoidal nanomagnets. *Nanotechnology.* 2010, Vol. 21, 285702.

77. **Adeyeye, Junjia Ding andAdekunle O.** Binary Ferromagnetic Nanostructures: Fabrication, Static and Dynamic Properties. *Advanced Functional Materials.* 2013, Vol. 23, 13.

78. **G. Gubbiotti, P. Malagò, S. Fin, S. Tacchi, L. Giovannini, D. Bisero, M. Madami, G. Carlotti, J. Ding, A. O. Adeyeye, and R. Zivieri.** Magnetic normal modes of bicomponent permalloy/cobalt structures in the parallel and antiparallel ground state. *Phys. Rev. B.* 2014, Vol. 90, 024419 .

79. **N. Dao, S. R. Homer and S. L. Whittenburg.** Micromagnetics simulation of nanoshaped iron elements: Comparison with experiment. *J. Appl. Phys.* 1999, Vol. 86, 3262 .

80. **R. Engel-Herbert, T. Hesjedal, J. Mohanty, D. M. Schaadt, and K. H. Ploog.** Magnetization reversal in MnAs films: Magnetic force microscopy, SQUID magnetometry, and micromagnetic simulations. *Phys. Rev. B.* 2006, Vol. 73, 104441.

81. **Xiaobin Zhu, P. Grütter, V. Metlushko and B. Ilic.** Magnetization reversal and configurational anisotropy of dense permalloy dot arrays. *Appl. Phys. Lett.* 2002, Vol. 80, 4789 .

82. **M. Kleiber, F. Kümmerlen, M. Löhndorf, A. Wadas, D. Weiss, and R. Wiesendanger.** Magnetization switching of submicrometer Co dots induced by a magnetic force microscope tip. *Phys. Rev. B.* 1998, Vol. 58, 5563 .

83. **A. Vansteenkiste, B. Van de Wiele.** MuMax: A new high-performance micromagnetic simulation tool. *J. Magn. Magn. Mater.* 2011, Vol. 323, 21, pp. 2585–2591.

84. **Welland, R. P. Cowburn and M. E.** Micromagnetics of the single-domain state of square ferromagnetic nanostructures. *Phys. Rev. B.* 1998, Vol. 58, 9217 .

85. **R. P. Cowburn, D. K. Koltsov, A. O. Adeyeye and M. E. Welland.** Designing nanostructured magnetic materials by symmetry. *Europhys. Lett.* 1999, Vol. 48, 2, p. 221.

86. **P. Vavassori, D. Bisero, F. Carace, A. di Bona, G. C. Gazzadi, M. Liberati, and S. Valeri.** Interplay between magnetocrystalline and configurational anisotropies in Fe(001) square nanostructures. *Phys. Rev. B.* 2005, Vol. 72, 054405.

87. **Ben Van de Wiele, Samuele Fin, Anandakumar Sarella, Paolo Vavassori and Diego Bisero.** How finite sample dimensions affect the reversal process of magnetic dot arrays. *Appl. Phys. Lett.* 2014, Vol. 105, 162407.

88. **André Thiaville, José Miguel García, Rok Dittrich, Jacques Miltat, and Thomas Schrefl.** Micromagnetic study of Bloch-point-mediated vortex core reversal. *Phys. Rev. B.* 2003, Vol. 67, 094410.

89. **J. Sort, A. Hoffmann, S.-H. Chung, K. S. Buchanan, M. Grimsditch, M. D. Baró, B. Dieny, and J. Nogués.** Magnetization Reversal in Submicron Disks: Exchange Biased Vortices. *Phys. Rev. Lett.* 2005, Vol. 95, 067201 .

90. **Myoung-Woo Yoo, Jehyun Lee and Sang-Koog Kim.** Radial-spin-wave-mode-assisted vortex-core magnetization reversals. *Appl. Phys. Lett.* 2012, Vol. 100, 172413.

91. **Matthias Kammerer, Hermann Stoll, Matthias Noske, Markus Sproll, Markus Weigand, Christian Illg, Georg Woltersdorf, Manfred Fähnle, Christian Back, and Gisela Schütz.** Fast spin-wave-mediated magnetic vortex core reversal. *Phys. Rev. B.* 2012, Vol. 86, 134426.

92. **Giovannini, F. Montoncello and L.** Bandwidth broadening and asymmetric softening of collective spin waves in magnonic crystals. *Appl. Phys. Lett.* 2014, Vol. 104, 242407.

93. **Roman Verba, Gennadiy Melkov, Vasil Tiberkevich and Andrei Slavin.** Fast switching of a ground state of a reconfigurable array of magnetic nano-dots. *Appl. Phys. Lett.* 2012, Vol. 100, 192412.

94. **Jain, A. O. Adeyeye and S.** Coupled periodic magnetic nanostructures. *J. Appl. Phys.* 2011, Vol. 109, 07B903 .

95. **M Sepioni, M Madami, S Tacchi, G Gubbiotti, G Carlotti, D Bisero, A O Adeyeye, N Singh and S Goolaup.** Dipolar interaction in dense chains of submicrometric rectangular dots. *J. Phys.: Conf. Ser.* 2010, Vol. 200, 072089.

96. **E. Nikulina, O. Idigoras, P. Vavassori, A. Chuvilin, and A. Berger.** *Appl. Phys. Lett.* 2012, Vol. 100, 142401 .

97. **I. L. Prejbeanu, M. Natali, L. D. Buda, U. Ebels, A. Lebib, Y. Chen, and K. Ounadjela.** In-plane reversal mechanisms in circular Co dots. *J. Appl. Phys.* 202, Vol. 91, 10.